

1987

## Sites and diffusion of muons in FCC metal hydride systems

James Russell Kempton  
*College of William & Mary - Arts & Sciences*

Follow this and additional works at: <https://scholarworks.wm.edu/etd>



Part of the [Condensed Matter Physics Commons](#)

---

### Recommended Citation

Kempton, James Russell, "Sites and diffusion of muons in FCC metal hydride systems" (1987).  
*Dissertations, Theses, and Masters Projects*. Paper 1539623772.  
<https://dx.doi.org/doi:10.21220/s2-wqm0-cn08>

This Dissertation is brought to you for free and open access by the Theses, Dissertations, & Master Projects at W&M ScholarWorks. It has been accepted for inclusion in Dissertations, Theses, and Masters Projects by an authorized administrator of W&M ScholarWorks. For more information, please contact [scholarworks@wm.edu](mailto:scholarworks@wm.edu).

## **INFORMATION TO USERS**

**The most advanced technology has been used to photograph and reproduce this manuscript from the microfilm master. UMI films the original text directly from the copy submitted. Thus, some dissertation copies are in typewriter face, while others may be from a computer printer.**

**In the unlikely event that the author did not send UMI a complete manuscript and there are missing pages, these will be noted. Also, if unauthorized copyrighted material had to be removed, a note will indicate the deletion.**

**Oversize materials (e.g., maps, drawings, charts) are reproduced by sectioning the original, beginning at the upper left-hand corner and continuing from left to right in equal sections with small overlaps. Each oversize page is available as one exposure on a standard 35 mm slide or as a 17" × 23" black and white photographic print for an additional charge.**

**Photographs included in the original manuscript have been reproduced xerographically in this copy. 35 mm slides or 6" × 9" black and white photographic prints are available for any photographs or illustrations appearing in this copy for an additional charge. Contact UMI directly to order.**



300 North Zeeb Road Ann Arbor, MI 48106-1346 USA



Order Number 8802437

**Sites and diffusion of muons in FCC metal hydride systems**

Kempton, James Russell, Ph.D.

The College of William and Mary, 1987

**U·M·I**  
300 N. Zeeb Rd.  
Ann Arbor, MI 48106



SITES AND DIFFUSION OF MUONS  
IN FCC METAL HYDRIDE SYSTEMS

---

A Dissertation

Presented to

The Faculty of the Department of Physics  
The College of William and Mary in Virginia

In Partial Fulfillment

Of the Requirements for the Degree of  
Doctor of Philosophy

---

by

James Russell Kempton

1987


APPROVAL SHEET

This dissertation is submitted in partial fulfillment of  
the requirements for the degree of


Doctor of Philosophy


  
James Russell Kempton


Approved, August 1987

  
William J. Kossler

  
Kenneth G. Petzinger

  
Harlan E. Schone

  
Gina L. Hoatson

  
Gary C. Defotis  
Department of Chemistry  
The College of William and Mary in Virginia

To my wife, Julie, for her encouragement



## TABLE OF CONTENTS

	Page
ACKNOWLEDGEMENTS . . . . .	vi
LIST OF TABLES . . . . .	viii
LIST OF FIGURES . . . . .	ix
ABSTRACT . . . . .	xii
CHAPTER I. INTRODUCTION . . . . .	2
CHAPTER II. EXPERIMENTAL DETAILS . . . . .	5
2.1 MUON PRODUCTION . . . . .	5
2.2 DATA COLLECTION . . . . .	9
2.3 TEMPERATURE AND MAGNETIC FIELD CONTROL . . . . .	14
2.4 PREPARATION OF SAMPLES . . . . .	18
CHAPTER III. INTERACTIONS OF THE MUON WITH THE LATTICE	22
3.1 THERMALIZATION . . . . .	22
3.2 MAGNETIC INTERACTION . . . . .	26
3.3 ELECTRONIC INTERACTION . . . . .	34
3.4 SUMMARY . . . . .	46
CHAPTER IV. MUON DIFFUSION . . . . .	47
4.1 THERMALLY-ACTIVATED TUNNELING . . . . .	49
4.2 THERMALLY-ACTIVATED JUMPING . . . . .	55
CHAPTER V. $\mu$ SR TECHNIQUES . . . . .	59
5.1 TRANSVERSE-FIELD TECHNIQUE . . . . .	59

5.2	ZERO-FIELD TECHNIQUE . . . . .	69
5.3	LONGITUDINAL-FIELD TECHNIQUE . . . . .	76
5.4	SUMMARY . . . . .	78
CHAPTER VI. MONTE CARLO SIMULATIONS . . . . .		82
6.1	THE MODEL . . . . .	84
6.2	APPLICATION OF THE MONTE CARLO METHOD . . . . .	88
6.3	RESULTS . . . . .	90
CHAPTER VII. RESULTS AND DISCUSSION . . . . .		93
7.1	TRANSVERSE-FIELD STUDIES . . . . .	105
7.2	ZERO-FIELD STUDIES . . . . .	145
7.3	LONGITUDINAL-FIELD STUDIES . . . . .	157
CHAPTER VIII. CONCLUSION . . . . .		160
APPENDIX A.	COMPUTER PROGRAM FOR SIMULATION OF MOTION ON A CUBIC LATTICE . . . . .	164
APPENDIX B.	DIPOLAR BROADENING BY UNLIKE SPINS . . . . .	176
APPENDIX C.	DERIVATION OF THE PARAMETERS $\alpha$ AND $r_B$ . . . . .	179
APPENDIX D.	CALCULATION OF A ZERO-FIELD RELAXATION FUNCTION . . . . .	182
APPENDIX E.	ZERO-FIELD SPIN-SPIN RELAXATION TIME . . . . .	184
REFERENCES	. . . . .	186
VITA	. . . . .	190

## ACKNOWLEDGEMENTS

The writing of a dissertation is the culmination of several years of work toward the Doctor of Philosophy. These years have been filled with times of celebration as the secrets of physics were unlocked and also with times of frustration when these same secrets were not within reach. I am grateful not only for these times, but for those people who have taken part. These include the faculty, staff, and graduate students of the department of physics and the computer center at The College of William and Mary and the members of St. Stephen Lutheran Church. I am especially indebted to the following people for their involvement:

Professor William J. Kossler, my advisor, for his commitment and help in these experiments and their analysis and for his guidance and friendship;

Professor Harlan E. Schone, for his support and for stimulating my interest in metal hydride materials;

Professor Kenneth G. Petzinger, for many hours of helpful discussion and for his interest in this work;

Professors Gina L. Hoatson and Gary C. Defotis for their careful reading of this manuscript;

Dr. James J. Reilly, for preparation of the titanium and lanthanum hydride samples;

Professors E. F. W. Seymour, Carey E. Stronach and William F. Lankford, Drs. Bassam S. Hitti and Yong Li, and Xiao-hong Yu, for their help in these experiments and analysis;

The National Science Foundation (Grant# DMR8503223), for supporting this work;

and my wife, Julie, for her love, understanding, and encouragement during the past five years.

## LIST OF TABLES

Table	Page
2.1 Characteristics of the muon beam at BNL . . . . .	8
3.1 Energy levels for polaronic motion of proton isotopes in copper . . . . .	44
6.1 Results of the Monte Carlo Simulations . . . . .	92
7.1 Lattice constants for titanium hydride . . . . .	94
7.2 Prefactor and activation energy for fits to Eqn. 7.10 for $TiH_x$ data . . . . .	117
7.3 $p_r$ products for $TiH_{1.97}$ data . . . . .	122
7.4 Tunneling matrix elements and activation energies for fits to Eqn. 7.14 for $TiH_x$ data . . . . .	125
7.5 Probability for the existence of a vacancy at a second-nearest-neighbor site, tunneling matrix element, and activation energy for the two $\mu$ SR titanium hydride samples at 500 K. . . . .	127
7.6 Percentage of occupied octahedral sites in yttrium hydride as a function of hydrogen concentration and temperature as measured by neutron scattering and NMR. . . . .	132
7.7 Percentage of tetrahedral sites occupied by muons in yttrium hydride as a function of temperature and hydrogen concentration. . . . .	134
7.8 Prefactor and activation energies for proton correlation times obtained from $T_{1\rho}$ measurements. . . . .	138
7.9 The zero-field depolarization rate as a function of hydrogen concentration in titanium hydride at 100 K. . . . .	152
7.10 The zero-field depolarization rate in yttrium hydride at 20 K and 295 K . . . . .	157

## LIST OF FIGURES

Figure	Page
2.1a The angular distribution of the emitted positron with respect to the muon spin for $a=1/3$ . . . . .	10
2.1b The angular distribution of the emitted positron with respect to the muon spin for $a=0.18$ . . . . .	11
2.2 The BNL $\mu$ SR apparatus. . . . .	12
2.3 The constant current source used to measure the resistance of the temperature sensor $R_t$ . . . . .	15
2.4 The control circuit for a field shimming coil. . . . .	17
3.1 Excess projected range for the muon as a function of displacement energy for various materials. . . . .	25
3.2 The precession of the muon magnetic moment, $\vec{\mu}$ , in an external field $H_0$ . . . . .	26
3.3 Macroscopic magnetic field inside a magnetized ellipsoidal sample. . . . .	32
3.4 Distribution of energy levels due to the dipolar interaction. . . . .	35
3.5 Interstitial sites in FCC lattices. . . . .	38
3.6 Contour plot of the charge density of a typical FCC lattice. . . . .	39
3.7 Charge- and spin-density distribution around a positive muon in a spin-polarized electron gas. . . . .	42
3.8 Interaction potential between positive point charges and $Cu^+$ ions in Cu metal. . . . .	43
4.1 Diffusion mechanisms for light interstitials as a function of temperature. . . . .	48
4.2 Thermally-activated tunneling of a light interstitial. . . . .	50
5.1 A typical $\mu$ SR transverse-field histogram. . . . .	62

5.2	Calculated line widths for T sites in a FCC crystal as a function of the relative interaction strength $\omega_B/\omega_E$ .	65
5.3	Muon field-correlation time as a function of temperature and hydrogen concentration in NbH <sub>x</sub> .	70
5.4	Calculated muon spin relaxation functions for different values of the field-correlation time, $\tau$ .	75
5.5	Muon polarization in zero field as a function of time.	77
5.6	Field dependence of the $\mu^+$ longitudinal-field relaxation functions in MnSi.	79
5.7	Comparison of longitudinal- and zero-field muon relaxation functions.	80
6.1	The pulse sequence for the stimulated-echo method of measuring diffusion coefficients.	85
6.2	Measured and predicted values of the diffusion coefficient for TiH <sub>1.55</sub> .	86
7.1	Lattice structure for FCC metal hydrides.	95
7.2a-b	Lattice constant for titanium hydride.	96
7.2c	Phase diagram for titanium hydride.	97
7.3	Phase diagram for yttrium hydride.	98
7.4a-b	Lattice constant for zirconium hydride.	99
7.4c	Phase diagram for zirconium hydride.	100
7.5a	Phase diagram for lanthanum hydride.	101
7.5b-c	Lattice parameter for lanthanum hydride.	102
7.6	Muon depolarization rate, $\Lambda$ , as a function of temperature for TiH <sub>x</sub> .	106
7.7	The depolarization parameter, $\Lambda_{\text{Exp}}^2$ , in region I for titanium hydride plotted as a function of vacancy concentration.	110
7.8	The mean time of stay for a muon at an octahedral site, $\tau_B$ , plotted as a function of temperature.	114

7.9	Muon field-correlation time plotted as a function of temperature for $TiH_{1.83}$ and $TiH_{1.97}$ .	118
7.10	The depolarization rate, $\lambda$ , in yttrium hydride as function of temperature for $YH_{1.77}$ and $YH_2$ .	131
7.11	Muon field-correlation time plotted as a function of temperature for $YH_{1.77}$ .	137
7.12	The zero-field depolarization rate as a function of temperature for $ZrH_{1.99}$ , $ZrH_{1.90}$ , and $ZrH_{1.56}$ .	140
7.13	The depolarization rate as a function of temperature for $ZrH_{1.94}$ .	141
7.14	The depolarization rate as a function of temperature for $LaH_{2.06}$ .	144
7.15a	Experimentally-determined zero-field muon polarization as a function of time for $TiH_{1.99}$ at 100 K.	147
7.15b	Experimentally-determined zero-field muon polarization as a function of time for $TiH_{1.97}$ at 100 K.	148
7.15c	Experimentally-determined zero-field muon polarization as a function of time for $TiH_{1.83}$ at 100 K.	149
7.15d	Experimentally-determined zero-field muon polarization as a function of time for $TiH_{1.83}$ at 100 K.	150
7.16a	Experimentally-determined zero-field muon polarization as a function of time for $YH_2$ at 20 K.	155
7.16b	Experimentally-determined zero-field muon polarization as a function of time for $YH_2$ at 295 K.	156
7.17	Experimentally-determined longitudinal-field muon polarization as a function of time for $TiH_{1.97}$ at 100 K and 7.9 G.	159



## ABSTRACT

A positive muon can be considered an isotope of hydrogen due to similarities in spin and charge. For metal hydride systems, the muon enters the sample "as the last hydrogen added," and competes for the same sites as the hydrogen atoms. To observe the site competition and diffusion of both particles (muon and proton), several FCC metal hydrides,  $TiH_{1.83}$ ,  $TiH_{1.97}$ ,  $TiH_{1.99}$ ,  $YH_{1.77}$ ,  $YH_2$ ,  $ZrH_{1.94}$ , and  $LaH_{2.06}$ , were studied using transverse-, zero-, and low longitudinal-field  $\mu$ SR. The low temperature region results indicate that the muon predominately occupies octahedral sites for the FCC metal hydrides in this study. The probability for a muon to occupy a tetrahedral site in titanium and zirconium hydrides at these temperatures is proportional to the vacancy concentration. Whereas the probability for T site occupation in yttrium hydride is proportional to the number of protons not occupying these sites which increases with hydrogen concentration. Muon T site occupancy below room temperature for  $LaH_{2.06}$  was not observed and was not expected since these sites are occupied by protons. Around 300 K, the muon diffuses over interstitial O sites to vacancies in the H sublattice of  $TiH_{1.99}$ . The vibration of the hydrogen lattice is found to be the mechanism responsible for the activation of the muon out of the O site. Above room temperature, the muon occupies tetrahedral sites in yttrium and titanium hydrides. At high temperatures, the field-correlation time for a muon in titanium and yttrium hydrides is approximately one to two orders of magnitude greater than for a proton as measured by NMR. The results of a Monte Carlo simulation indicate that the presence of the muon inhibits the motion of the nearest-neighbor protons at high temperatures. The dynamics of the proton spins are observed by zero- and low longitudinal-field  $\mu$ SR through the oscillation of the muon polarization at long times for a static muon in a T or O site. This observation is not predicted by the Kubo-Toyabe treatment for a stationary muon.

SITES AND DIFFUSION OF MUONS  
IN FCC METAL HYDRIDE SYSTEMS

The Muon Spin Rotation ( $\mu$ SR) technique has existed for the past thirty years.<sup>1</sup> At the time of its invention, it was recognized as an excellent tool for solid state physics. The advantages of using the muon as a probe are three-fold: its mass, which is one-ninth that of the proton, its point charge, and its large magnetic moment.<sup>2</sup> These features make it sensitive to quantum tunneling at low temperatures, internal magnetic fields, lattice defects and impurities. The time scale of sensitivity of this probe ranges from tens of microseconds to nanoseconds or smaller under optimal conditions. The short time scale is imposed by the electronics of the data collection system; while the large time scale limit is due to the finite muon lifetime of 2.2 microseconds.<sup>3</sup> However, the technique failed to grow in usage over the next fifteen years due to a lack of high intensity meson factories. This handicap allowed techniques such as NMR and ESR to become the preferred probe for exploring materials. In the early 70s with the building of high intensity meson facilities such as SIN and TRIUMF, the use of this probe began to grow. People started to study ferromagnets, superconductors, semiconductors, and metals.<sup>3</sup> Recently this technique has been used by the  $\mu$ SR group at the College of

William and Mary to determine the magnetic ordering in the superconducting state of the heavy fermion compound  $\text{CeCu}_{2.1}\text{Si}_2$  and the London penetration depth in high  $T_c$  superconductors ( $\text{La}_{1.85}\text{Sr}_{0.15}\text{CuO}_4$  and  $\text{YBa}_2\text{Cu}_3\text{O}_7$ ).

This work is a study of FCC metal hydride systems using muons as a probe. These systems have been studied extensively with NMR and neutrons. These methods tend to measure quantities averaged over all nuclear sites, e.g. spin-lattice relaxation times and scattering cross sections.  $\mu\text{SR}$  is sensitive to the magnetic fields at interstitial and substitutional sites. The muon's ability to occupy interstitial sites provides information not available to the techniques listed above. This study exploits the similarities between a muon and a proton, such as charge, spin and mass. For this reason, this work will focus on FCC metal hydride systems, where the metal has a very small magnetic moment, to study the interactions between protons and muons. These studies will serve as a guide for analysis of the results from experiments on a FCC hydride system which contains a metal having a magnetic moment. The hydride compounds which we have chosen are  $\text{YH}_x$  ( $x=1.77$  and  $2.00$ ),  $\text{TiH}_y$  ( $y=1.83$ ,  $1.97$ , and  $1.99$ ),  $\text{ZrH}_{1.94}$  and  $\text{LaH}_{2.06}$ .

In this set of experiments we started with samples hydrided close to stoichiometry. Due to the similarity between a proton and a muon, we expect the muon to behave as if it were the last hydrogen being added to the system.

At low temperatures ( $T < 100$  K) in high H concentration samples, the muon decays before it has a chance to find a vacant site in the hydrogen lattice. If the hydrogen concentration is lowered (or in other words the number of vacancies in the H sublattice is increased) the probability for the muon to occupy one of these sites is increased. As the temperature is raised, the muon is able to find vacant sites in the hydrogen lattice. At very high temperatures, one sees activation out of these sites with diffusion limited by the vacancy concentration.

In chapter 2, the experimental details of this study, such as the production of the muons, sample preparation, temperature control, and data collection, will be discussed. The focus of chapter 3 is to provide insight into some of the interactions between the muon and the hydrogen alloy. Chapter 4 is devoted to the diffusion processes of muons and protons in these metal hydrides. In Chapter 5, the measurement of the interactions between the muon and hydrogen alloy with the  $\mu$ SR techniques in this study is discussed. Chapter 6 centers on an effort to model the effect of hydrogen motion on the depolarization of the muon's spin. In chapter 7, the results of the  $\mu$ SR studies of metal hydride systems are presented and discussed.

CHAPTER 2  
EXPERIMENTAL DETAILS

2.1 MUON PRODUCTION<sup>4</sup>

Polarized positive muons are produced by the decay of mesons, such as pions and kaons.<sup>5</sup> Since the yield of pions per incident proton is much greater than for kaons, the pion is the meson of choice. Pions can be produced by several reactions. One of these is a proton of energy greater than 180 MeV striking a production target (e.g. C, Be) and producing a pion by the following reactions:



Conservation of angular momentum for these two reactions requires that the pion be a spin zero particle. If one increases the proton energy, then multiple production of pions may occur due to an increase in the number of proton interactions with the target.

The pion has a lifetime of 26 nanoseconds and decays into a muon and neutrino.

$$\pi^+ \longrightarrow \mu^+ + \nu_\mu \quad (2.3)$$

This weak decay violates parity and produces the polarized muon. In the center of mass frame of the positive pion, the muon and the muonic neutrino are emitted in opposite directions to conserve momentum. Since the neutrino has a negative helicity (left handed), the spin vector of the muon must be antiparallel to its momentum.

For pions of finite momentum ( $\sim 180$  MeV/c), a beam transport system consisting of at least a row of quadrupole magnets, known as a muon channel, must be used. The purpose of the muon channel is to provide an area where the pions can decay. Other elements such as dipole magnets can be added to the beam transport system to select the momentum of the pions and muons. This type of beam is known as a decay beam. During the decay process, the transport system accepts muons which decay in a forward or backward direction (known as "forward" or "backward" muons) in the pion center of mass frame. The effective polarization of this muon beam is less than 100%. The loss of polarization is due to the acceptance by the beam transport system of muons whose momentum (in the pion center-of-mass frame) is not along the axis of the muon channel.

A second method of muon production is the surface beam. This beam is characterized by pion decay near the surface of the production target. This means that the lab frame and pion center of mass frame are the same and that

the effective polarization of the muon beam is 100% antiparallel to the beam momentum. The advantage of this type of beam is that the muon can stop in a couple of milligrams of material as opposed to several grams for the decay beam. Due to the low amount of mass necessary to stop a surface beam, the entire beam line from the production target to the sample must be under vacuum which complicates the transport, detector and cryostat systems.

The polarized muons at the Alternating Gradient Synchrotron (AGS) at Brookhaven National Laboratory (BNL) used in these experiments were produced by a decay beam. The pions were created by bombarding a platinum target with 28.3 GeV/c protons. Every 3.2 seconds an approximately square intensity envelope containing  $1 \times 10^{12}$  protons and of duration 1.0 seconds arrived at the production target. This produced 4000 muons at the sample. The characteristics of the beam for the hydride experiments are listed in Table 2.1.

In order to observe internal fields in the sample, one needs to know the orientation of the muon's spin as a function of time. One can infer this by knowing the direction of the spin when the muon decays. The muon decays by the following parity violating weak decay

$$\mu^+ \text{ ----> } e^+ + \nu_e + \bar{\nu}_\mu \quad (2.4)$$

with a lifetime of  $2.19703(4) \times 10^{-6}$ .<sup>5</sup> Since one cannot detect neutrinos efficiently, the direction of the emitted



Table 2.1

Characteristics of the muon beam used for the hydride experiments at BNL.

---

Target	7.5 x 1 x 1 cm <sup>3</sup> Pt
P <sub>π</sub>	180 MeV/c
P <sub>μ</sub>	90 MeV/c
E <sub>μ</sub>	33 MeV
Range (μ <sup>+</sup> )	5.5 grams/cm <sup>2</sup>
Maximum Stopping Rate	2 x 10 <sup>3</sup> μ <sup>+</sup> /(cm <sup>2</sup> -TP*)
Polarization	80 %
Macro-time Structure	
Spill Length	1.0 μs
Acceleration Length	2.2 μs
Period	3.2 μs
Background	0.5 %
e <sup>+</sup> (detected/muon)	0.5

---

\* TP Tera (10<sup>12</sup>) Protons on Target

positron must be measured in order to obtain the orientation of the muon spin at the time of decay. The angular distribution of the emitted positron is given by<sup>3</sup>

$$W(\theta) = 1 + a \cos(\theta) \quad (2.5)$$

where  $\theta$  is the angle between the muon spin and the positron's direction and  $a$  is an asymmetry factor which equals  $1/3$  if all energies of the emitted positrons are detected with equal probability (Fig. 2.1a). The value of one-third for  $a$  assumes that the polarization of the muon is 100% and that the solid angle subtended by each positron detector is not large. The value of  $a$  for the beam and detectors used at BNL is 0.18 (Fig. 2.1b). One notices that the probability for emission along the direction of the muon spin is greater for  $a=1/3$ .

## 2.2 DATA COLLECTION

The detector system along with shielding, collimation, Helmholtz pair, and cryostat for the  $\mu$ SR experiments is shown in Fig. 2.2. The detectors consist of an organic scintillator optically coupled to a photomultiplier tube via a Plexiglas light guide (or optical fibers as used at KEK in Japan). The passage of a charged particle (i.e. muon or positron) through the scintillator excites the electrons in the organic molecules.<sup>6</sup> A photon is emitted to allow the electron to return to a lower energy state. This photon is then transformed into an electrical pulse by the photomultiplier tube.

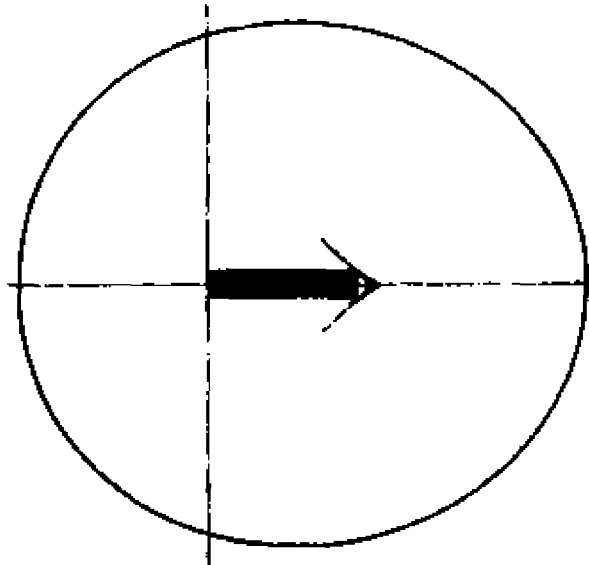


Figure 2.1a  
The angular distribution of the emitted positron with respect to the muon spin.  $W(\theta) = 1 + a \cdot \cos\theta$  with  $a=1/3$ .

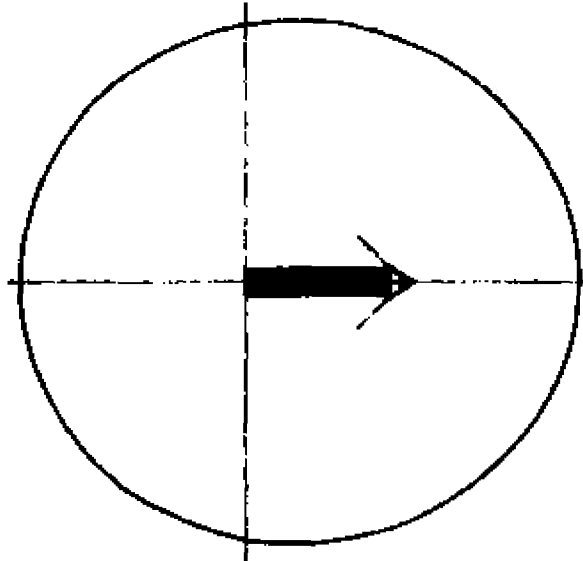


Figure 2.1b  
The angular distribution of the emitted positron with  
respect to the muon spin.  $W(\theta) = 1 + a \cdot \cos\theta$  with  $a=0.18$ .

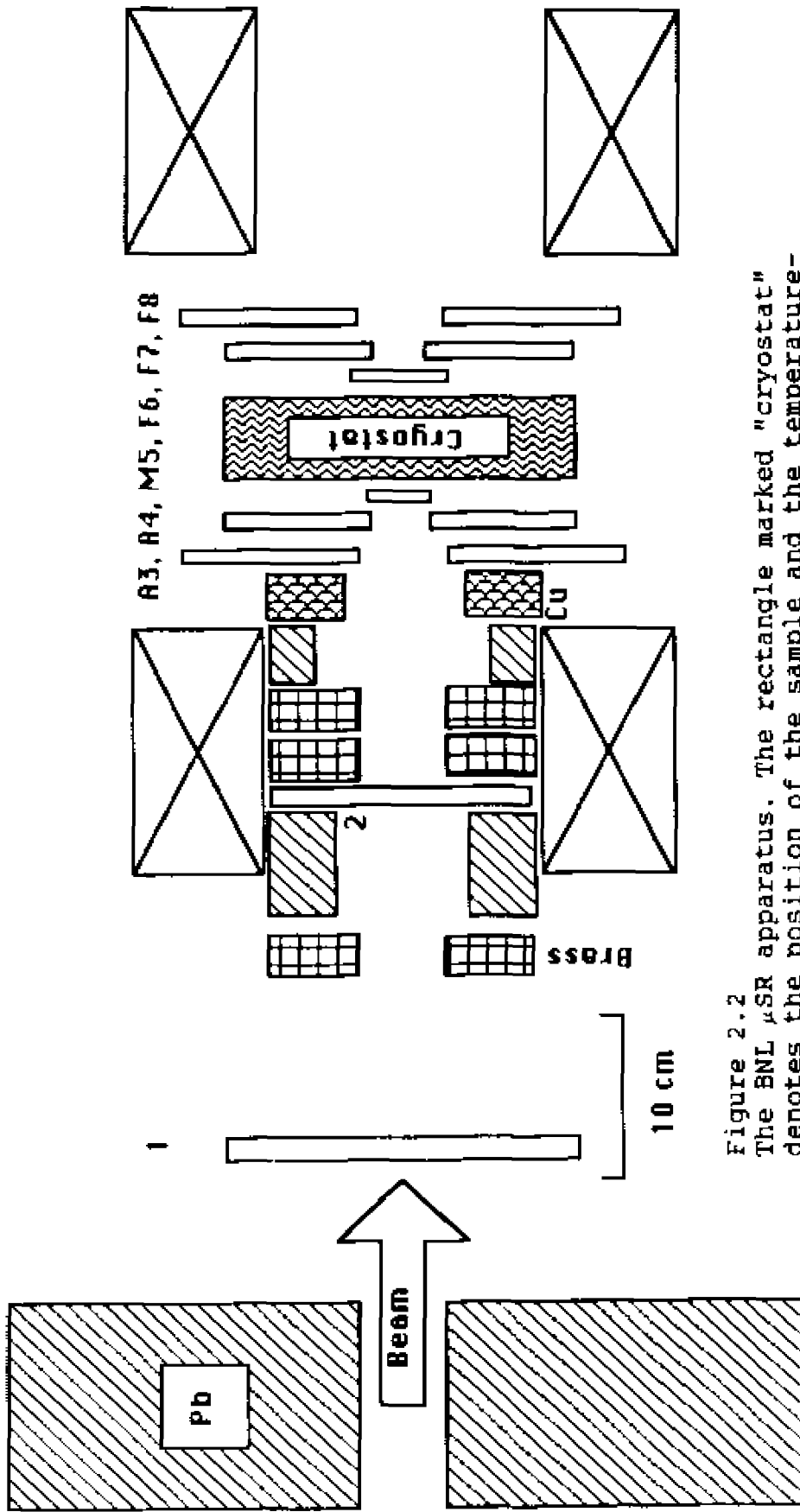


Figure 2.2  
 The BNL  $\mu$ SR apparatus. The rectangle marked "cryostat" denotes the position of the sample and the temperature-control system. The four rectangles represent the air core coils in arrangement near the Helmholtz condition with their axis in the plane of the page and perpendicular to the beam momentum. The collimators of lead, brass, and copper and the detectors (as numbered rectangles) are also included.

Incoming muons after passing through a variable thickness water degrader, placed inside the last quadrupole magnet, and through collimators made of lead, brass, and copper (Fig. 2.2) are detected by a coincidence between detectors 1, 2 and M5 (12M5). Detection of muons which stop in the sample is achieved by a coincidence between  $12M5\overline{F6}$ , where the bar denotes an anticoincidence. This signal is used to start a clock. The backward-direction positron detectors A3 and A4 have small holes in the center of them to allow the incident muon beam to pass through without generating a signal in these detectors. The forward-direction positron detectors F7 and F8 also have holes for reasons of symmetry. An emitted positron is detected by a coincidence of  $\overline{2A3A4F7F8}$  or  $\overline{2A3A4F7F8}$  for a "forward" or "backward" positron. This signal stops the clock started by the incident muon. This time is converted into a voltage (or amplitude) by a TAC (time to amplitude converter) and is then input to a multichannel analyzer. If a second muon should be detected before a time (10-20  $\mu$ s) after the detection of the first muon, then the clock is reset to zero with no output of the TAC being generated. Another instance where the clock must be reset is when no positron is detected. This is mainly due to the lack of positron detectors for  $e^+$  decaying in the vertical directions ( $\pm\pi/2$ ) and is seen in the ratio  $e^+$  detected per muon in Table 2.1. Therefore it is necessary to reset the clock after 10 to 20 microseconds. The signals going to

the multichannel analyzer must be directed to the proper section for storage which is accomplished by a router box. The two spectra (backward and forward) in the multichannel analyzer are transferred to a computer, which is used for analysis and storage.

### 2.3 TEMPERATURE AND MAGNETIC FIELD CONTROL

Several temperature control systems were used for these studies. For  $\text{TiH}_{1.99}$  with  $T < 300$  K, this hydride compound was mounted in a  $^4\text{He}$  flow cryostat equipped with platinum and carbon-glass resistors and a gold-chromel thermocouple. For temperatures above 300 K, a heated-water circulating system with a platinum sensor was used. The temperature in both systems was determined by measuring the current through the resistor. The current was provided by a nine-volt battery. The studies of  $\text{TiH}_{1.83}$ ,  $\text{TiH}_{1.97}$ ,  $\text{YH}_2$ , and  $\text{ZrH}_{1.94}$  for  $T < 300$  K were performed using an Air Products helium Displex closed-cycle refrigerator equipped with a platinum resistor and a gold-chromel thermocouple. The same refrigerator was used for the low temperature measurements on  $\text{LaH}_{2.06}$  and  $\text{YH}_{1.77}$ , but was also equipped with a carbon-glass sensor. A constant-current source (Fig. 2.3) was connected to two of the four sensor leads. The resistance of these sensors was determined by measuring the potential difference between the other two leads. For the investigations of  $\text{TiH}_{1.83}$ ,  $\text{TiH}_{1.97}$ , and  $\text{YH}_{1.77}$  in the range 300 K to 600 K, an oven consisting of resistive

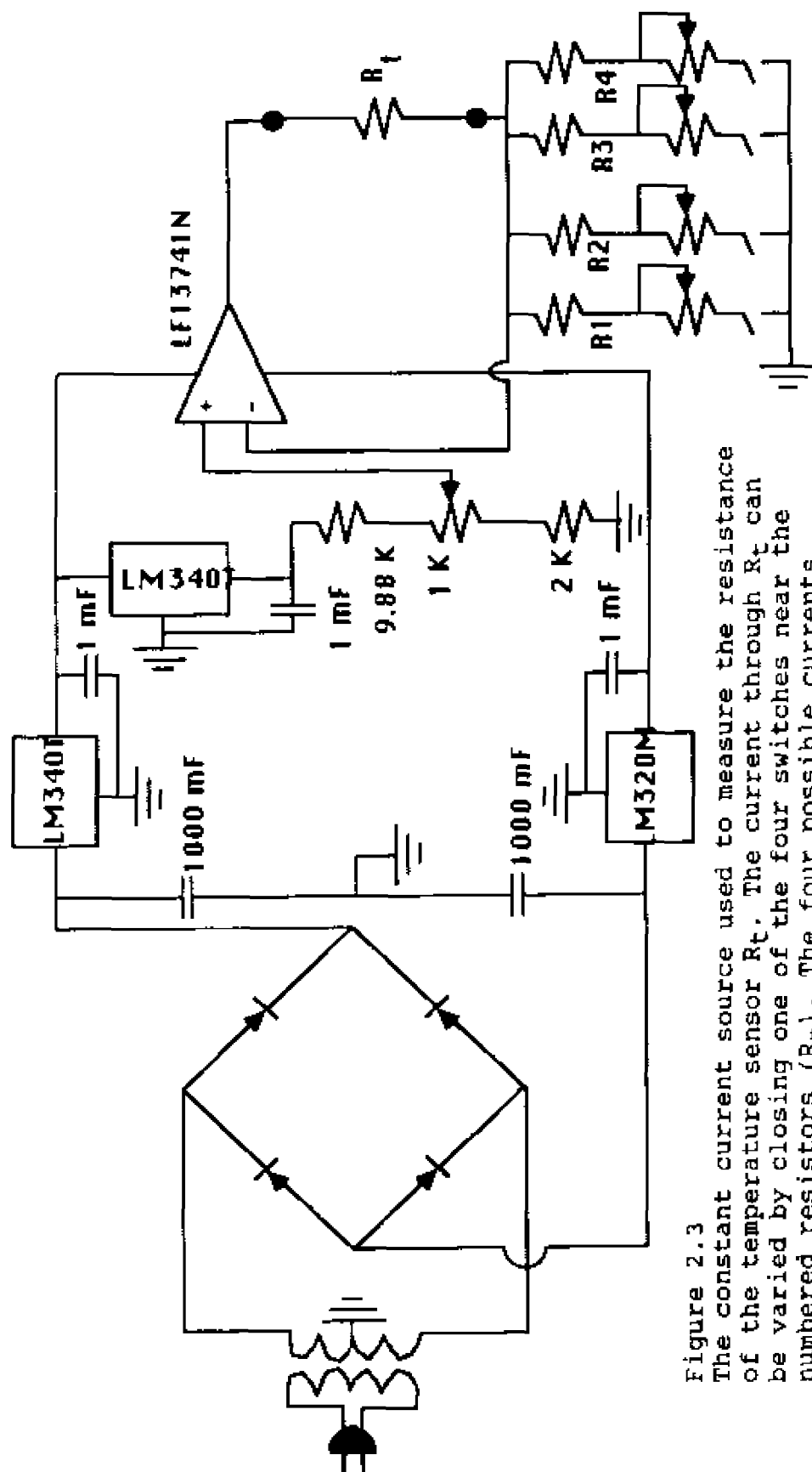


Figure 2.3  
 The constant current source used to measure the resistance of the temperature sensor  $R_t$ . The current through  $R_t$  can be varied by closing one of the four switches near the numbered resistors ( $R_n$ ). The four possible currents through  $R_t$  were  $1 \mu\text{A}$ ,  $10 \mu\text{A}$ ,  $100 \mu\text{A}$ , and  $1 \text{ mA}$ .



wire (chromel-constantan) wrapped around an aluminum frame was used. A chromel-constantan thermocouple with an ice reference junction was used to measure the temperature.

The study of these hydride compounds necessitated the use of zero-, longitudinal-, and transverse-field  $\mu$ SR measurements. Zero-field  $\mu$ SR requires that the fields perpendicular and parallel to the initial muon spin be extremely small. This was accomplished by placing field shimming coils on each of the six sides of the cryostat. The control system for each coil consisted of a variable-voltage power supply and a circuit to regulate the current through the coil (Fig. 2.4). The current in each coil was adjusted to yield a magnetic field of less than 0.2 Gauss at the sample. The variance of the field across the sample was 0.05 Gauss or less. These field shimming coils were checked, and the current adjusted periodically over the typical four to six weeks of beam time. These coils were also used during the low longitudinal- and transverse-field experiments. The longitudinal field experiments were performed using a set of coils placed on two sides of the cryostat such as to produce a magnetic field parallel to the polarization of the beam. The coils were capable of producing a fourteen gauss field with an input of 50 amperes. The transverse field was produced by a pair of coils with a six inch gap (Fig. 2.2). The nominal value for the field was 150 gauss. All field measurements were made using a Hall probe.

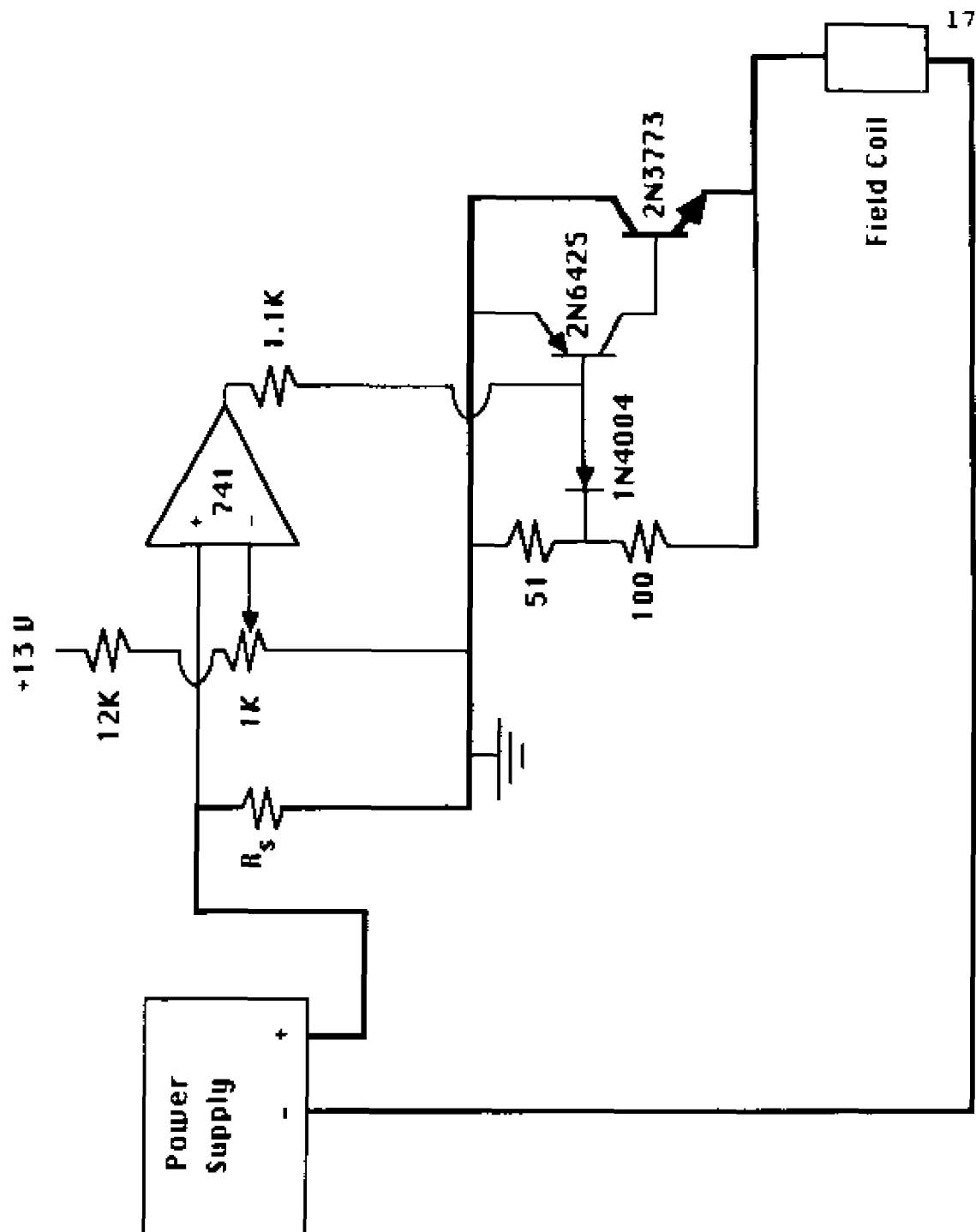


Figure 2.4  
 The control circuit for a field shimming coil. The current through a shimming coil is provided by the voltage-regulated power supply. This current generates a potential difference across  $R_s$  (a piece of manganin wire, which has a small  $dR/dT$ ) which is then compared to a reference voltage set by a potentiometer. This allows a constant current to flow through the field shimming coil.

## 2.4 PREPARATION OF SAMPLES

### A. Sample Cells

The metal hydrides used in the  $\mu$ SR studies were powders which necessitated the use of a sample cell to hold them. Each sample consisted of 20 to 30 grams of material. The cell used for the  $\text{TiH}_{1.99}$  sample consisted of aluminum foil wrapped around the powder. This was adequate for this sample, since titanium hydride is stable and the temperature range of the experiment did not cause the compound to outgas. For  $\text{ZrH}_{1.94}$  and  $\text{YH}_2$ , the sample cell was a square aluminum frame of 0.7 cm thickness and 3 cm on each side with mylar windows. The sample, after adding hydrogen, was loaded in the cell under vacuum. The sample cells for  $\text{TiH}_{1.83}$ ,  $\text{TiH}_{1.97}$ ,  $\text{YH}_{1.77}$  and  $\text{LaH}_{2.06}$  had stainless steel foil hard soldered onto a stainless steel ring of 1 cm thickness and 3 cm diameter. These samples were loaded under a helium gas atmosphere through a neck attached to the side of the stainless steel ring. This neck was internally threaded which allowed a stainless steel screw and a soft copper washer to seal this system. The helium gas allowed good thermal contact.

### B. Samples

In the fabrication of a metal hydride sample, one starts with a pure metal and pure  $\text{H}_2$  gas. The distributors

and the impurities of the materials used for the preparation of our samples are listed below. The lanthanum used in this study was obtained from the Materials Preparation Center at Ames Laboratory. The spark source mass spectrometric analysis of the lanthanum yielded the following major impurities at less than 20 atomic ppm: Al, F, Nb, Y, and Ce. No mention of the oxygen content was made. The titanium used was obtained from MRC Corporation and was of VP grade (99.94% purity). The typical analysis of the material (which was an average over several lots) showed the following major impurities: oxygen at 600 ppm/weight and carbon, nitrogen, iron, and silicon at less than 75 ppm/weight. The zirconium used was obtained from Alfa Products in the form of a 3N5 (99.95% purity) crystal bar. The typical analysis showed the following major impurities: iron at 120 ppm/weight, titanium and hafnium at 75 ppm/weight, and oxygen, tantalum, niobium, and chromium at 50 ppm/weight. The yttrium used was obtained from Johnson Matthey in the form of a 4N (99.99% purity) ingot. The analysis of this material by the manufacturer yielded the following major impurities: lutetium at 50 ppm/weight and lanthanum and aluminum at 10 ppm/weight. The impurity levels of gases such as nitrogen and oxygen were not specified. The titanium and lanthanum were hydrided using H<sub>2</sub> gas (99.999% purity) obtained from the Matheson Company. The purity of the H<sub>2</sub> gas used to hydride the zir-

conium and yttrium metals was not specified by the supplier.

The  $TiH_x$  and  $LaH_{2.06}$  samples were prepared by J. J. Reilly under the following procedure. The metals were heated to 573 K under vacuum and allowed to outgas to clean their surfaces. At this point,  $H_2$  gas was introduced. If no hydrogen was absorbed, the metal was heated to about 700 K and maintained until absorption took place. The change in the hydrogen pressure during the reaction allowed a crude determination of the hydrogen concentration in the sample. Upon completion, the samples were allowed to cool to room temperature and then removed from the furnace. After the sample cooled, a small amount of the material was taken for hydrogen analysis by thermal decomposition. This method determines the hydrogen concentration to within an accuracy of one percent by measuring the pressure change in a small volume from the outgassing of hydrogen.

The  $ZrH_{1.94}$  and  $YH_2$  samples were prepared by E. F. W. Seymour in the following manner. Initially the hydriding system was evacuated. After evacuation, the system was filled with hydrogen to a pressure of approximately one atmosphere as measured by a mercury manometer to within an accuracy of one percent. After this, the hydrogen inlet valve was closed, and the valve at the top of the furnace was opened. Using this furnace, the sample was heated to several hundred degrees Celsius while monitoring the

hydrogen pressure in the system. After a sufficient pressure change, the sample was allowed to cool to room temperature. The hydrogen content of the sample was calculated from the difference between initial and final readings of the manometer. To reduce the error in pressure readings due to the finite volume between the valve on the furnace and the sample, a one liter reservoir was incorporated into the system. The hydriding system was also equipped with a titanium sponge. This element acts to purify the hydrogen by absorbing the gas from the cylinder of  $H_2$ . This sponge is then gently heated to give a pure source of hydrogen. This method is a standard trick in the field of hydrogen alloying to achieve high purity  $H_2$ , but the purity of this particular system has not been determined by E. F. W. Seymour. It should be mentioned that this system has been used to hydride samples for NMR work and has not yielded a problem due to impurities arising from the  $H_2$  gas or titanium sponge.

Yttrium dihydride is unstable at room temperature under atmospheric conditions. The hydrogen concentration of the sample is reduced by the formation of water vapor. During the transfer of  $YH_2$  from one sample cell to another, the hydride was accidentally exposed to the atmosphere. The concentration of this sample was then checked by thermal decomposition and found to have a H/Y ratio of 1.77. No impurities were expected to have been added during this period of exposure.

## CHAPTER 3

### INTERACTIONS OF THE MUON WITH THE LATTICE

In the first chapter, the large magnetic moment of the muon was stated to be advantageous. This allows internal fields and spin dynamics of the host to be measured and the site of occupation for the muon to be determined. These measurements or determinations involve magnetic, electronic and elastic interactions with the lattice. However, one must ask the question whether the muon with a momentum of 100 MeV/c affects the lattice and the quantity being measured.

In this chapter, we will first explore the effects of thermalization of the muon on itself and the lattice. Upon examining this, the three interactions listed above will be discussed.

#### 3.1 THERMALIZATION<sup>7</sup>

For  $\mu$ SR to be considered a differential technique, the muon must have a kinetic energy of the order of  $kT$ . The thermalization of a high energy muon (~40 MeV) raises two (and possibly more) questions.

1. Is the muon still polarized after it thermalizes?

- ii. Does the muon damage the lattice during thermalization? If so, is the information collected a representative of an undamaged lattice?

Let us consider the first question. The kinetic energy of the incoming muon is significantly higher than the energy of the lattice ( $kT \approx 0.04$  eV). The loss of this energy occurs via inelastic scattering with electrons until the muon energy reaches 2-3 keV. This process happens in  $10^{-9}$ - $10^{-10}$  seconds. At this point in nonmetals, electron capture and loss by the muon occurs reducing its energy to approximately 200 eV in a matter of  $5 \times 10^{-13}$  seconds. The muon-electron system, known as muonium, becomes stable at this point. Following this, the muonium loses energy by inelastic collisions with atoms in the lattice. In metallic systems (including metal hydrides) the muonium state is not stable due to screening by the large number of conduction electrons. Therefore, the muon continues to lose energy via inelastic electron scattering until it thermalizes with the lattice.

Let us consider the effect of thermalization upon the polarization of the muon. The muon-electron scattering should be the dominant depolarization mechanism. Ford and Mullin<sup>8</sup> have calculated the cross section for scattering of longitudinally polarized muons on unpolarized electrons and discovered that the depolarization is proportional to the fractional energy loss,  $U$ .



$$U = (m_e/m_\mu)\beta^2 \sin^2(\alpha/2), \quad (3.1)$$

where  $\beta=v/c$  and  $\alpha$ = center of momentum scattering angle. The constant of proportionality between the depolarization and  $U$  is  $\beta^2 m_e/m_\mu$  which means that the depolarization due to electrons for a 90 MeV/c muon ( $U \leq 0.003$ ) is negligible.<sup>8</sup> Since the loss of polarization due to coulomb scattering is of the same order or less,<sup>8</sup> the loss of polarization due to thermalization is insignificant.

The final question to consider is the damage to the lattice by the muon and the effect upon the information gathered. During thermalization, the muon ionizes and displaces host atoms. The creation of these defects must be a concern since their presence does not reflect the natural state of the material. There is a threshold energy for vacancy creation meaning that the atom displacements do not occur during the last part of the muon's path. Brice<sup>9</sup> has calculated the range of the muon past the last displaced atom for various materials assuming a sharp threshold energy  $E_d$  (Fig. 3.1). One sees that the muon continues a considerable distance past the displaced atoms. The chance that the muon diffuses back to the damaged region is extremely small, as is the chance that a second muon finds the damaged region before the annealing out of the defects. One can conclude that the thermalization does not affect the polarization of the muon or the quantities measured.

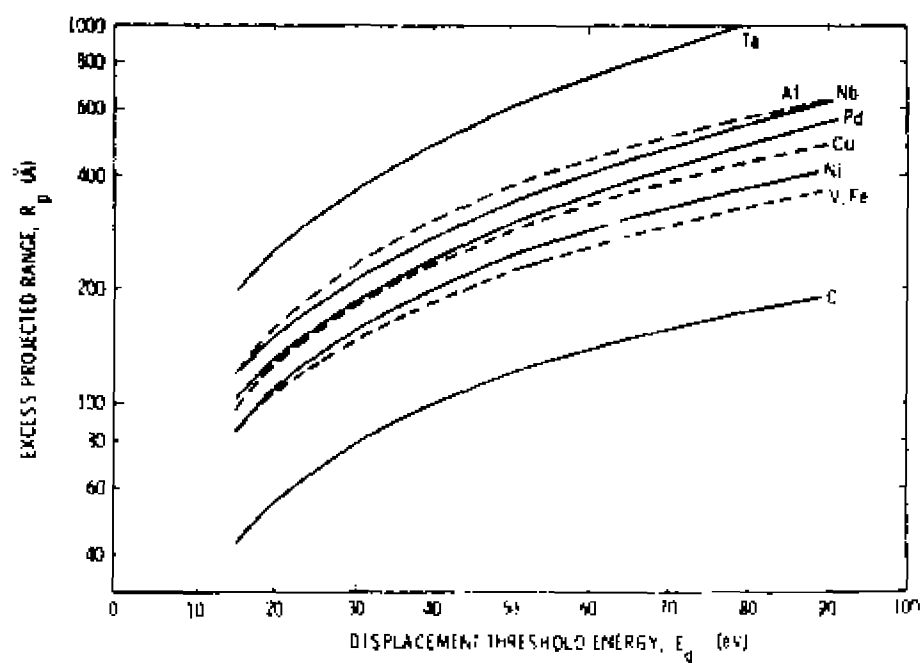


Figure 3.1 (Brice<sup>9</sup>)  
 Excess projected range for the muon as a function of displacement energy for positive muons incident on various materials.

### 3.2 MAGNETIC INTERACTION

#### A. Spin Precession<sup>10</sup>

The large magnetic moment of the muon makes it useful for studying magnetic ordering, Knight shifts, spin glass behavior and many other topics which involve the internal fields of the sample. Classically, the magnetic moment is due to a body of charge spinning around an axis with its magnitude proportional to this current. Since the charge for the muon is positive, the angular momentum,  $\vec{J}$ , and the magnetic moment,  $\vec{\mu}$ , lie along the same axis. Therefore:

$$\vec{\mu} = \gamma \vec{J} \quad (3.2)$$

The gyromagnetic ratio,  $\gamma$ , for a muon is 85.16 kHz/G. The equation of motion for a magnetic moment in a constant magnetic field,  $H_0$ , with no damping is

$$\frac{d\vec{J}}{dt} = \vec{\mu} \times \vec{H}_0 \quad (3.3)$$

or alternatively

$$\frac{d\vec{\mu}}{dt} = \gamma \vec{\mu} \times \vec{H}_0. \quad (3.4)$$

This equation states that the time rate of change of the direction of the magnetic moment is proportional to the field and is perpendicular to  $\vec{\mu}$  and  $\vec{H}_0$ . This is graphical-

ly depicted in Fig. 3.2. In this figure, the magnetic field lies on the z-axis and the magnetic moment is a vector with components  $(\mu \sin\theta \cos\phi, \mu \sin\theta \sin\phi, \mu \cos\theta)$ . Solving this equation, one finds

$$\theta = \text{Constant} \quad (3.5)$$

$$\text{and } \frac{d\phi}{dt} = \gamma H_0 = \omega_L \quad (3.6)$$

The motion of the spin is uniform around the axis of the magnetic field with the z component of  $\vec{\mu}$  remaining constant. This motion is known as Larmor precession. The magnetic moment vector may be written

$$\vec{\mu} = (\mu \cos(\omega_L t) \sin\theta, \mu \sin(\omega_L t) \sin\theta, \mu \cos\theta). \quad (3.7)$$

If a frictional force is present, the moment will have a spiral motion until it aligns with the field. The rate of change for the z-component of the magnetic moment is governed by the friction in the system.

Let us consider the quantum mechanical picture of the same system. Since the muon is a quantum mechanical particle, the rotating charge is actually intrinsic angular momentum, otherwise known as spin. For a single spin  $\vec{I}$  in an external field oriented along the z-direction, the Hamiltonian is

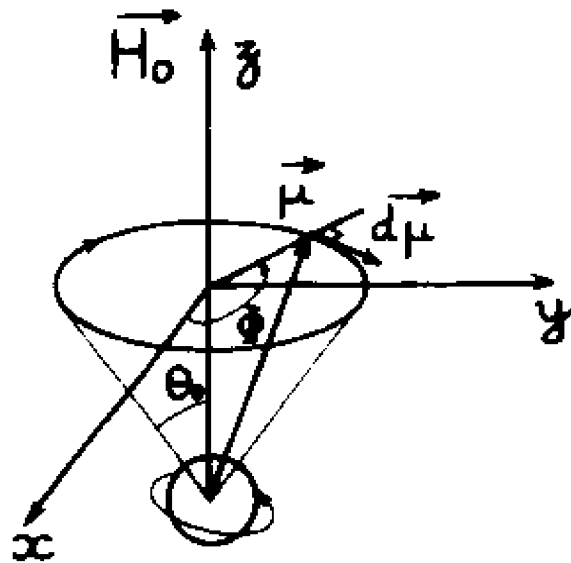


Figure 3.2 (Volino<sup>10</sup>)  
 The precession of the muon magnetic moment,  $\vec{\mu}$ , in an external field  $\vec{H}_0$ .

$$H_z = -\vec{\mu} \cdot \vec{H}_0 = -\gamma H_0 I_z. \quad (3.8)$$

The  $2I+1$  eigenstates of  $H_z$  are those labelled by the quantum number  $m$  and have an energy spacing of  $\hbar\gamma H_0 = \hbar\omega_L$ , where  $\omega_L$  is the classical precession frequency.

Let us proceed to find the expectation value of the different components of  $\vec{\mu}$ . Initially, we pick a state which is a superposition of the eigenstates of the Zeeman Hamiltonian

$$|\psi(0)\rangle = \sum_m a_m |m\rangle \quad (3.9)$$

$$\text{where } \sum_m |a_m|^2 = 1 \quad (3.10)$$

In the Schrödinger representation

$$|\psi(t)\rangle = \sum_m a_m \exp(-iE_m t/\hbar) |m\rangle. \quad (3.11)$$

The time dependent expectation value of a physical quantity for this representation is

$$\langle U(t) \rangle = \langle \psi(t) | U | \psi(t) \rangle. \quad (3.12)$$

Thus the expectation value of  $\mu_y(t)$  is

$$\langle \mu_y(t) \rangle = \langle \psi(t) | \mu_y | \psi(t) \rangle \quad (3.13a)$$

$$= \sum_{mm'} \hbar\gamma a_m a_m^* \exp(-i(E_m - E_{m'})t/\hbar) \langle m' | I_y | m \rangle. \quad (3.13b)$$

The quantity  $\langle m' | I_y | m \rangle$  is zero unless  $m-m' = \pm 1$ . Thus,  
 $(E_m - E_{m'})/\hbar = \pm \omega_L$ . Restricting ourselves to spin 1/2 particles (i.e. muon), the matrix element can be rewritten as

$$\langle -\frac{1}{2} | I_y | \frac{1}{2} \rangle = -\langle \frac{1}{2} | I_y | -\frac{1}{2} \rangle = -(1/2i) \langle \frac{1}{2} | I_+ | -\frac{1}{2} \rangle \quad (3.14)$$

$$= 1/2i \quad . \quad (3.15)$$

$$\text{Assuming } \langle m' | I_{\pm} | m \rangle = [I(I+1) - m(m\pm 1)]^{\frac{1}{2}} \delta_{m', m\pm 1} \quad (3.16)$$

Eqn. 3.13 may now be rewritten as

$$\langle \mu_y(t) \rangle = \hbar \gamma / (2i) (a_{\frac{1}{2}}^{\dagger} a_{-\frac{1}{2}} e^{-i\omega_L t} - \text{c.c.}) \quad (3.17)$$

where c.c. is the complex conjugate of the first term. If the coefficients  $a_{\frac{1}{2}}$  and  $a_{-\frac{1}{2}}$  are chosen such that

$$a_{\frac{1}{2}} = c_1 e^{i\phi} \quad (3.18)$$

$$a_{-\frac{1}{2}} = c_2 e^{i\theta} \quad (3.19)$$

$$\text{where } c_1^2 + c_2^2 = 1, \quad (3.20)$$

this gives

$$\langle \mu_y(t) \rangle = \hbar \gamma c_1 c_2 \sin(\phi - \theta + \omega_L t). \quad (3.21)$$

Similarly

$$\langle \mu_x(t) \rangle = \hbar \gamma c_1 c_2 \cos(\phi - \theta + \omega_L t) \quad (3.22)$$

$$\langle \mu_z(t) \rangle = \hbar \gamma (a^2 - b^2) / 2 \quad (3.23)$$

These expressions show that the z component of  $\vec{\mu}$  is a constant and that the x and y components oscillate at a frequency equal to the Larmor frequency. This is what was found in the classical picture.

### B. Origins of Magnetic Field at the Site of the Muon<sup>4</sup>

In the previous section, the precession of the muon spin in a magnetic field was introduced. In this section, the various magnetic fields at the site of the muon will be examined. The magnetic field at the site of the muon,  $\vec{B}_\mu$ , can be written (Fig. 3.3) as

$$\vec{B}_\mu = \vec{B}_{\text{ext}} + \vec{B}_{\text{hf}} + \vec{B}_{\text{dem}} + \vec{B}_L + \vec{B}_{\text{dip}} \quad (3.24)$$

$\vec{B}_{\text{ext}}$  arises from sources external to the sample. The magnetic fields arising from the magnetization of the sample can be described by a Lorentz sphere around the muon. This tool separates the sample into two regions. Inside the sphere, the sources of the fields are treated microscopically; while outside the sphere, they are treated in a continuum limit.  $\vec{B}_L = (4\pi/3)\vec{M}$ , the Lorentz cavity field, is the field inside an empty sphere in a medium of uniform magnetization  $\vec{M}$ .  $\vec{B}_{\text{dem}} = -N\vec{M}$  is the shape dependent demagnetization field. The shape of the sample is incorporated via the constant,  $N$  (see reference 10).  $\vec{B}_{\text{dip}}$  is the magnetic field due to nuclear dipoles inside the Lorentz sphere.  $\vec{B}_{\text{hf}}$  is the hyperfine field due to the polarization of the electrons surrounding the muon. The Pauli paramagnetic susceptibility of conduction electrons is given by<sup>12</sup>

$$\chi = N\mu_B^2/kT_F. \quad (3.25)$$



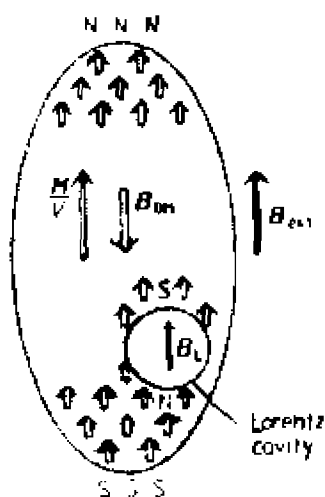


Figure 3.3 (Schenck<sup>4</sup>)

Macroscopic magnetic field inside a magnetized ellipsoidal sample in an external field applied parallel to the long axis of the ellipsoid.  $M$  is the magnetization.  $B_{DM}$  ( $B_{dem}$ ) and  $B_L$  are the demagnetization and Lorentz cavity fields, respectively. The static component of the individual magnetic moments induced by the field are denoted by the small arrows. Not shown is the hyperfine field  $B_{hf}$ .

where  $N$ ,  $\mu_B$ ,  $k$  and  $T_F$  are the number of conduction electrons, the Bohr magneton, the Boltzmann constant and the Fermi temperature, respectively. The presence of the muon may enhance the susceptibility of the conduction electrons by a factor of ten.

For diamagnetic materials,  $\vec{B}_{hf}$ ,  $\vec{B}_L$ , and  $\vec{B}_{dem}$  can be neglected since they are two to three orders of magnitude less than  $\vec{B}_{ext}$  ( $\sim 150$  G). Therefore,  $\vec{B}_{ext}$  and  $\vec{B}_{dip}$  are the only fields which contribute for the studies presented. The effects of dipolar field upon the muon spin will be discussed in more detail in the next section.

### C. Dipolar Interaction<sup>10</sup>

The classical interaction between two magnetic dipole moments  $\vec{\mu}_1$  ( $\gamma\hbar\vec{I}_1$ ) and  $\vec{\mu}_2$  ( $\gamma\hbar\vec{I}_2$ ) can be written as

$$H_{dd} = 1/r^3 [\vec{\mu}_1 \cdot \vec{\mu}_2 - 3(\vec{\mu}_1 \cdot \hat{r})(\vec{\mu}_2 \cdot \hat{r})] \quad (3.26)$$

where  $\vec{r}$  is the vector between the two dipoles (and  $\hat{r} = \vec{r}/r$ ). Working in spherical coordinates, this Hamiltonian can be rewritten as

$$H_{dd} = \hbar^2 \gamma_1^2 \gamma_2^2 / r^3 [A + B + C + D + E + F] \quad (3.27)$$

where

$$A = I_{1z} I_{2z} (1 - 3\cos^2\theta) \quad (3.28)$$

$$B = -1/2 [I_1^+ I_2^- + I_1^- I_2^+] (1 - 3\cos^2\theta) \quad (3.29)$$

$$C = D^* = -3/2[I_1^+ I_{2z} + I_{1z} I_2^+] \sin\theta \cos\theta e^{-i\phi} \quad (3.30)$$

$$E = F^* = -3/4 I_1^+ I_2^+ \sin^2\theta e^{-2i\phi} \quad (3.31)$$

This Hamiltonian may also be written as

$$H_{dd} = -\bar{\mu}_1 \cdot \bar{H}_d \quad (3.32)$$

where  $\bar{H}_d$  is the field produced by a second dipole (nucleus). For most nuclei, this field is on the order of a couple gauss. A distribution of dipolar fields at crystallographically equivalent sites arises from averaging over the lattice locations and spin orientations of the remaining nuclei. This range of fields gives rise to a distribution of Larmor frequencies as shown in Fig. 3.4 which is characterized by a quantity known as the line width. Determination of this distribution gives information about the muon position and the orientation of the local spins. This Hamiltonian will be used to calculate the Gaussian line width in the Zeeman and quadrupolar limits in chapter 5.

### 3.3 ELECTRONIC INTERACTION

In the previous section, the magnetic interaction of muons was emphasized. This interaction is usually the "star of the show" in the data analysis while the electronic effects are often swept under the rug. However,  $\mu$ SR can measure or observe many electronic effects: the sites available for muon occupation, elastic forces and lattice

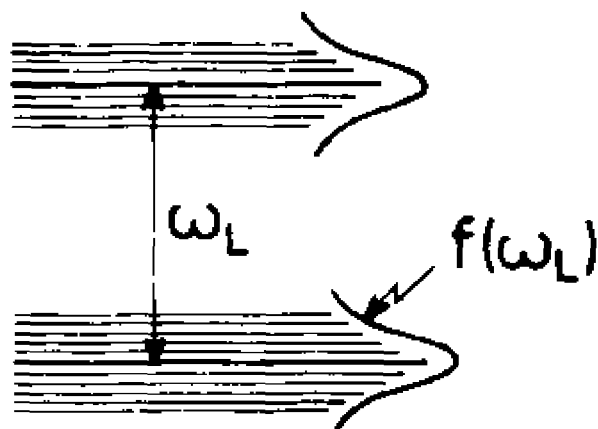


Figure 3.4 (Volino<sup>10</sup>)  
Distribution of energy levels due to the dipolar interaction. The figure also shows the difference in energy levels due to the Zeeman interaction.

expansions around the muon, the electric field gradient at neighboring nuclei due to the muon and its screening cloud, Knight shifts (which are a measure of the polarization of the local electrons due to an external field) and the magnetic hyperfine fields in ordered materials from the polarization of the local electrons (which are coupled by exchange forces to the local magnetic moments). This section will begin with a discussion of selection of sites for muon occupation followed by a discourse on elastic forces and lattice expansions. This will be followed by a discussion on the interaction of nuclear quadrupole moments with the electric field gradient produced by the muon. The effects due to the polarization of the local electrons by external fields or local magnetic moments will not be discussed here. The reader is referred to reference 4 for a treatment of these topics.

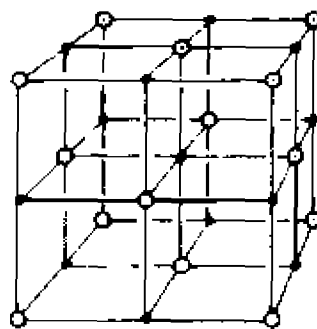
#### A. Selection of Sites for Occupation

The electronic interaction is an integral part of the site selection process. The potential for the lattice may be viewed as a superposition of potentials from the atomic cores. In metals, the conduction electrons are free to adjust themselves when a perturbation, such as muon's charge, is present. This superposition of potentials gives rise to potential minima for positive particles. These minima are known as octahedral (O) and tetrahedral (T) interstitial sites. For the case of a Face Centered Cubic

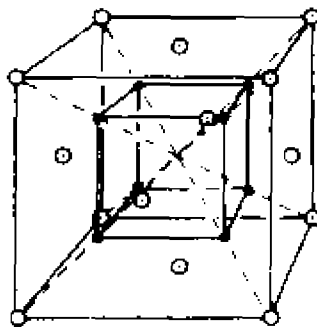
(FCC) lattice, there exist two T sites and one O site for each unit cell (Fig. 3.5). The interstitial sites of octahedral symmetry in a FCC lattice form a FCC lattice of their own. This lattice of interstitial O sites is displaced by  $a/2$  ( $a$ =lattice constant) along a (100) direction. The interstitial sites of tetrahedral symmetry in a FCC form a simple cubic (SC) lattice of their own. This lattice is displaced by  $a\sqrt{3}/4$  along the diagonal of the cube. The hydrogens, in the dihydride phase of this study, occupy the majority of these T sites. They form either a simple cubic or a distorted SC lattice. If the hydrogens occupy T sites, one can add the potentials for a SC and FCC lattice to obtain a first-order picture of what the muon sees in terms of a charge density. Fig. 3.6 is the charge density for the 110 direction of  $(\beta\text{-La})^{14}$ , a typical FCC lattice. The four tetrahedral sites in this figure are located at  $x=1/4$  and  $3/4$  and  $y=1/\sqrt{8}$  and  $3/\sqrt{8}$  positions. The octahedral sites are located along  $x=1/2$  line for  $y=0, 1/\sqrt{2},$  and  $\sqrt{2}$ . The presence of the hydrogen atoms and the muon will perturb the charge density, but Fig. 3.6 serves merely to demonstrate the symmetry of the interstitial sites for FCC lattices.

## B. Screening

In the section on magnetic fields, it was mentioned that the muon has a screening cloud around it. The mean radius of this screening cloud  $r_s$  for a free electron gas



a)



b)

Figure 3.5a-b (Schroeder<sup>13</sup>)  
Interstitial sites (closed circles) in FCC lattices (open circles). a.) interstitial sites of octahedral symmetry (O sites). b.) interstitial sites of tetrahedral symmetry (T sites).

## FCC(110) Charge Density

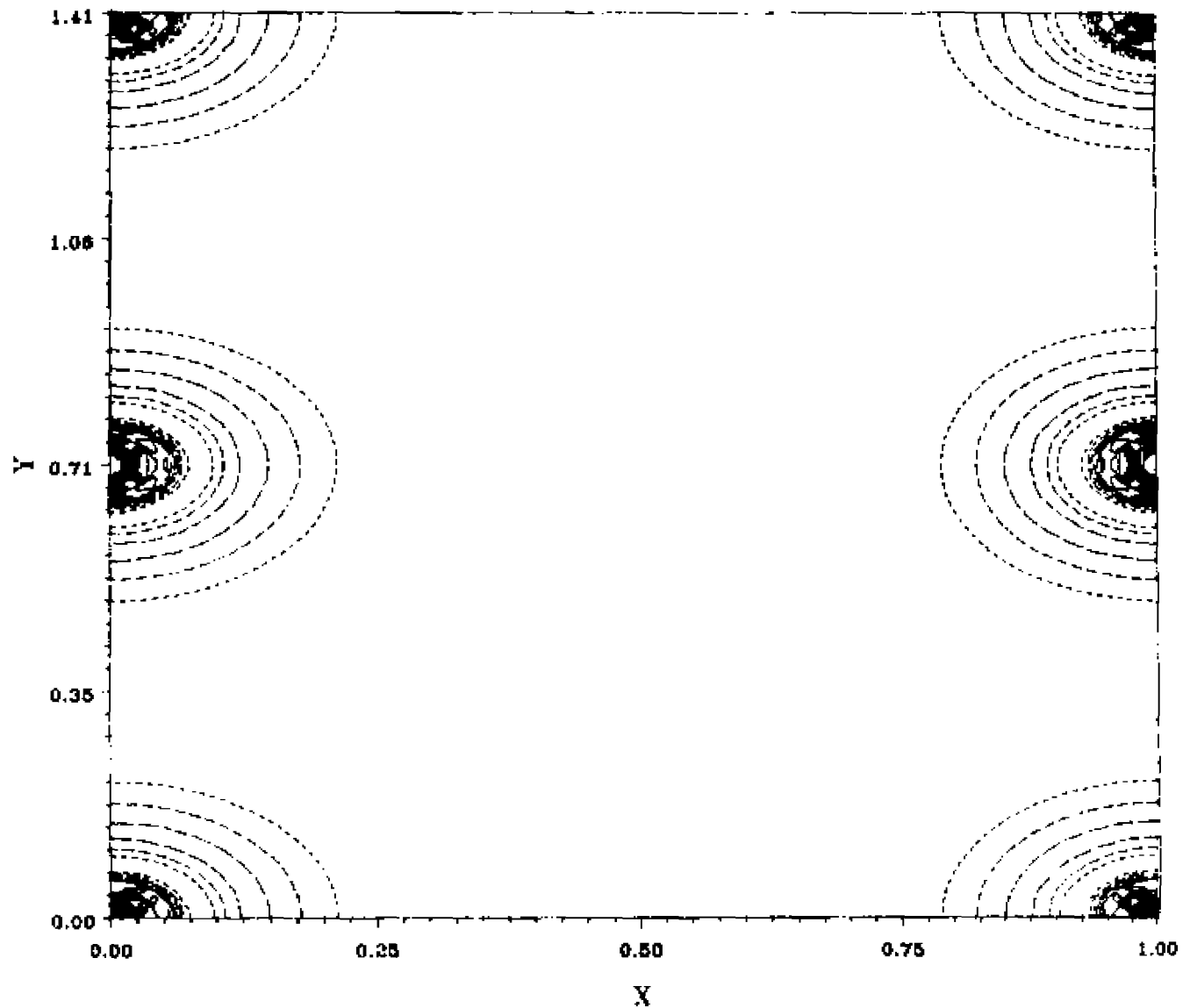


Figure 3.6 ( $\text{Lu}^{14}$ )  
Contour plot of the charge density of  $\beta$ -La, a typical FCC  
lattice, in the (110) plane.



is dependent upon the density of electrons at the Fermi surface  $n_0(E_f)$  and is<sup>3</sup>

$$r_s = \left( \frac{E_f}{6\pi n_0(E_f) e^2} \right)^2 \quad (3.33)$$

For most metals,  $n_0(E_f)$  is in the range  $10^{22} - 10^{23} \text{ cm}^{-3}$  which yields a value of approximately one angstrom for this radius. This means that most of the screening occurs for distances less than the muon nearest-neighbor length. However, this perturbation does cause RKKY-oscillations of charge and spin densities over a couple lattice constants.

Since muonium has not been found in metals, the possibility that two electrons of opposite spin states bind to the muon, like  $\text{H}^-$ , has been considered by many theorists. Jena et al.<sup>15</sup> have used a jellium model, where a uniform positive background is substituted for the periodicity of the positive metal atoms to calculate normalized charge density  $n(r)/n_0$  and spin density enhancement curves for free electrons as a function of distance from a muon as shown in Fig. 3.7.

$$\eta = (n^\uparrow(r) - n^\downarrow(r)) / (n_0^\uparrow - n_0^\downarrow) \quad (3.34)$$

These curves were calculated in the Hohenberg-Kohn-Sham formalism which involves solving for the local wavefunction and potential self-consistently.<sup>15</sup> Jena et al.<sup>15</sup>

found that the potential for metals would allow for bound states, but that the binding energies for the muonium state would be smaller than the electron-electron interactions.

### C. Elastic Forces

Elasticity of materials is characterized by a linear restoring force with the provision that the elastic limit of the material is not exceeded. This is often associated with a child's happiness with a spring and is not a stranger to most people. Lattices also possess this same characteristic. For the muon, there is "pushing" and "shoving" between it and the lattice.

Teichler<sup>16</sup> has considered the problem of local lattice distortions in copper for an octahedral interstitial muon screened by conduction electrons. Using the potential  $V(R-R_1)$  shown in Fig. 3.8 (which includes terms for interactions between  $\mu^+$  at position  $R$  and a  $\text{Cu}^+$  ion at position  $R_1$  and interactions between the screening electrons and each positive ion ( $\mu^+$  and  $\text{Cu}^+$ )), he calculates the coupling strength  $g$  with the copper neighbors.

$$g(R-R_1) = - \nabla_{R_1} \int d^3r |\psi_\mu(r-R)|^2 V(r-R_1) \quad (3.35)$$

Using a potential energy  $U(R)$  for an unrelaxed FCC lattice of fourteen shells of  $\text{Cu}^+$  ions around an octahedral interstitial site, the muon wave function  $\psi_\mu$  was estimated. The

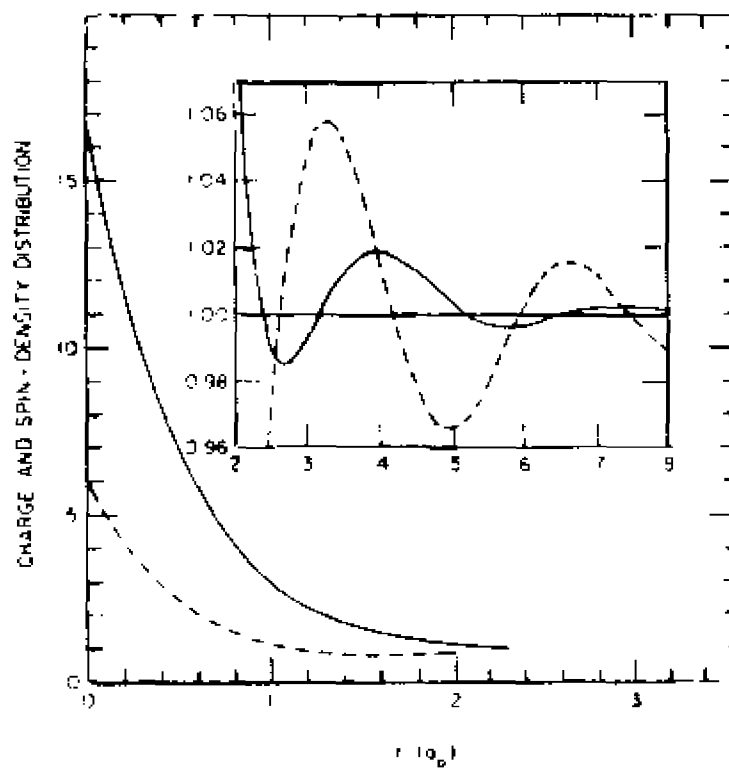


Figure 3.7 (Jena et al. 15)  
 Charge- and spin-density distribution around a positive muon in a spin-polarized electron gas with  $r_s = 2 a_0$  and  $(n_{\uparrow} - n_{\downarrow}) / (n_{\uparrow} + n_{\downarrow}) = 0.17$ . The dashed and solid curves represent the normalized spin density and normalized charge density, respectively.

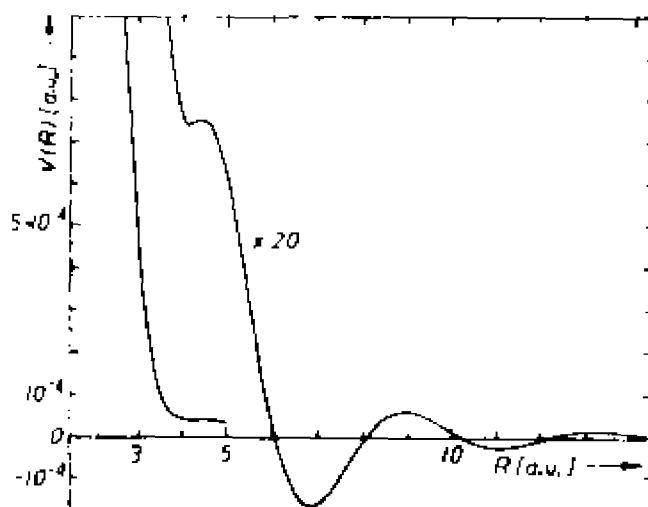


Figure 3.8 (Teichler<sup>16</sup>)  
Interaction potential  $V(R)$  between positive point charges  
and  $\text{Cu}^+$  ions in Cu metal.

results for this calculation are shown in Table 3.1 along with the results for other isotopes of hydrogen. Included in this table is the harmonic oscillator frequency for  $U(R)$ . Teichler has used the coupling strength  $g$  to obtain radial static distortions  $\delta u$  around the muon in the harmonic oscillator approximation using the "lattice response function" of copper.<sup>16</sup> The deformation energy (polaron binding energy),  $E_0$ , reported is a measure of the decrease in muon energy due to the relaxation of the copper

TABLE 3.1<sup>16</sup>

Energy levels, lattice coupling, lattice distortion, and lattice relaxation energy for polaronic motion of proton isotopes in copper.

	$\hbar\omega$ (meV)	$g$ (eV/a)	$\delta u / (a/2)$	$E_0$ (meV)
$\mu^+$	356	2.0	0.03	90
p	120	1.34	0.02	40
d	84.5	1.27	0.02	36
t	69	1.23	0.02	34

lattice. These calculations agree with the  $\mu$ SR experiments of Camani et al.<sup>17</sup> and show that a muon distorts the local lattice more than a proton.

#### D. Quadrupolar interaction<sup>10</sup>

For nuclei with spin greater than 1/2, the distribution of positive charge is not spherical. This nonspherical nature gives rise to an interaction with the elec-

tronic cloud produced by the muon. This distribution may be developed using the method of moments. Since the Wigner-Eckart theorem requires the expectation value of the electric dipole moment to vanish as a consequence of time reversal invariance, the first nonzero moment is the electric quadrupole.<sup>18</sup> The electric quadrupole moment,  $Q$ , for a spherical charge distribution, i.e. spin-0 or -1/2 nuclei, is zero.<sup>18</sup> This interaction can be expressed as a function of the electric quadrupole moment second rank tensor of the nucleus  $Q_{\alpha\beta}$  and the electric field gradient (e.f.g.) second rank tensor at the nucleus site due to the electronic cloud  $V_{\alpha\beta}$  due to the presence of the positive muon.<sup>4</sup>

$$H_Q = 1/6 \sum_{\alpha\beta} V_{\alpha\beta} Q_{\alpha\beta} \quad (3.36)$$

where  $Q_{\alpha\beta} = eQ/(6I(2I - 1)) [3(I_\alpha I_\beta + I_\beta I_\alpha)/2 +$

$$- \delta_{\alpha\beta} I(I + 1)] \quad (3.37)$$

$V_{\alpha\beta}$  is a function of the distance between the nuclei and the electronic cloud.

### 3.4 SUMMARY

The different interactions between the muon and the lattice have been presented in this chapter. The thermalization of the muon was shown not to affect its polarization or the quantities measured. Secondly, it was shown that the magnetic interaction is responsible for the precession of the muon's spin and the distribution of dipolar fields. Further, the electronic interaction was

shown to account for the selection of sites for muon occupancy, the electron cloud around the muon, the distortion of the lattice in the vicinity of the muon, and the interaction of the electric field gradient and the nuclear quadrupole moment. The relevance of these interactions to the different  $\mu$ SR techniques will be discussed in chapter 5.

## CHAPTER 4

### MUON DIFFUSION

Hydrogen isotopes (including the muon) have large mobilities in metals. At room temperature and below, the mobility of hydrogen is several orders of magnitude higher than any other interstitial atom. The question as to why this is true has stimulated the experimental and theoretical study of the diffusion mechanism. Due to the light mass of hydrogen isotopes, a quantum mechanical picture is often necessary to describe their motion. The large difference in mass ratios of the four hydrogen isotopes (muon, hydrogen, deuterium and tritium) allows a wide range of effects to be studied which is beneficial in differentiating between different diffusion mechanisms.

The diffusion of light interstitial particles can be described by one of four mechanisms (Fig. 4.1). The temperature of the lattice determines which mechanism is dominant. One should emphasize that these divisions are a simplified view of reality and that the boundaries which separate these processes are not necessarily sharp and may allow for overlap. At low temperatures, the interstitial particle is delocalized into a band state if it is not trapped by lattice defects. This motion is limited by



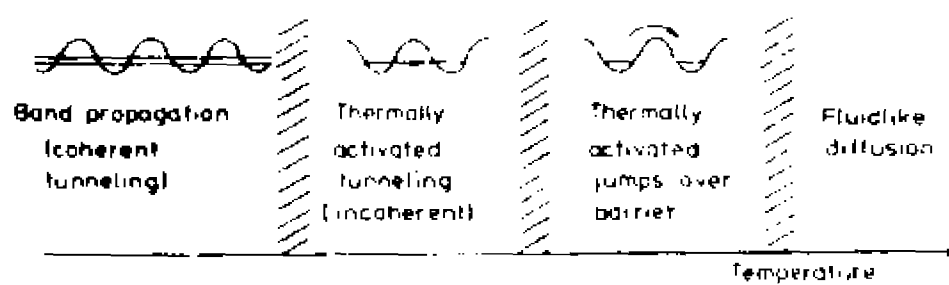


Figure 4.1 (Kehr<sup>19</sup>)  
Diffusion mechanisms for light interstitials as a function of temperature.

scattering with thermal phonons and lattice defects (and electrons in metals). For higher temperatures, the interstitial particle is self-trapped by the relaxation of the lattice around it. The particle and the distortion are known as a polaron. The particle is able to move to a crystallographically equivalent site when two or more phonons equalize the energies of the two sites. The restriction that the tunneling process between crystallographically equivalent sites not be a one-phonon process is imposed by conservation of momentum. This process is known as thermally-activated tunneling. The third mechanism is known as thermally-activated jumping and is characterized by a higher activation energy since the particle must overcome a potential barrier. This process usually dominates over tunneling at high temperatures. The fourth process which occurs is "fluid-like diffusion" where the particle is mainly in states above the potential barriers. Diffusion in this state is limited by collisions generated by the thermal fluctuations in the lattice. In this chapter, the thermally-activated diffusion processes will be discussed.

#### 4.1 THERMALLY-ACTIVATED TUNNELING<sup>4, 19, 20</sup>

Fig. 4.2 shows a schematic of the process of thermally-activated quantum tunneling. Initially the particle is self-trapped due to the relaxation of the lattice around the interstitial. Thermal fluctuations bring the

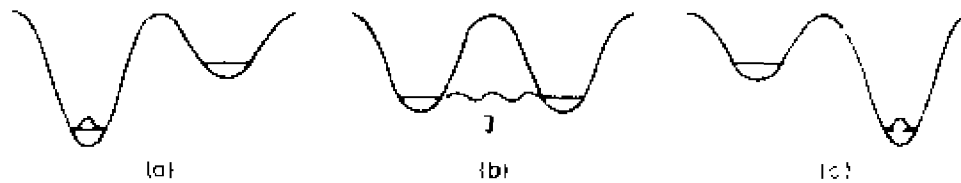


Figure 4.2 (Kehr<sup>19</sup>)  
Thermally-activated tunneling of a light interstitial. a.) The lattice is relaxed around the interstitial on the left side allowing the interstitial to have a lower energy. b.) Thermal fluctuations in the lattice have equalized the height of the levels in the two wells allowing a tunneling process to occur. c.) The lattice is relaxed around the new position of the interstitial.

two levels to the same energy. The particle is able to tunnel through the barrier with a tunneling matrix element  $J$ . After tunneling, the lattice relaxes around the new site of the interstitial particle. According to the "Golden Rule", one expects the transition rate  $\Gamma$  to a neighboring interstitial site to be of the form

$$\Gamma = J^2 \exp(-E_a/kT). \quad (4.1)$$

An excellent starting point for small-polaron hopping theory is to consider the tunneling matrix element as a perturbation of the Hamiltonian. In the evaluation of jump rates, the following assumptions are usually made in small-polaron theory:

- i) The interstitial particle responds to the host atoms adiabatically. This is a valid assumption as long as local mode frequencies of the muon are much greater than the Debye frequency of the host.
- ii) The coupling between the particle and a host atom is linear which means that the interaction energy is proportional to the displacement of the host atom. This allows the vibration spectra to be unaffected by the distortion.
- iii) The localized interstitial is associated with the unperturbed initial and final states. This allows the tunneling matrix element  $J$  to be viewed as a pertur-

bation. This is valid, because the lattice relaxation energy is much greater than  $J$ .

iv) The lattice potentials can be treated in the harmonic approximation.

v) The tunneling matrix element  $J$  is independent of the changes induced by the phonons. This is called the Condon approximation and allows the change in the barrier height due to the phonons to be neglected.

The use of the last assumption is sometimes questioned. This will be explored in more detail at the end of this section.

If transitions between sites are not allowed, then the localized states of the particle are eigenstates of the Hamiltonian. The tunneling matrix element produces transitions between these eigenstates and can be treated by a time-dependent perturbation theory. If the particle starts in site  $p$  with the lattice relaxed around it, then the probability for a transition to site  $p'$  with the lattice relaxed around it is

$$\Gamma_{pp'} = 2\pi/\hbar |\langle p\alpha | H | \alpha' p' \rangle|^2 \delta(E_{p\alpha} - E_{p'\alpha'}) \quad (4.2)$$

where  $\alpha$  and  $\alpha'$  are quantum numbers for the initial and final states, respectively. After summing over initial and final states and over the phonon states, the following results are obtained. For  $T > \theta_D$ ,<sup>19</sup>

$$\Gamma_{pp'}(T) = \frac{J^2}{\hbar} \left( \frac{\pi}{4E_a kT} \right)^{1/2} \exp(-E_a/kT). \quad (4.3)$$

This transition rate includes processes involving two or more phonons. For  $T \ll \theta_D$ , only two-phonon processes are expected. Hence,<sup>19</sup>

$$\Gamma_{pp'}(T) = 57600\omega_D \pi \frac{J^2 E_a^2}{(\hbar\omega_D)^4} \left( \frac{T}{\theta_D} \right)^7 \exp(-5E_a/\hbar\omega_D) \quad (4.4)$$

where  $\hbar\omega_D = k\theta_D$ .

$E_a$  is a measure of the energy to equalize the energy levels in the two wells (Fig. 4.2) and is equal to the relaxation energy (polaron binding energy)  $E_0$  (Section 3.3C) divided by two.

The tunneling matrix element,  $J$ , is introduced to allow delocalization of the particle over several sites. Frequently, the host atoms are considered to be fixed at their equilibrium positions. This is a reasonable approximation since the mass ratio between the host metal atom and interstitial particle is usually large. The potential produced by the host atoms may be replaced with a periodic one, such as a cosine function, which allows the calculation of band states. Since the bands are narrow for particles such as the muon, the wave functions are strongly localized. Thus, only transition matrix elements to the neighboring sites need to be considered. An order of magnitude estimate for  $J$  can be obtained by placing the light interstitial in a periodic one-dimensional potential

and calculating the energy splitting between the lowest (symmetric) and the first excited (antisymmetric) states. The wave function for a state is often a linear combination of harmonic oscillator wave functions. If the potential is

$$V(x) = (V_0/2)\cos(2\pi x/d), \quad (4.5)$$

where  $d$  is the spacing between wells and  $V_0$  is a barrier height, then the frequency of oscillation within the well is

$$\omega^2 = (2\pi)^2 V_0 / (2md)^2. \quad (4.6)$$

With this formula, one has the choice of calculating a barrier height from an experimentally determined vibration frequency or a vibration frequency from a measured barrier height, such as an activation energy.<sup>19</sup> If the well is deep ( $V_0 \gg \hbar\omega$ ), then an order of magnitude estimate for the tunneling matrix element is given by the Mathieu formula.

$$J = 8 \frac{\hbar^2}{2md^2} \left( \frac{2md^2 V_0}{\hbar^2} \right)^{3/4} \exp\left( -\frac{2d}{\pi\hbar} (2mV_0)^{1/2} \right) \quad (4.7)$$

The Condon approximation has been found to be a severe restriction in some cases. If the motion of the

interstitial involves a path which passes between two host atoms, these atoms must be displaced from their positions for the transition to occur. Since the distortion of the host lattice in this matter is not considered as part of the ground state, then the expression for the transition rate must be changed.<sup>19</sup>

$$\Gamma_{pp'}(T) = \frac{J^2}{4\hbar/(E_a E_g)} \exp(-E_a/kT) \quad (4.8)$$

The elastic energy  $E_g$  is the energy necessary to distort the lattice. This means that the Condon approximation is not valid since the phonons, necessary to distort the lattice, severely affect the barrier height. The elastic energy  $E_g$  has been found to contribute significantly for jumps between O sites in FCC metals and T sites in BCC metals, but not T sites in FCC metals.

#### 4.2 THERMALLY-ACTIVATED JUMPING<sup>12</sup>

Diffusion is characterized by a net flux of vacancies or particles through a solid. This net flux is often driven by a concentration gradient of vacancies or particles trying to distribute themselves uniformly in the solid. This phenomena is expressed by Fick's law for a concentration of  $N$  particles.

$$J_N = -D \nabla N \quad (4.9)$$



The net flux  $\bar{J}_N$  is the number of atoms crossing a unit area in a unit time. The constant  $D$  is the diffusion constant. The direction of the diffusion is away from areas of high concentration, but may also be driven by the gradient of the chemical potential (which has not been included in Eqn. 4.9).

For a particle to diffuse in the classical sense, the potential energy barriers imposed by the nearest-neighbor atoms must be overcome. The height of this barrier is indirectly determined by the mass of the particle. The potential well can be approximated by a harmonic oscillator potential. This means that the energy level spacing is proportional to  $1/\sqrt{m}$  with the lowest level occurring at  $(3/2)\hbar\sqrt{k/m}$  above the bottom of the well. For a particle in a well with a barrier height  $E$ , the fraction of time in which the interstitial will have enough energy to pass over the barrier is proportional to  $\exp(-E/kT)$ . This fraction reflects the general phonon spectrum in the lattice with the higher energy portion of this spectrum increasing in number as a function of increasing temperature. If the frequency of vibration in the potential well is  $\nu$ , then the probability for the particle to escape from the well is

$$p = \nu \exp(-E/kT). \quad (4.10)$$

This probability is also known as the jump frequency. The frequency of vibration is proportional to  $1/\sqrt{m}$ .

Let us consider two parallel planes, with occupied interstitial sites, separated by lattice constant  $a$ . If there are  $S$  interstitial particles in one plane and  $S + a \frac{dS}{dx}$  on the other, then the net number of atoms to diffuse between the planes per unit time is roughly  $-pa \frac{dS}{dx}$ . If the concentration of interstitial particles is  $N$ , then the number per unit area is  $S = aN$ . The diffusion flux is then

$$J_N = -pa^2 \left( \frac{dN}{dx} \right) \hat{i} \quad (4.11)$$

Using Eqns. 4.9, 4.10 and 4.11, one finds an expression for the diffusion coefficient.

$$D = \nu a^2 \exp(-E/kT) \quad (4.12)$$

In lattices where there are an extremely large number of interstitials, the diffusion constant will be reduced by a factor proportional to the percentage of vacant interstitial sites. This is known as a blocking factor and is commonly observed for protons in metal hydride systems such as  $TiH_x$ .<sup>21</sup>

It has been shown that the prefactor and the activation energy are inversely proportional to the square root of the mass of the interstitial particle. However, this

simplistic model is not a description of the true state of affairs. In reality, the anharmonic shape of the wells and the motion of the lattice atoms must be considered in the characterization of a diffusion constant.

## CHAPTER 5

### $\mu$ SR TECHNIQUES

For several years after the discovery of the parity violating weak decay of the muon, the only  $\mu$ SR technique used was transverse-field muon spin rotation. In the late 70s, zero- and longitudinal-field muon spin relaxation were developed at TRIUMF.<sup>22</sup> The invention of these techniques was beneficial to the study of internal fields in materials. Several other techniques, such as muon spin resonance<sup>23</sup> and level crossing resonance (LCR)<sup>24</sup> have since been added to the variety of  $\mu$ SR methods. Muon spin resonance can be used to study hyperfine fields and the time dependence of local fields.<sup>23</sup> LCR is useful in the study of nuclear hyperfine structure in paramagnetic spin systems.<sup>24</sup> This chapter is devoted to the discussion of transverse-, zero- and low longitudinal-field  $\mu$ SR techniques used in the present study of metal hydride systems.

#### 5.1 TRANSVERSE-FIELD TECHNIQUE

The number of positrons resulting from the decay of the muon is given by an exponential law for decay of a radioactive particle.<sup>7</sup>

$$N(t) = N_0 \exp(-t/r_\mu) \quad (5.1)$$

If the magnetic field is perpendicular to the spin, then the muon moment will precess at the Larmor frequency as mentioned previously. This means that the distribution of the emitted positrons will precess. Eqn. 2.6 is now rewritten as

$$W(\theta, t) = 1 + a \cos(\omega t + \phi). \quad (5.2)$$

Grouping together these two equations, one has

$$N(t) = N_0 \exp(-t/r_\mu) (1 + a \cos(\omega t + \phi)). \quad (5.3)$$

Often a term to compensate for accidental events arising from uncorrelated start and stop signals is added to this expression. This term is known as the background term and may or may not be time independent. The frequency  $\omega$  is proportional to the average field at the site of the muon. This field has a finite width due to the dipolar interaction in the material as mentioned in the section on dipolar interactions. This distribution of fields leads to a dephasing of the ensemble of muon spins which damps the  $\mu$ SR signal. In other words the probability for preferential decay along the muon spin decreases for the ensemble. This dephasing of the ensemble of muon spins is incorporated into the formula for fitting with a term known as

the relaxation function,  $G_X(t)$ . The formula describing the spectrum (Fig. 5.1) is now written

$$N(t) = N_0 \exp(-t/\tau_\mu) (1 + aG_X(t) \cos(\omega t + \phi)) + \text{Bkgd.} \quad (5.4)$$

For the case of static fields (no muon motion or host spin relaxation), the width of the field is usually approximated by a continuous and isotropic Gaussian distribution:<sup>7</sup>

$$P(B_X) = (2\pi M_2)^{-1/2} \exp(-(\gamma_\mu B_X)^2 / 2M_2) \quad (5.5)$$

where  $M_2$  is the second moment of the field distribution. The relaxation function may be found by a fourier transform of the field distribution. The relaxation function for Eqn. 5.5 is a Gaussian distribution.

$$G_X(t) = \exp(-\Delta_X^2 t^2 / 2) \quad ; \quad (\Delta_X^2 = M_2) \quad (5.6)$$

From this expression, one may obtain a line width  $\Delta$  which equals  $\Delta_X / \sqrt{2}$ . When the field distribution is not Gaussian, then  $G_X(t)$  will take on other forms. I will return to this later in this section. But first let us explore the development or calculation of  $M_2$ .

The second moment is proportional to the second derivative of  $G_X(t)$  at time  $t=0$ .

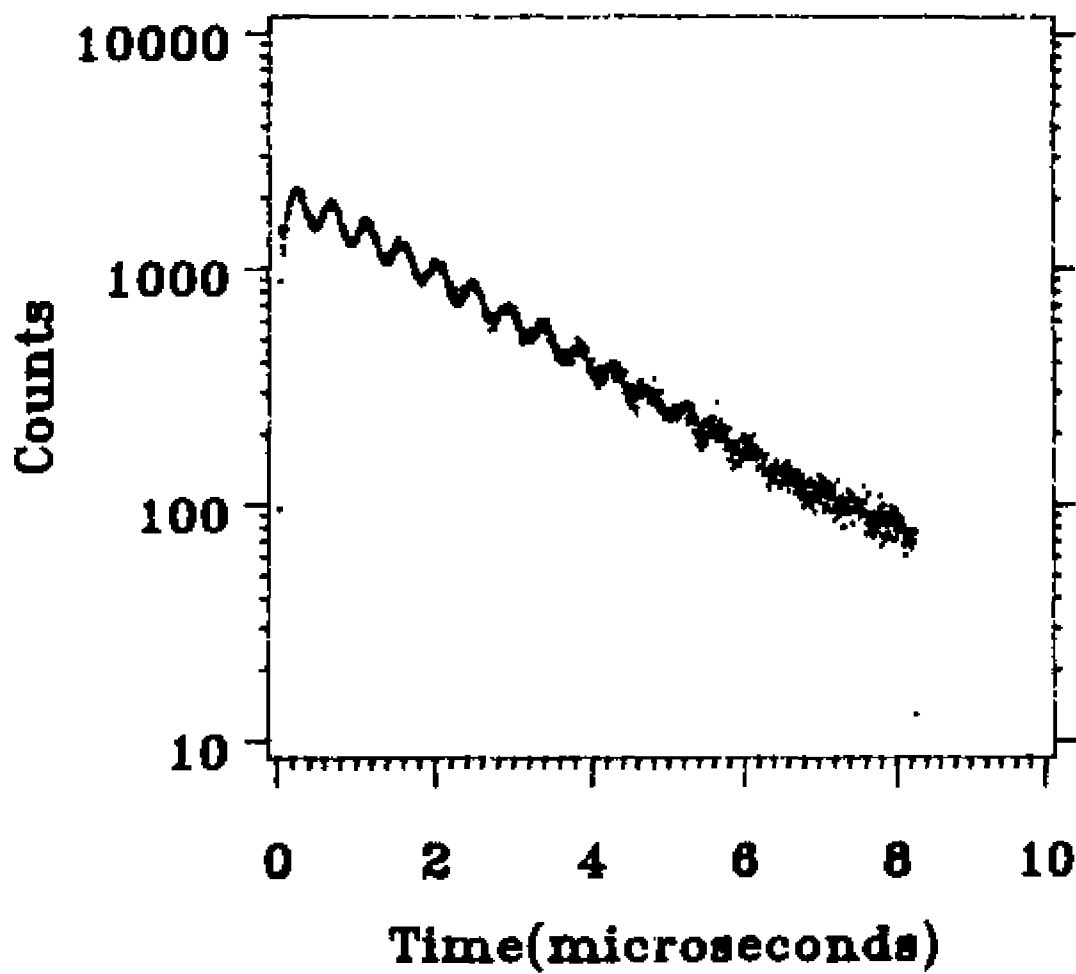


Figure 5.1  
A typical  $\mu$ SR transverse-field histogram (spectrum).

$$M_2 = - \left. \frac{d^2 G_X}{dt^2} \right|_{t=0} \quad (5.7)$$

The relaxation function is defined:

$$G_X(t) = \langle \sigma_X(t) \sigma_X(0) \rangle \quad (5.8)$$

where  $\sigma_X$  is the Pauli spin operator and the brackets refer to an average over all nuclear states. If we have an applied field in some direction with no quadrupole interaction, then this direction can be taken as the axis of quantization.  $G_X(t)$  can be rewritten as

$$G_X(t) = \langle \exp(iHt/\hbar) \sigma_X(0) \exp(-iHt/\hbar) \sigma_X(0) \rangle \quad (5.9)$$

$$\text{where } H = H_{\text{Zeeman}} + H_{\text{dd}}. \quad (5.10)$$

Since the trace possess cyclical invariance, the expression for the second moment is

$$M_2 = \langle [H, \sigma_X] [H, \sigma_X] \rangle / \hbar^2 \quad (5.11)$$

The approximate eigenstates of the system are those of the Zeeman Hamiltonian. The muon and proton operators commute leaving term A of Eqn. 3.27 (the secular Hamiltonian) as the only term in the Hamiltonian

$$H_{\text{dd}} = \sum_j \hbar^2 I_{\mu z} I_{Nz} (1 - 3 \cos^2 \theta) / r_j^3 \quad (5.12)$$



where the summation is over all nuclei. Upon calculating the commutators and taking the trace over the states, one obtains<sup>4</sup>

$$M_2 = \gamma_\mu^2 \gamma_N^2 \hbar^2 I_N(I_N+1)/3 [\sum_j (1 - 3\cos^2\theta_j)^2/r_j^6] \quad (5.13)$$

This is commonly known as the Van Vleck formula. For a polycrystalline sample, integration over all angles gives

$$M_2 = 4/15 \gamma_\mu^2 \gamma_N^2 \hbar^2 I_N(I_N+1) [\sum_j 1/r_j^6] \quad (5.14)$$

For nuclei with  $I > \frac{1}{2}$  and possessing a significant quadrupole moment,  $Q$ , a quadrupolar term must be added to the Hamiltonian. If the external field is not large enough to achieve the Zeeman limit, then the approximate energy eigenvalues for the system are

$$H_Q |I_N I_{Nz}\rangle = e^2 Q / [4 I_N (2 I_N - 1)] \{ I_{Nz}^2 - I_N(I_N + 1)/3 \} |I_N I_{Nz}\rangle \quad (5.15)$$

where  $I_N$  and  $I_{Nz}$  are quantum numbers for the nuclear spin. The quantization axis for the system is along the muon-to-nucleus vector. Since the eigenstates are different, then fewer terms in the dipolar Hamiltonian will average to zero. For the case of half-integer spin nuclei assuming a radially directed EFG from the muon, the second moment for a polycrystalline is written as<sup>25</sup>

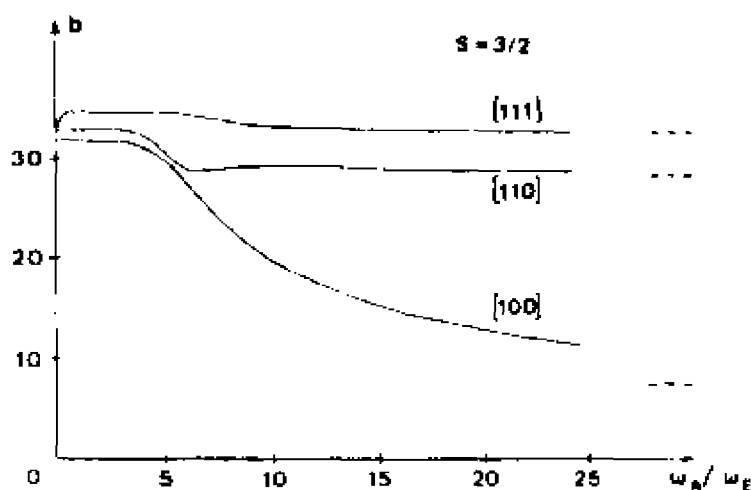


Figure 5.2 (Hartmann<sup>26</sup>)  
 Calculated line widths  $b$ , where  $b^2 = M_2 a^6 / \gamma_I^2 \hbar^2$ , for T sites in a FCC crystal as a function of the relative interaction strength  $\omega_B / \omega_E$  at  $a/2$  from the position of the interstitial for different orientations of the external magnetic field.  $\omega_B$  and  $\omega_E$  are the Larmor frequency of the lattice nuclei ( $\omega_B = \gamma_N B_0$ ) and the electric interaction frequency ( $\omega_E = (eQ_{\alpha\beta} / \hbar) \{V_{\alpha\beta} / [4s(2s-1)]\}$ ), respectively. The dashed lines to the right indicate the values for  $b$  in the Zeeman limit.

$$M_2 = 4/3 \gamma_\mu^2 \gamma_N^2 \hbar^2 I_N(I_N+1) [2/3 + 1/(4I_N(I_N+1))] (\sum_j 1/r_j^6). \quad (5.16)$$

For integer spin nuclei, the second moment under the same conditions is

$$M_2 = 8/9 \gamma_\mu^2 \gamma_N^2 \hbar^2 I_N(I_N+1) (\sum_j 1/r_j^6). \quad (5.17)$$

As the external magnetic field is increased, the value for the second moment will approach the value obtained from the Van Vleck formula. The magnetic field at which  $M_2$  changes indicates the strength of the quadrupolar coupling. This is depicted in Fig. 5.2 as the value of  $b$ , which is proportional to the muon line width, changes as a function of magnetic field.<sup>26</sup> The physics occurring is the change of quantization axis for the nearest-neighbor nuclei eigenstates.

Often, some particular form for  $G_X(t)$  is used to fit the data. This approach allows one to get an initial feel for the data. One particular form for  $G_X(t)$  is

$$G_X(t) = \exp(-\Lambda^2 t^2). \quad (5.18)$$

If the fields are static, then  $\Lambda^2$  is the second moment divided by two. However, the fields are not always static. This is caused by dynamic motion of the host spins or atoms or by the motion of the muon. When this occurs,  $\Lambda$

becomes smaller. This phenomenon is known as motional narrowing and will be explained by the following argument.<sup>10</sup> For the static case, the distribution of local fields is (r. l. for rigid lattice, no motion)

$$\delta h^{r.l.} \sim 1/(\gamma T_2^{r.l.}) \quad (5.19)$$

where  $T_2^{r.l.} = 2(M_2)^{-1}$ .  $T_2$  is a measure of time for the dephasing of an ensemble of spins and is known as the spin-spin relaxation time. If the muon is allowed to jump  $n$  times during the time  $T_2$ , then the dephasing will be much slower, because the dephasing in one site may be compensated by opposite dephasing in another site. Due to the random nature of the sites, one can use a one-dimensional random walk to describe this phenomenon. The dephasing after one jump is

$$|\delta\phi| = |\gamma\delta h^{r.l.}\tau| \quad (5.20)$$

where  $\tau$  is the field-correlation time.  $\tau$  is a measure of time for the dipolar field to decrease to  $1/e$  of its initial value. This decrease is due to diffusion of the muon, spin dynamics or diffusion of the host atoms (if the muon cannot move), or both. The distribution of dephasing  $|\Delta\phi|$  after  $n$  jumps at time  $t = n\tau$  is

$$\Delta\phi^2 = n(\delta\phi)^2 = t/\tau(\gamma\delta h^{r.l.}\tau)^2 = t\tau/(T_2^{r.l.})^2 \quad (5.21)$$

Dephasing is said to occur when  $\Delta\phi^2 \sim 1$  radian<sup>2</sup>, so that the effective time for dephasing  $t = T_2$  is given by

$$T_2 = [\tau (\gamma \delta h^{r.l.})^2]^{-1} = (T_2^{r.l.})^2 / \tau \gg T_2^{r.l.} \quad (5.22)$$

Upon taking the reciprocal of this equation, one obtains the effective distribution of the fields.

$$\delta h = \gamma \tau (\delta h^{r.l.})^2 \ll \delta h^{r.l.} \quad (5.23)$$

One sees that the effective distribution of fields is narrowed giving rise to a smaller value for the line width. This occurs only when the jump or correlation time  $\tau \leq T_2^{r.l.}$ . When  $\tau \ll T_2^{r.l.}$ , the relaxation function is better approximated by a Lorentzian form.

$$G_X(t) = \exp(-t/T_2) = \exp(-\Delta_X^2 \tau t) \quad (5.24)$$

In the range between the limits appropriate to Gaussian or Lorentzian relaxation functions, a third form for  $G_X(t)$  is often used. It is commonly called an Abragamian and is given by the following expression.<sup>7</sup>

$$G_X(t) = \exp(-\Delta_X^2 \tau^2 [\exp(-t/\tau) - 1 + t/\tau]) \quad (5.25)$$

The prerequisite for use of this form is that it goes to the proper limits. For  $\Delta\chi\tau \gg 1$ , Eqn. 5.25 reduces to the Gaussian form for  $G_X(t)$ . For  $\Delta\chi\tau \ll 1$ , Eqn. 5.25 reduces to the Lorentzian form for  $G_X(t)$ . In the region of  $\Delta\tau \geq 1$ , the uncertainty in  $\tau$  obtained from Eqn. 5.25 may be large. For this reason, zero- and low longitudinal-field  $\mu$ SR are commonly used to measure the field-correlation time. These two techniques will be discussed later.

The use of the Abragamian or Lorentzian forms allows one to obtain the correlation time as a function of temperature as is shown in Fig. 5.3.<sup>27</sup> Information concerning muon and/or host atom diffusion can now be determined. If the correlation time is due solely to muon diffusion, then  $\tau$  is proportional to  $1/\Gamma$  or  $1/D$  depending on the diffusion mechanism.

In this section, we have described the effects of dipolar coupling (with and without quadrupolar coupling) for the cases of a dynamic and static muon and/or host. These phenomena will be applied to the study of the hydride compounds in the chapter 7.

## 5.2 ZERO-FIELD TECHNIQUE

Zero-field  $\mu$ SR has proven to be a useful alternative technique. Its primary advantage is that it is very sensitive to motion of the muon and to dynamics of the host system (such as spin glasses). The technique and its benefits will be presented in this section.

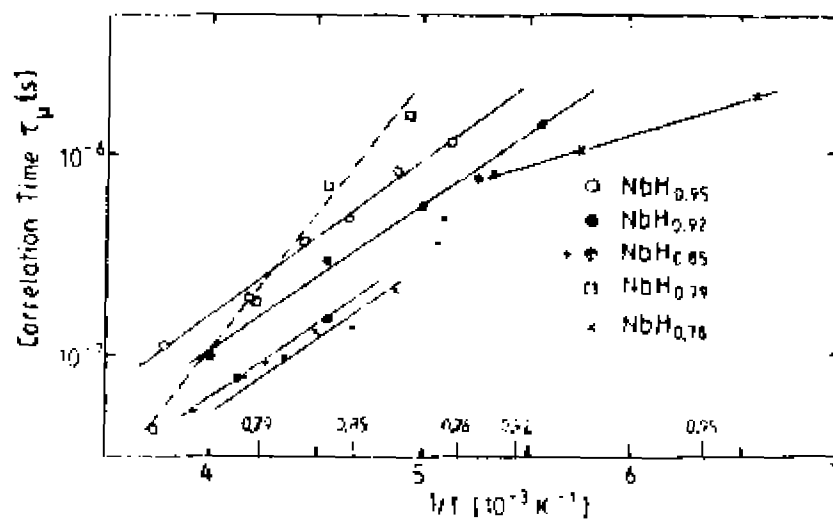


Figure 5.3 (Richter et al. 27)  
 Muon field-correlation time as a function of temperature and hydrogen concentration in  $\text{NbH}_x$ . The low temperature limits of the  $\beta$  phase for the different hydrogen concentrations are shown above the temperature scale.

For nonmagnetic materials in zero-field, the incoming muon's spin precesses around the internal dipolar fields. Since these fields have a finite width to them, the ensemble of muon spins will dephase. The time for dephasing is known as the zero-field spin-spin relaxation time and is inversely proportional to the width of the distribution of the fields. The data is described by the function

$$N(t) = N_0 \exp(-t/\tau_\mu) (1 + aG_z(t) \cos(\phi)) + \text{Bkgd} \quad (5.26)$$

which is the same as Eqn. 5.4 with  $\omega = 0$ . For the forward decay spectrum,  $\phi = 0$  for muons initially polarized along the beam momentum; while for the backward decay spectrum,  $\phi$  equals  $\pi$ . After determining  $N_0$ ,  $a$ , and  $\text{Bkgd}$  for both spectrums,  $G_z(t)$ , the zero-field relaxation function, is obtained with help of a computer.<sup>7</sup>

$$G_z(t) = [N'_F(t) - \alpha N'_B(t)] / [a_B N'_F(t) + a_F \alpha N'_B(t)] \quad (5.27)$$

where the subscripts and primes denote the two different spectra and the subtraction of the background from each spectrum, respectively. The quantity  $\alpha$  equals  $N_{0F}/N_{0B}$ , where  $N_{0F}$  and  $N_{0B}$  are the normalization constants in Eqn. 5.26 for the forward and backward spectra, respectively. This function depends on the correlation time and second moment for the muon. It is of a different form than  $G_x(t)$



in Eqns. 5.6, 5.24, and 5.25. The following discussion will show how an analytic form for  $G_z(t)$  is derived.

Consider the case of a muon surrounded by nuclei possessing static moments. If the angle between the initial muon spin polarization  $\vec{\sigma} = \sigma_z(0)\hat{k}$  and the dipolar field  $\vec{H}$  is  $\theta$ , then the time evolution of  $\sigma_z(t)$  is<sup>28</sup>

$$\sigma_z(t) = \cos^2\theta + \sin^2\theta \cos(\gamma_\mu H t). \quad (5.28)$$

If the random fields  $\vec{H}$  are assumed to be isotropic with each component possessing a Gaussian distribution function, then the field distribution is

$$P(H_i) = \gamma_\mu / [(2\pi)^{1/2} \Delta] \exp(-\gamma_\mu^2 H_i^2 / 2\Delta^2) \quad (i=x, y, z), \quad (5.29)$$

where  $\Delta^2/\gamma_\mu^2$  is the second moment for each distribution.

$$\Delta^2/\gamma_\mu^2 = \langle H_x^2 \rangle = \langle H_y^2 \rangle = \langle H_z^2 \rangle \quad (5.30)$$

To obtain the relaxation function  $G_z(t)$ , the statistical average of  $\sigma_z(t)$  is found.

$$G_z(t) = \iiint \sigma_z(t) P(H_x) P(H_y) P(H_z) dH_x dH_y dH_z \quad (5.31)$$

Hence, the relaxation function is

$$G_z(t) = 1/3 + 2/3(1 - \Delta^2 t^2) \exp(-\Delta^2 t^2 / 2) \quad (5.32)$$

The second moment for this relaxation function is  $2\Delta^2$ . The factor of two arises from the depolarization of the muon spin by fields in the x and y direction. In the transverse field case, the second moment is equal to  $\Delta^2$ , because only the component of the dipolar fields along the external field depolarizes the spin.

If no quadrupolar interaction is present, then one can use the method prescribed by Eqns. 5.7 and 5.8a to obtain the second moment. Since the muon and nuclear Zeeman levels are degenerate, all the terms of the dipolar Hamiltonian (Eqn. 3.27) are kept.<sup>4</sup> If  $\theta$  is the angle between the initial polarization and  $\vec{r}_i$ , then the second moment for a single crystal is

$$M_2^{ZF} = 1/3I(I+1)(\hbar\gamma_\mu\gamma_I)^2 \langle \sum_i (2 + 3 \sin^2\theta_i) / r_i^6 \rangle \quad (5.33)$$

For a polycrystalline sample,

$$M_2^{ZF} = 4/3I(I+1)(\hbar\gamma_\mu\gamma_I)^2 \langle \sum_i 1/r_i^6 \rangle \quad (5.34)$$

One advantage of zero-field  $\mu$ SR over transverse field is that the depolarization occurs at a higher rate. For the polycrystalline case,

$$\Delta_Z/\Delta_X = (5/2)^{1/2} \quad (5.35)$$

If a quadrupolar interaction is present, then the second moment is given by Eqns. 5.16 and 5.17 for half-

integer and integer spin nuclei, respectively. For the case of integer spin nuclei, the ratio of the depolarization rates is

$$\Delta_Z/\Delta_X = (5/3)^{1/2}. \quad (5.36)$$

where  $\Delta_X$  is the strong field (Zeeman limit) value.

As was mentioned at the beginning of this section, zero-field  $\mu$ SR is quite sensitive to the time fluctuations of magnetic fields. Kubo and Toyabe<sup>29</sup> have obtained curves of  $G_Z(t)$  for different values of  $r\Delta$  (Fig. 5.4b). For slow modulations of the field ( $r\Delta \sim 1$ ), this figure shows that zero-field  $\mu$ SR is much more sensitive to variations in  $r$  than the transverse-field technique (Fig. 5.4a).

In the past five years, the validity of Eqn. 5.32 has been questioned by Celio and Meier<sup>30</sup> and Petzinger and Wei.<sup>31</sup> The grounds for their arguments are the violation of three assumptions in Kubo-Toyabe theory.<sup>31</sup> The first is that the depolarizing field is static. This assumption is violated because the dipolar Hamiltonian which couples the muon and nuclei can alter the spin orientations of both. The second assumption is that the distribution of fields is a continuous Gaussian function as described by Eqn. 5.29. However, the depolarization is due only to those nuclei which are within a couple lattice distances, and will not produce a continuous Gaussian distribution. The third assumption is that the field distribution is isotro-

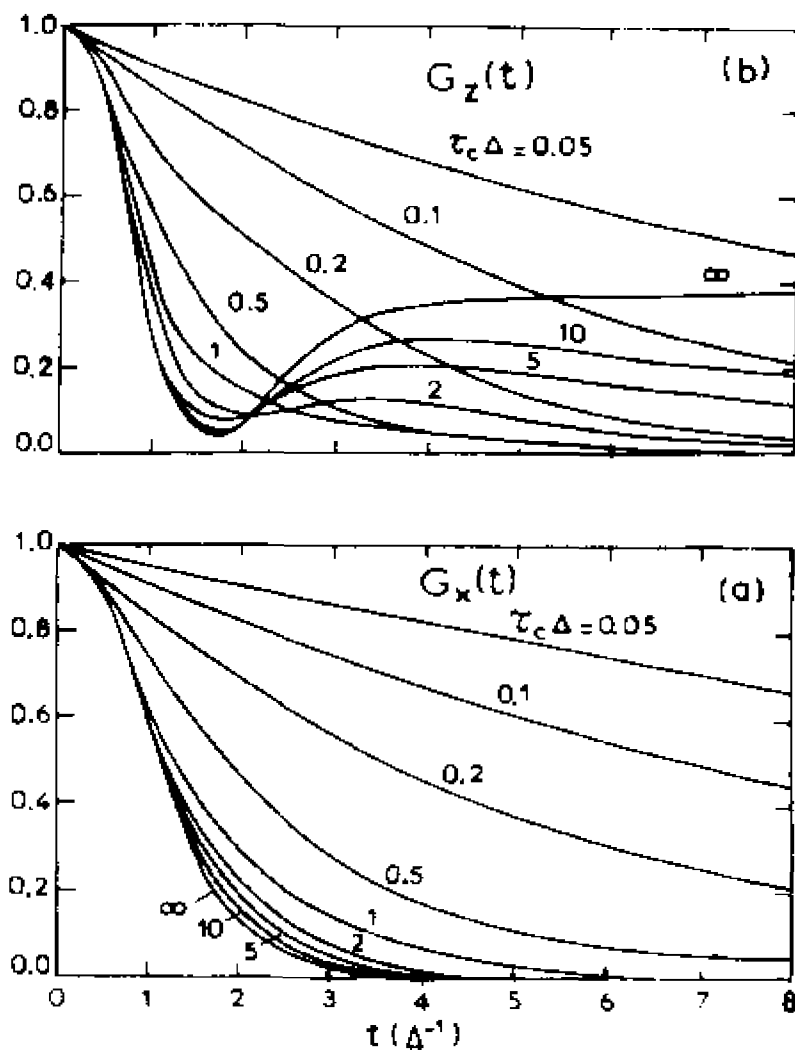


Figure 5.4 (Kubo and Toyabe<sup>29</sup>)  
 Calculated muon spin relaxation functions for different values of the field-correlation time,  $\tau$ . a.) High transverse-field relaxation function,  $G_x(t)$ . b.) Zero-field relaxation function,  $G_z(t)$ .

pic. While this is true for sites which possess cubic symmetry, the field distributions for a BCC T-site are non-isotropic. Celio and Meier<sup>30</sup> have calculated  $G_z(t)$  by the determination of eigenvalues and eigenstates of the dipolar Hamiltonian using Eqn. 5.37.

$$G_z(t) = \text{Tr}(\rho \exp[(i/\hbar)H_{dd}t] \sigma_\mu \exp[(-i/\hbar)H_{dd}t]) \quad (5.37)$$

where  $\rho$  is the spin density matrix.

$$\rho = 2(2I+1)^{-N} [1 + P_X(0) \sigma_X] \quad (5.38)$$

Fig. 5.5 compares the relaxation functions for a static muon in O and T sites of a FCC lattice for spin- $\frac{1}{2}$  nuclei. One drawback is that this calculation includes only the nearest-neighbor nuclei to the muon.

While the Kubo-Toyabe depolarization function can be used for data analysis, caution must be exercised in the interpretation of results so as not to mistake the oscillations of  $G_z(t)$  as an indication of motion.

### 5.3 LONGITUDINAL-FIELD TECHNIQUE

The zero-field technique is a special case ( $B=0$ ) of the longitudinal-field method. In this method, one begins with a small magnetic field along the axis of the initial muon spin. The experimental relaxation function is calculated using Eqn. 5.27. The field distribution for the x and y components is expressed by Eqn. 5.29. Due to the

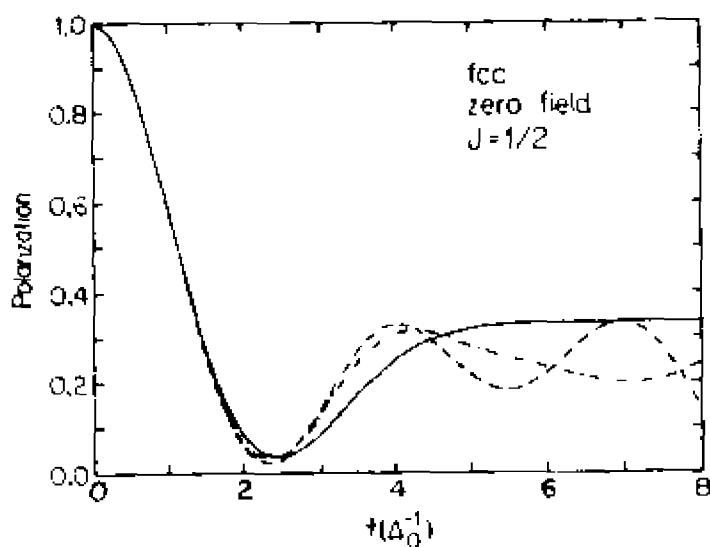


Figure 5.5 (Celio and Meier<sup>30</sup>)  
 Muon polarization in zero field as a function of time. The solid line corresponds to  $G_2(t)$  calculated using Kubo-Toyabe theory. The dashed-dotted (dashed) curve represents the calculated relaxation function using Eqn. 5.37 for a positive muon at an octahedral (a tetrahedral) site in a FCC lattice interacting with the nearest-neighbor nuclei possessing  $J=1/2$ .

presence of a longitudinal field, the z component for the field distribution must be changed to<sup>7</sup>

$$P(H_z) = \gamma_\mu / [(2\pi)^{1/2} \Delta_z] \exp(-\gamma_\mu^2 (H_z - H_0)^2 / 2\Delta_z^2) \quad (5.39)$$

These field distributions yield the following relaxation function where  $\omega = \gamma_\mu B_{\text{ext}}$ .

$$G_z(t) = 1 - 2\Delta_z^2/\omega^2 [1 - \exp(-\Delta_z^2 t^2/2) \cos(\omega t)] + \quad (5.40) \\ 2\Delta_z^4/\omega^3 \int_0^t \exp(-\Delta_z^2 r^2/2) \sin(\omega r) \, dr$$

For  $\omega=0$  ( $B=0$ ) Eqn. 5.40 reduces to Eqn. 5.32. Experimentally-determined relaxation functions along with fits to Eqn. 5.40 are shown in Fig. 5.6 for MnSi for various values of  $B_{\text{ext}}$ . This method allows one to experimentally determine the size of field necessary to decouple the nuclear dipole fields.

This technique is also useful in differentiating between static and dynamic fields (Fig. 5.7).<sup>7</sup> A small and static internal field can depolarize the muon in transverse field as efficiently as a rapidly fluctuating and large field. However, a small longitudinal field will appreciably affect the depolarization of the muon in a small and static internal field, but not in a rapidly fluctuating and large field. In the previous section, a word of caution was placed upon the interpretation of

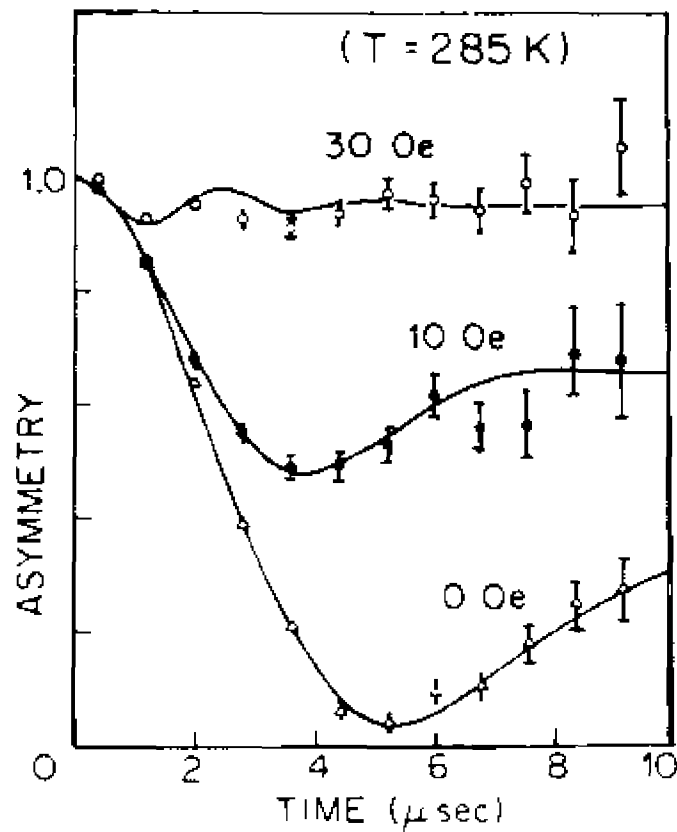


Figure 5.6 (Hayano et al. 28)  
 Field dependence of the  $\mu^+$  longitudinal-field relaxation functions in MnSi. The solid curves are fits to Eqn. 5.40.



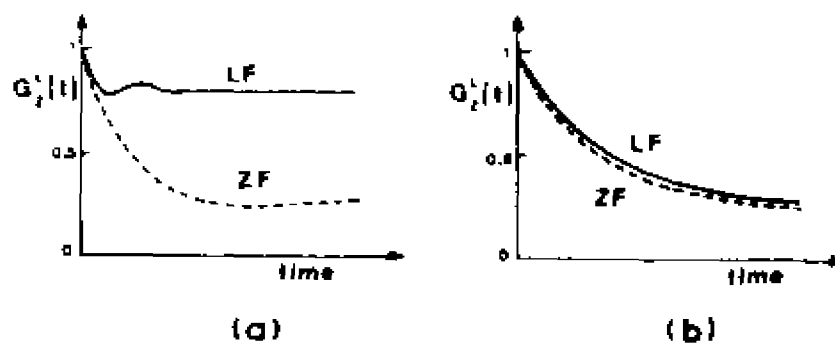


Figure 5.7 (Chappert<sup>7</sup>)  
 Comparison of longitudinal- and zero-field muon relaxation functions for a.) a static random field and b.) fast dynamic fields. The fast dynamic field limit is reached when the fluctuation rate  $\nu$  exceeds  $\omega_{\text{ext}}$  ( $\approx \gamma_{\mu} B_{\text{ext}}$ ).

$G_z(t)$ . The same holds for the longitudinal-field technique.

#### 5.4 SUMMARY

The use of different  $\mu$ SR techniques have been shown to be sensitive to effects due to magnetic interactions of the lattice and muon and to diffusion of the particle. Chapter 7 will describe the experiments on metal hydride systems where the magnetic and electronic interactions coupled with diffusion theory will be used to explain the results.

CHAPTER 6  
MONTE CARLO SIMULATIONS

A Monte Carlo simulation models a physical situation using a computer. The method is so named due to the use of random numbers similar to those coming out of roulette games.<sup>32</sup> Initially, one starts with a model for the physical system. The generated random numbers are used in one of three ways. The first method uses the numbers to define the initial set of conditions for the system. The system is then allowed to evolve under a rigid set of rules prescribed by the model. The second way begins with one set of initial conditions and lets the system evolve. In this instance, the random numbers are used to select the path of evolution with the weighting of each course prescribed by the model. A third method is a combination of the first two where the initial conditions and the path of evolution are chosen randomly using the weighted probabilities given by the model. All three methods yield numerically exact information within statistical errors. These errors may be reduced by increasing the amount of computer time. Since the last method averages over both initial conditions and evolution paths, the amount of computer time used may be large.

The Monte Carlo technique has several applications. The first use is that information obtained from the simulations can be compared to data from experiments to check the extent to which the model system correctly represents that real system. A second application is to check the validity of various approximations used in an analytical treatment. A third use is to procure information on systems where little or no experimental data exists. Thus, this method provides insight into models and motivates experiments on real systems.

This chapter will begin with a description of the process which is being modelled. This will be followed by a discussion of the application of the Monte Carlo method to this process. Finally, the results of the simulations will be presented.

## 6.1 THE MODEL

The initial motivation for the simulations arose from the appearance of small prefactors and small activation energies for the muon field-correlation times in metal hydride systems for temperature regions where the protons were diffusing.<sup>27,33,34</sup> It was observed that the muon attempt frequency was two or more orders of magnitude lower than that for the proton measured by NMR in the same systems.<sup>35</sup> Naively, this did not make any sense since the motion of the muon should be limited by proton diffusion.

For titanium dihydride, the hydrogen atoms occupy interstitial T sites which form a SC sublattice.<sup>36</sup> Bustard et al.<sup>36</sup> set out to determine whether the hydrogen atoms hop to first- or third-nearest-neighbor vacant T sites using NMR and Monte Carlo simulations. In their experiments, they measured the self-diffusion coefficient,  $D$ , for hydrogen using a stimulated echo pulsed-magnetic-field-gradient technique. Fig. 6.1 shows the sequence of rf pulses and magnetic field gradients used in the stimulated echo method. They have also determined the mean residence time between hop,  $\tau_d$ , from measurements of the spin-lattice relaxation time  $T_1$ . Since the existence of several analytic forms from different models relating  $\tau_d$  to  $T_1$  leads to ambiguity in the value of the residence time, they used the Monte Carlo method to calculate  $\tau_d(T_1)$  for first- and third-nearest-neighbor hopping. The two quantities  $\tau_d$  and  $D$ , are related by Eqn. 6.1.

$$D = fL^2/(6\tau_d) \quad (6.1)$$

The constant  $f$  is the tracer correlation factor which accounts for non-random backward jumps of a vacancy and is dependent upon the vacancy concentration. The second factor,  $L$  is the length of the jump. After using the Monte Carlo simulations to obtain  $\tau_d$  from  $T_1$ , they computed the limiting value of  $D$  using Eqn. 6.1 for first- and third-nearest-neighbor hopping. Fig. 6.2 shows the results of

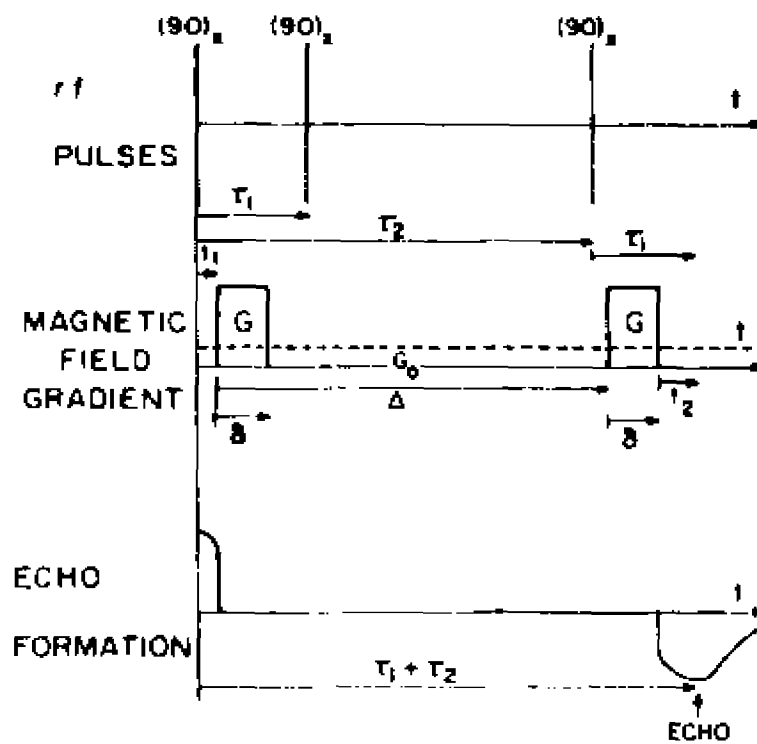


Figure 6.1 (Bustard et al.<sup>36</sup>)  
 The pulse sequence for the stimulated-echo method of measuring diffusion coefficients.

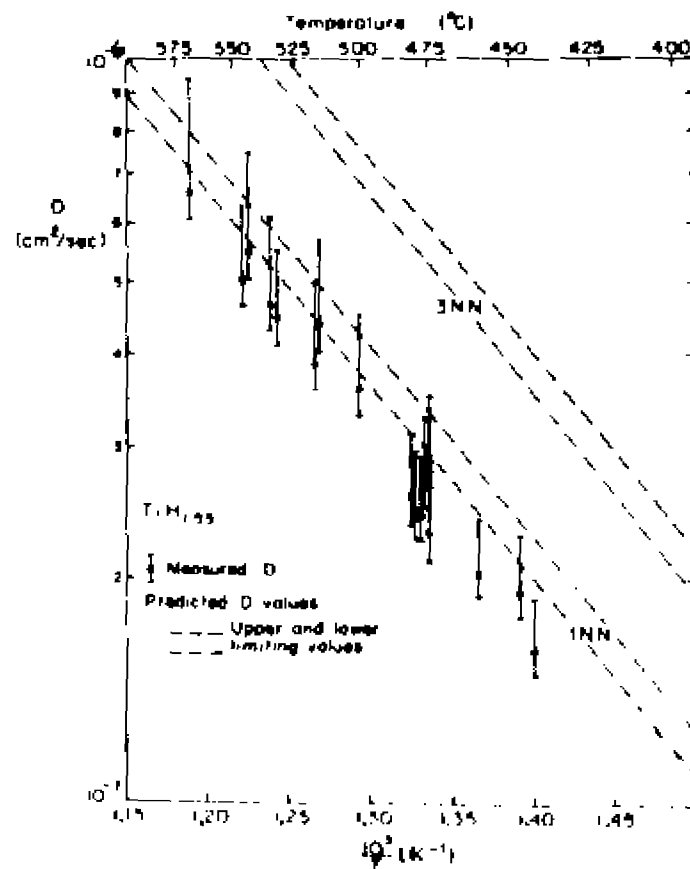


Figure 6.2 (Bustard et al.<sup>36</sup>)  
 Measured and predicted values of the diffusion coefficient  
 for  $TiH_{1.55}$  as a function of temperature.

their measurements of the diffusion constants along with the limiting values for  $D$ . The measurements coupled with their calculations show that the hopping is between first-nearest-neighbor sites. This would be expected from the calculations by Bisson and Wilson<sup>37</sup> of the activation energies in  $\gamma$ -TiH<sub>x</sub>. They found that the path with lowest activation energy (0.58 eV) was the one between first-nearest-neighbor positions. The activation energies for the second- and third-nearest-neighbor paths are 0.69 and 0.65 eV, respectively.<sup>37</sup> Therefore, these experiments and calculations show that hopping in  $\gamma$ -TiH<sub>x</sub> is between first-nearest-neighbor sites.

Since the path for motion of vacancies (hydrogen atoms) is known, a model with only a few parameters will be developed to describe the field-correlation time for the muon. The motion of the vacancies in the unperturbed lattice (no muon) occurs with some rate  $p$ . When the vacancy is next to the muon, the rate for the muon to move or the rate for the vacancy to move to the site of the muon is  $p'$ . This allows the muon jump rate to differ from the proton jump rate. Two other rates,  $p_{in}$  and  $p_{out}$ , have been added to account for the attraction or repulsion of vacancies due to the presence of the muon. These reflect a change in vacancy jump rate as the vacancy approaches the muon.  $p_{in}$  is the rate that a second-nearest-neighbor vacancy to the muon will become a nearest neighbor.  $p_{out}$



is the rate that a nearest-neighbor vacancy to the muon will become a second-nearest neighbor.

## 6.2 APPLICATION OF THE MONTE CARLO METHOD

The  $9 \times 9 \times 9$  lattice used for the simulations had periodic boundary conditions which allowed particles to diffuse from one edge to the opposite edge. Initially, the muon was placed at the center of the lattice with seven (~1%) vacancies randomly distributed. The random number generators utilized were the IMSL subroutine GGUBS and function routine GGUBFS. Both routines employed the same procedure to generate uniform deviates, but the subroutine GGUBS is able to generate more than one random number in each call. At the beginning of each simulation, the time of day was read in 1/300 second units. This integer number was converted to a real double precision value and used to seed the random number generator. The direction of the external magnetic field was picked randomly with respect to the coordinate system of the lattice. The spins on the remaining lattice locations (excluding the positions of the vacancies) were randomly given orientations randomly parallel and antiparallel to the field. After this was done, the dipolar magnetic field due to the protons in the lattice at the site of the muon was calculated. Having done this, the vacancies were allowed to move. During each time step, a random number for each vacancy was chosen. If the random number was less than the sum of the rates for

each of the six possible directions for motions, then the vacancy would be moved in the direction dictated by where the random number fell in the range of the sum of rates. For example, the six rates for a vacancy in one of the second-nearest-neighbor positions to the muon are:  $p$  for motion in the  $+x$  direction,  $p_{1n}$  for  $-x$ ,  $p$  for  $+y$ ,  $p_{1n}$  for  $-y$ ,  $p$  for  $+z$ , and  $p$  for  $-z$ . For the vacancy to move, the random number generated by the algorithm must be less than  $2p_{1n} + 4p$ . The range was divided into 6 intervals ordered  $(p_{1n} (-x), p_{1n} (-y), p (+x), p (+y), p (+z), p (-z))$ . The interval into which the random number falls determines the direction the vacancy will move. If  $p_{1n}$  and  $p$  equal  $1/5.1$  and  $1/51$ , respectively, and the random number chosen is  $0.314$ , then the vacancy will move in the  $-y$  direction for the above example. After each time step, the dipolar magnetic field at the site of the muon is computed. The total number of time steps was usually 3000 which was large enough to determine the field correlation time at the site of the muon, but small enough such that a vacancy was not likely to diffuse away and return full circle to the spot of the muon. Each simulation produced the dot product of the dipolar magnetic field as a function of time with a unit vector in the direction of the external field,  $\hat{B}_{ext}$ .

$$B(t) = \hat{B}_{dip}(t) \cdot \hat{B}_{ext} \quad (6.2)$$

The program used for the simulations is listed in Appendix A.

The results of each simulation were then multiplied by the dot product of the dipolar magnetic field at time  $t=0$  dotted with a unit vector in the direction of the external magnetic field ( $B(0) = \vec{B}_{dip}(0) \cdot \hat{B}_{ext}$ ).  $\langle B(t)B(0) \rangle$ , which is used to calculate  $G(t)$ , was obtained by averaging  $B(t)B(0)$  over all simulations with the same values for the four parameters:  $p$ ,  $p'$ ,  $P_{in}$ , and  $P_{out}$ .

$$G(t) = \exp[-\gamma^2 \int_0^t (t-t') \langle B(t')B(0) \rangle dt'] \quad (6.3)$$

A field-correlation time,  $\tau$ , is defined such that

$$\langle B(\tau)B(0) \rangle / \langle B(0)B(0) \rangle = 1/e.$$

A second significant quantity is the site occupation auto-correlation time. This number is a measure of the residence time for the particle at a particular site. The quantity was determined by summing  $N(t)\Delta t$  over the 3000 intervals.  $N(t)=1$  if the muon is at its initial starting point and 0 if not and  $\Delta t$  is the time increment.

In order to make the results independent of  $p$ ,  $\tau$  and  $\sum N(t)\Delta t$  were each multiplied by  $p$ .

### 6.3 RESULTS

The results of the simulations are shown in Table 6.1. The quantity  $\langle B(0)B(0) \rangle$  is proportional to the second moment for the muon.

$$M_2 = \gamma_\mu^2 \gamma_N^2 (\hbar / (2a^3))^2 \langle B(0)B(0) \rangle \quad (6.4)$$

The spin of the proton has been factored out of the bracket to make the results applicable in the future to other systems. From Eqns. 6.4 and 5.14,

$$M_2 = 4/15 \gamma_\mu^2 \gamma_N^2 \hbar^2 I_N(I_N+1) (\sum_j 1/r_j^6) \quad (5.14)$$

the theoretical value for  $\langle B(0)B(0) \rangle$  may be found. For a muon occupying a substitutional site in a SC lattice, the summation in Eqn. 5.14 is equal to  $8.402/a^6$ . Therefore, the theoretical value of  $\langle B(0)B(0) \rangle$  is 6.72. The values for  $\langle B(0)B(0) \rangle$  obtained with the simulations are in rough agreement and give confidence to the correctness of these simulations. A second test for the simulations is the case when  $p_{in}$ ,  $p_{out}$ , and  $p'$  equal  $p$ . If the probabilities are equal, then  $4p\tau c$  should be close to 1 for a SC lattice, where  $c$  is the vacancy concentration,  $\tau$  the field correlation time, and  $p$  the vacancy jump rate.<sup>38</sup> For this case, the simulations yield  $4p\tau c = 0.88$ , in good agreement.

The results in Table 6.1 have been ordered in terms of the parameter  $p\tau$ . In order to compare this to the results of the  $\mu$ SR experiments, one must calculate the product of the muon-field correlation time (obtained from a fit to an Abragamian form for the relaxation function (Eqn. 5.25) and the vacancy jump rate. The results of these simulations will be used in the following chapter.

TABLE 6.1  
Results of the Monte Carlo Simulations

<u>Simulation#</u>	<u>Probabilities</u>	<u><math>\langle B(0)B(0) \rangle</math></u>	<u><math>D_T</math></u>	<u><math>p \sum N(t) \Delta t</math></u>
01	$p' = p_{out} = p$ $p_{in} = 10p$	6.96	6	8
02	$p_{in} = p_{out} = p$ $p' = 10p$	6.22	12	13
03	$p' = p_{in} = p$ $p_{out} = p/100$	6.38	13	19
04	$p' = p_{in} = p_{out} = p$	6.97	23	34
05	$p' = p_{in} = p$ $p_{out} = 10p$	6.40	32	52
06	$p_{in} = p_{out} = p$ $p' = p/100$	6.94	49	160
07	$p_{in} = p_{out} = p$ $p' = 0$	6.56	52	infinite
08	$p_{out} = p$ $p_{in} = p/10$ $p' = 10p$	6.62	61	79
09	$p_{in} = p$ $p_{out} = p/100$ $p' = 0$	6.23	61	infinite
10	$p_{out} = p' = p$ $p_{in} = p/10$	6.68	98	121
11	$p_{out} = p' = p$ $p_{in} = p/100$	7.09	450	157
12	$p_{out} = p$ $p_{in} = p/100$ $p' = 0$	6.52	452	infinite

## CHAPTER 7

### RESULTS AND DISCUSSION

The interest in metal hydrides dates from the early 1950s. At that time, the interest was generated by the application of these compounds for use in control rods of nuclear reactors. Initially the studies were devoted to the determination of phases and lattice constants. Over the years the interest has changed to diffusion of the hydrogen atom in hopes of understanding the diffusion mechanism for hydrogen storage purposes. The present diffusion studies have focused primarily on FCC hydrides containing metals which have small nuclear moments.

Since the muon is a spin- $\frac{1}{2}$  particle with one unit of positive charge, it can be considered an isotope of hydrogen. For hydrides, the muon enters the sample as the "last hydrogen added," and competes for the same sites as the hydrogen atoms. Due to the muon's lower mass, one expects its motion to be impeded by the slower motion of the hydrogen atoms for near stoichiometric hydride compounds.

The results of transverse-, zero-, and low longitudinal-field studies of near-stoichiometric hydrides of titanium, zirconium, yttrium and lanthanum for static and

diffusing muons are reported below. The lattice structure for these FCC hydrides is shown in Fig. 7.1. The phase diagrams and lattice constants for these hydrogen alloys are presented in Figs. 7.2 - 7.5.

The lattice constants as a function of temperature for  $TiD_{1.98}$  and  $TiH_{1.99}$  are reported in Fig. 7.2b.<sup>40</sup>  $T_{critical}$  is the temperature for transition from the  $\delta$  phase to the  $\gamma$  phase. Table 7.1 shows that to within half a percent that the lattice constants for  $TiH_{1.99}$  are the same as for  $TiD_{1.98}$ .

Table 7.1

Lattice constants for titanium hydride as measured by x-ray diffraction.<sup>40</sup>

		$TiH_{1.99}$	$TiD_{1.98}$	ratio
$a$ (Å)	(T = 79 K)	4.528	4.516	1.0027
$c$ (Å)	(T = 79 K)	4.279	4.267	1.0028
$c/a$	(T = 79 K)	0.945	0.945	1.0000
$a$ (Å)	(T = 315 K)	4.454	4.440	1.0032
$T_{critical}$ (K)		$310 \pm 4$	$310 \pm 4$	

Fig. 7.2c shows the phase diagram for titanium hydride. The four crystalline forms for  $TiH_x$  are the hexagonal metal ( $\alpha$ ), BCC hydride ( $\beta$ ), FCC hydride ( $\gamma$ ), and FCT (Face-Centered Tetragonal) hydride ( $\delta$ ). The titanium hydride samples used in our study were of the  $\gamma$  and  $\delta$

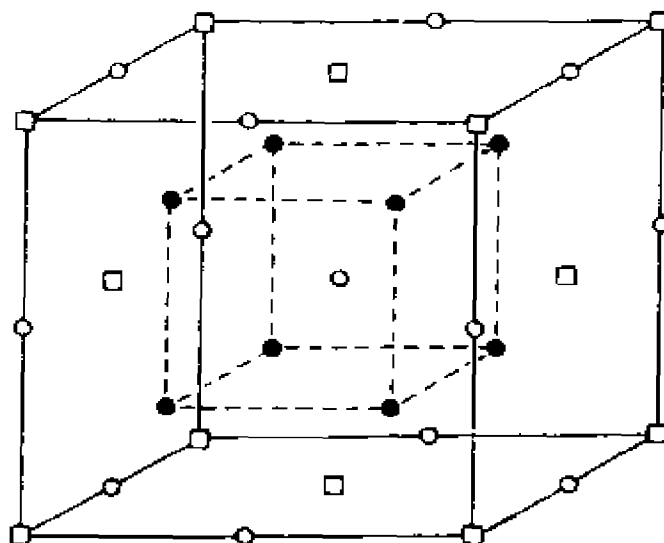


Figure 7.1 (Kossler et al.<sup>39</sup>)  
Lattice structure for FCC metal hydrides. The open squares, open circles, and closed circles correspond, respectively, to the metal atoms, octahedral sites, and tetrahedral sites (which are occupied by the hydrogen atoms).



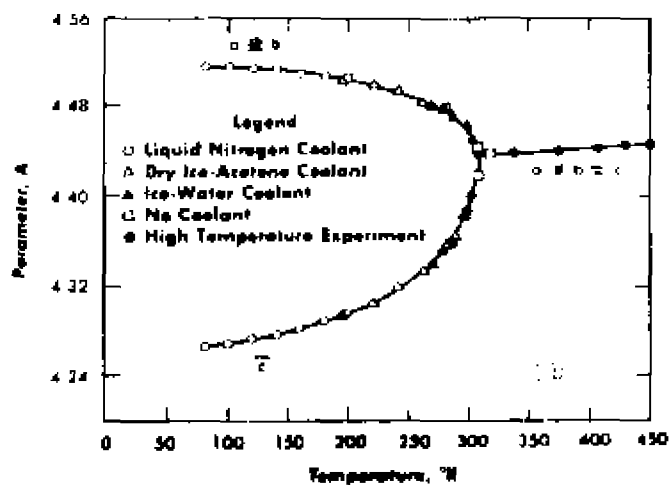
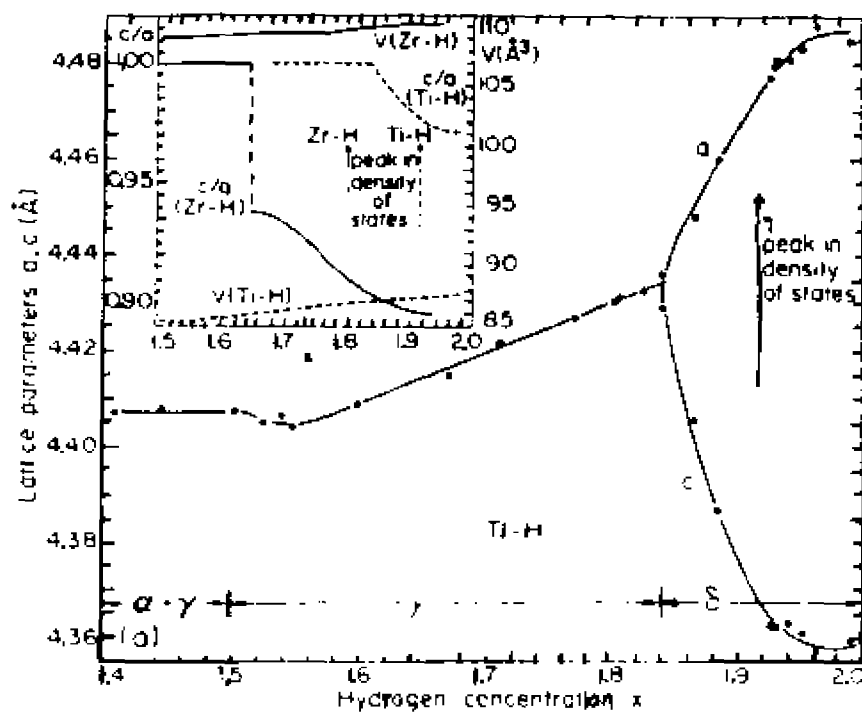


Figure 7.2a-b (Korn<sup>41</sup> and Yakel<sup>40</sup>)  
 a.) Lattice constant for titanium hydride as a function of hydrogen concentration at room temperature. b.) Lattice constant for  $TiD_{1.98}$  as a function of temperature.

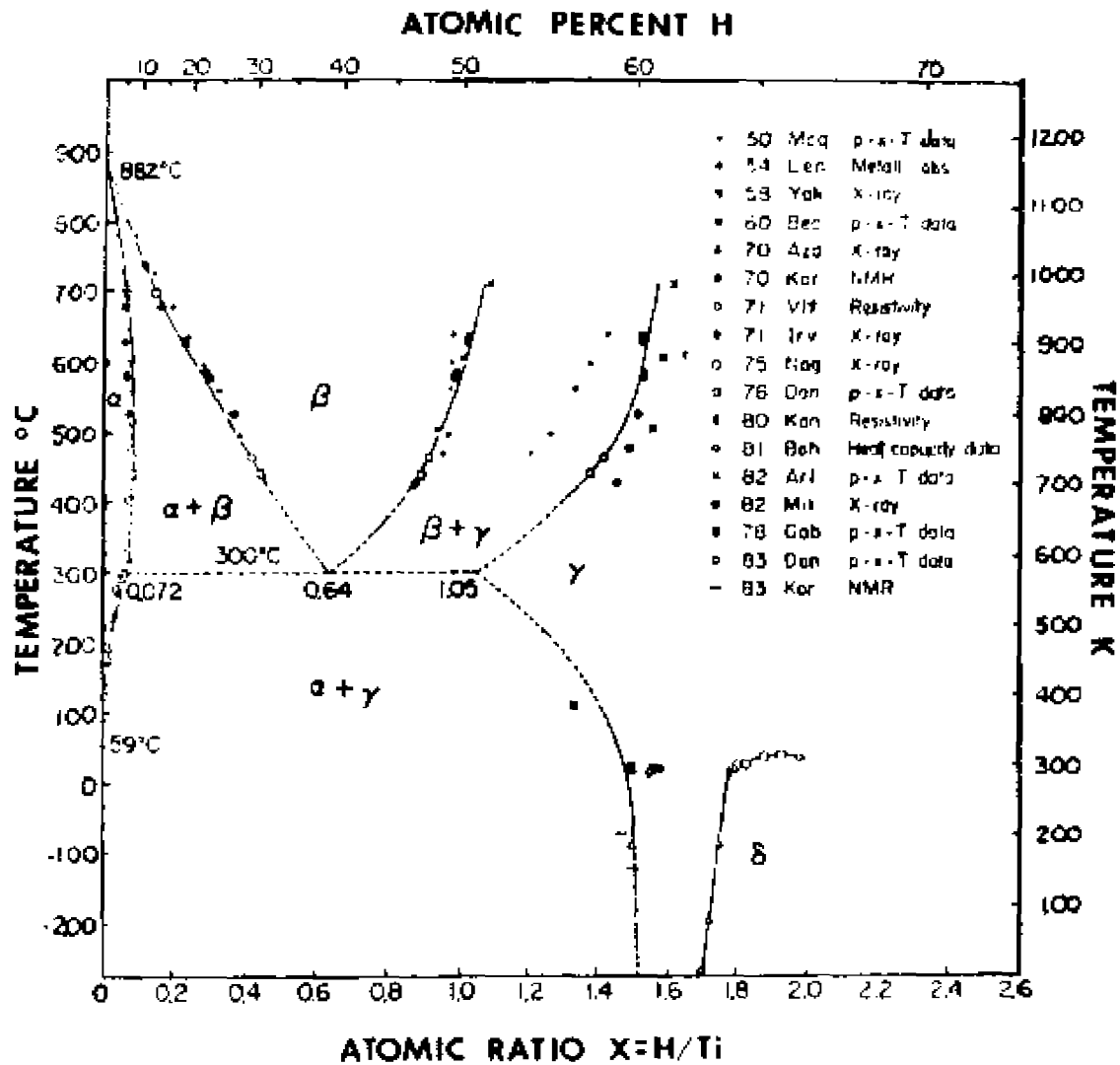


Figure 7.2c (San-Martin and Manchester<sup>42</sup>)  
 Phase diagram for titanium hydride. The dashed lines are  
 extrapolations of existing data.

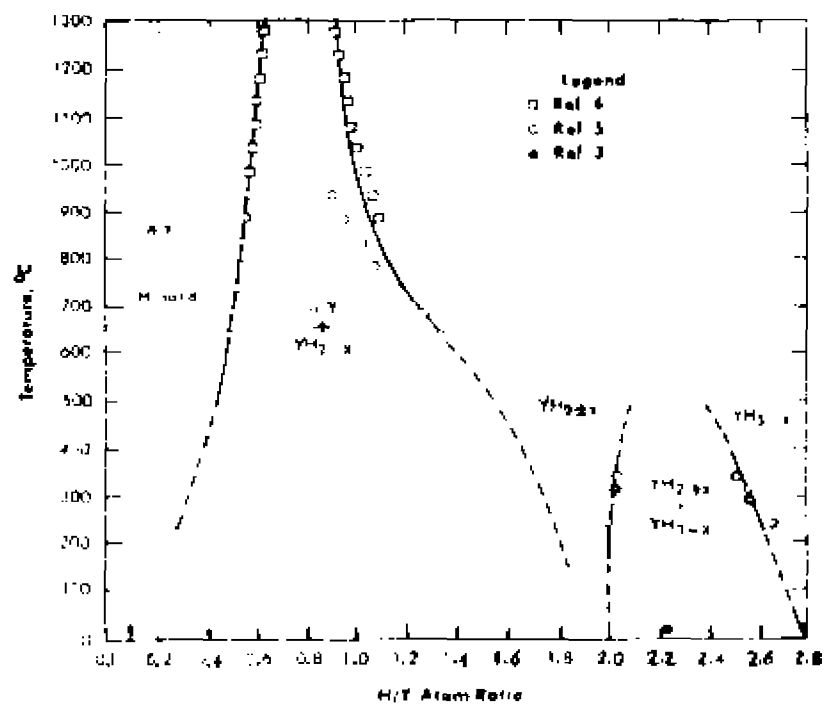


Figure 7.3 (Blackledge<sup>43</sup>)  
Phase diagram for yttrium hydride.

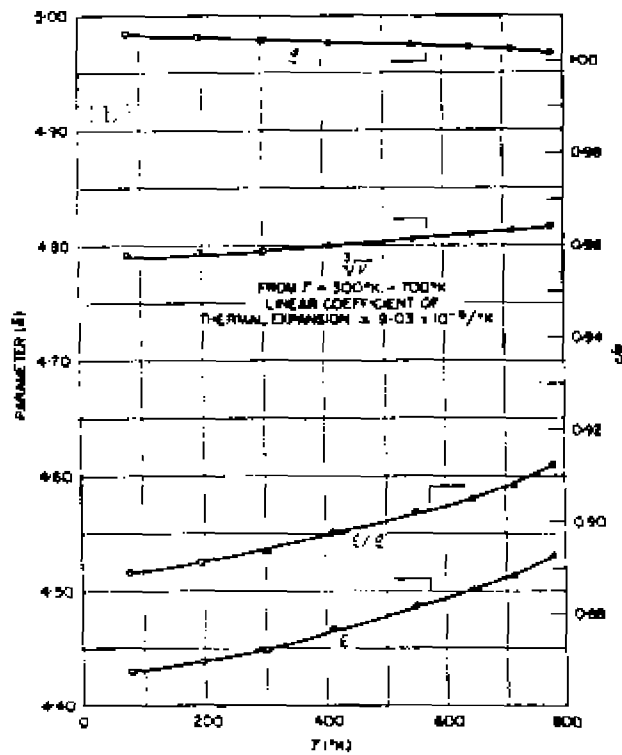
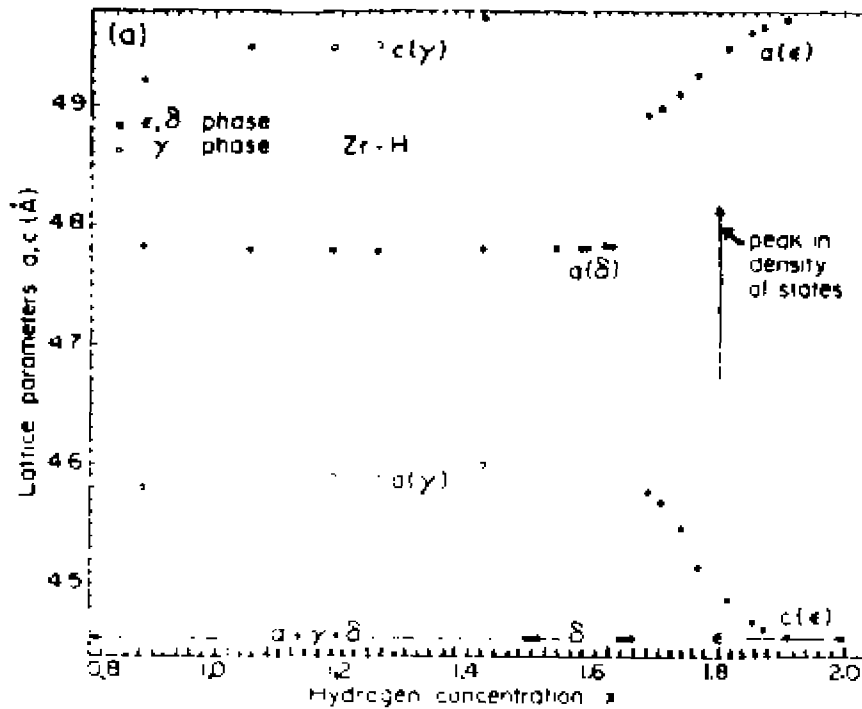


Figure 7.4a-b (Korn<sup>41</sup> and Yakel<sup>40</sup>)  
Lattice constant for a.) zirconium hydride as a function of hydrogen concentration at room temperature and b.)  $\text{ZrH}_{1.92}$  as a function of temperature.

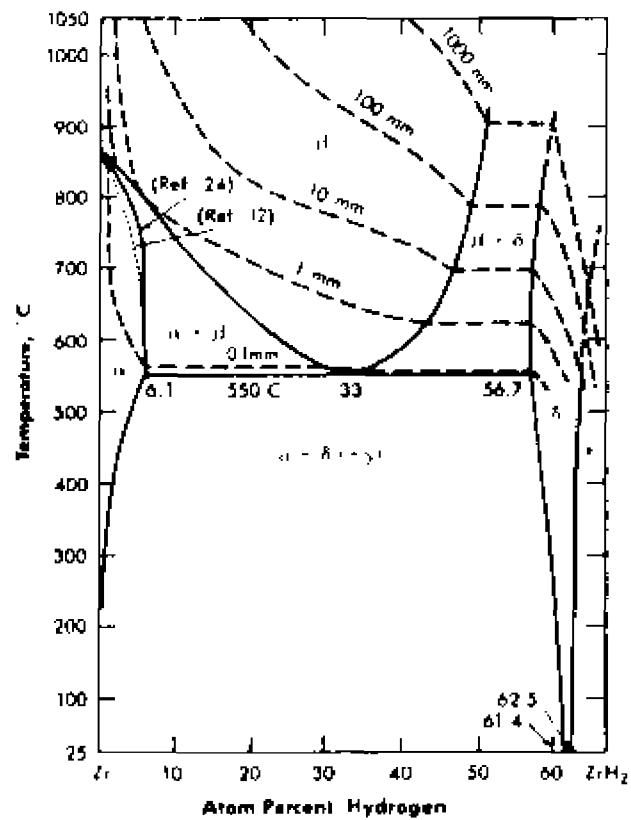


Figure 7.4c (Beck and Mueller<sup>44</sup>)  
 Phase diagram for zirconium hydride. Atom percent  
 hydrogen =  $x/(1+x)$ .

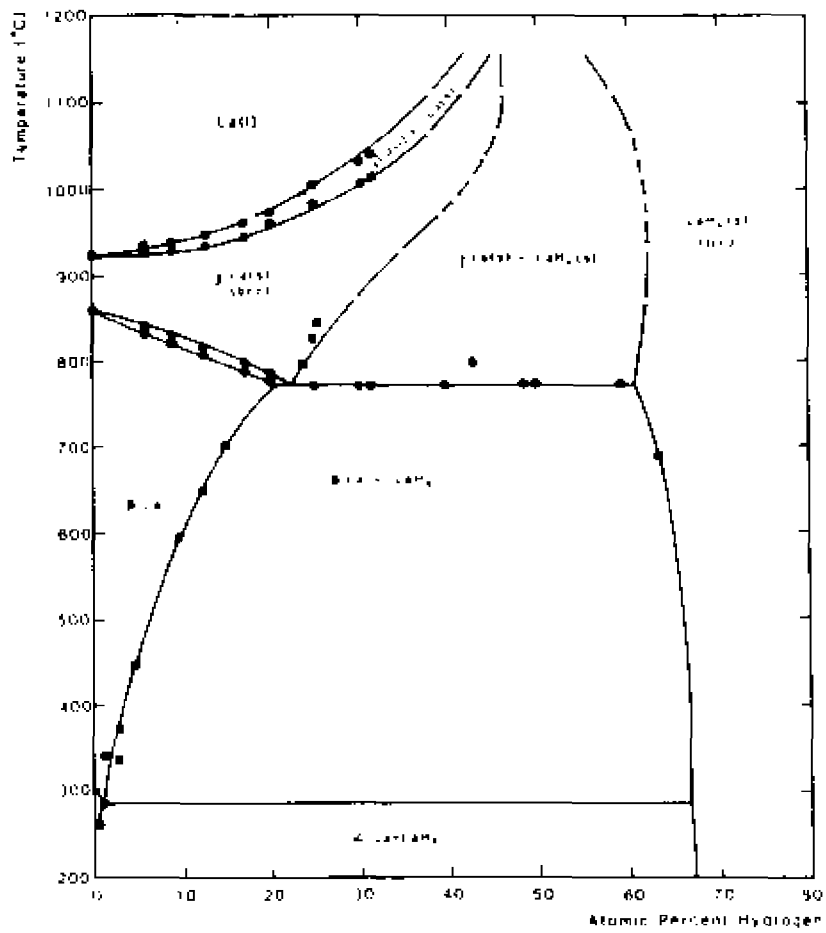


Figure 7.5a (Bishof et al.<sup>45</sup>)  
 Phase diagram for lanthanum hydride. Atomic percent  
 hydrogen =  $x/(1+x)$ .

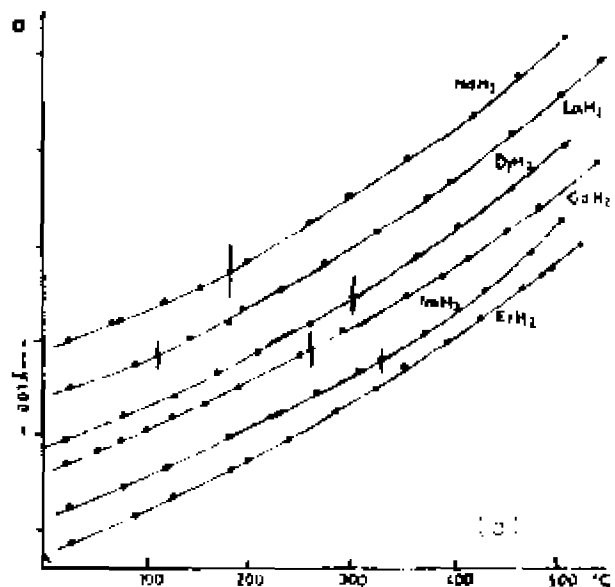
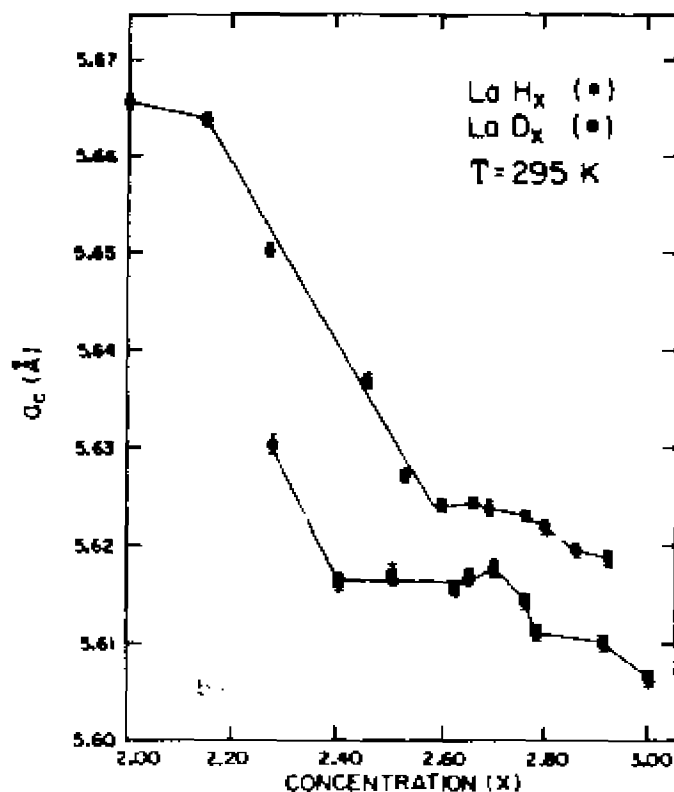


Figure 7.5b-c (Klavins et al.<sup>47</sup> and Bonnet and Daou<sup>48</sup>)  
 b.) Lattice parameter for lanthanum hydride as a function of hydrogen concentration at room temperature. c.) Lattice parameters for several rare earth dihydrides as a function of temperature. The curves can be parameterized by  $a(T) = a_0 + a_1T + a_2T^2$  where  $T$  is in  $^{\circ}\text{C}$  and  $a(T)$  in angstroms. For  $\text{LaH}_2$ ,  $a_0$ ,  $a_1$ , and  $a_2$  equal  $5.6689 \text{ \AA}$ ,  $3.400 \cdot 10^{-5} \text{ \AA}/^{\circ}\text{C}$ , and  $7.1 \cdot 10^{-9} \text{ \AA}/^{\circ}\text{C}^2$ , respectively. The units for the ordinate are arbitrary, since several of the curves were shifted parallel to the abscissa.

phases. The vacancies in the nonstoichiometric samples are randomly distributed in the hydrogen SC sublattice.

Fig. 7.3 shows the phase diagram for  $YH_x$ . The crystalline forms of  $YH_x$  are the hexagonal metal ( $\alpha$ ), FCC dihydride ( $YH_{2+x}$ ,  $\beta$ ), and hexagonal trihydride ( $YH_{3-x}$ ). The lattice constant for yttrium dihydride is 5.204 Å.<sup>43</sup> Our samples are in the  $\beta$  ( $YH_2$ ) and  $\alpha+\beta$  ( $YH_{1.77}$ ) phases. The hydrogen concentration in each phase in the  $YH_{1.77}$  sample can be estimated. The concentration of hydrogen in the  $\beta$  phase of the sample at a given temperature is roughly that for the  $\beta$  phase at the boundary between the  $\beta$  phase and  $\alpha+\beta$  phase regions for that temperature. The H/Y ratio of the  $\beta$  phase for  $YH_{1.77}$  at  $-100^\circ\text{C}$  is approximately 1.93. Similarly, the  $\alpha$ -phase hydrogen concentration at the same temperature is 0.04. This means that roughly 90% of the  $YH_{1.77}$  is composed of  $\beta$ -phase yttrium hydride. A majority of the hydrogen atoms are in T sites for the  $\beta$  phase, but the percentage of occupied O sites remains unresolved. This will be discussed in more detail in section 7.2.

For  $ZrH_x$ , the hydride consists of five distinct structures with several mixed phase regions as shown in Fig. 7.4c. The first phase has the hcp structure ( $\alpha$ ) of pure Zr. The second is of the high temperature BCC structure ( $\beta$ ). The third one appears in the mixed phase  $\alpha+\delta+\gamma$  and is a tetragonal structure ( $\gamma$ ) (Face-Centered Tetragonal (FCT)) with  $c/a > 1$ . The hydrogen occupy alternate



tetrahedral sites leading to a stoichiometric  $ZrH$ .<sup>44</sup> The  $\gamma$  structure is believed to be metastable. The fourth structure is FCC ( $\delta$ ) and has an average lattice constant of 4.78 Å over its concentration range at room temperature (Fig. 7.4a).<sup>41</sup> The fifth structure is FCT ( $\epsilon$ ) with  $c/a < 1$ . This phase is stable to very high temperatures, but the  $c/a$  ratio will not be constant due to the temperature dependence of  $c$ .<sup>40</sup> Both  $a$  and  $c$  are dependent on hydrogen concentration (Fig. 7.4a).<sup>41</sup> Our sample is of the  $\epsilon$  phase.

Lanthanum hydride has four primary structures: HCP ( $\alpha$ , pure metal), FCC ( $\beta$ , pure metal), BCC ( $\gamma$ , pure metal) and FCC hydride (Fig. 7.5a).<sup>45</sup> It has been found that hydrogen occupies T sites of the FCC hydride phase for  $H/La \leq 1.94$  by proton second moment measurements.<sup>46</sup> For concentrations greater than 1.94, the hydrogen atoms begin to occupy O sites. Fig. 7.5b shows that lattice parameter as a function of concentration and shows that  $a = 5.665$  Å for  $LaH_{2.06}$  at 295 K. The lattice parameter for  $LaH_2$  as a function of temperature is shown in Fig. 7.5c.

## 7.1 TRANSVERSE-FIELD STUDIES

The data from the transverse-field experiments were fit in two different manners. The first method used a non-linear least squares routine to minimize chi-square to Eqn. 5.4 using the form for  $G_X(t)$  specified in Eqn. 5.18 to fit each spectrum separately. This method assumes that  $\chi^2$  is a continuous function of  $n$  parameters which describe

a hypersurface in n-dimensional space. One problem in using this method is that the search range of the parameters must be close to the correct minimum in  $\chi^2$ . The second method used an algorithm which combined the method of linearizing the fitting function with a gradient search (Marquardt).<sup>49</sup> This method was employed to fit some of the data to Eqn. 5.4 with the form of  $G_x(t)$  as specified by Eqn. 5.25. The backward and forward spectra during this process were fitted simultaneously. This method allows for a crude search of the  $\chi^2$  hypersurface during the minimization of  $\chi^2$ . Both fitting algorithms were found to be in agreement when similar forms for Gaussian  $G_x(t)$  were used.

#### A. Titanium Hydride

The muon depolarization rate,  $\Lambda$ , for the titanium hydride samples is shown in Fig. 7.6. The plot can be divided into four different regions: I) a low temperature concentration-dependent plateau, II) a transition to a lower rate which occurs below room temperature, III) a concentration-independent plateau near room temperature, and IV) a region of motional narrowing due to diffusion of muons and/or hydrogen on the H sublattice (T sites).

The theoretical second moment for a static muon may be calculated by using the Van Vleck formula for a polycrystalline material (Eqn. 5.14, relabelled 7.1).

$$M_2 = (4/15) \gamma_\mu^2 \gamma_N^2 \hbar^2 I_N(I_N+1) \left( \sum_j 1/r_j^6 \right) \quad (7.1)$$

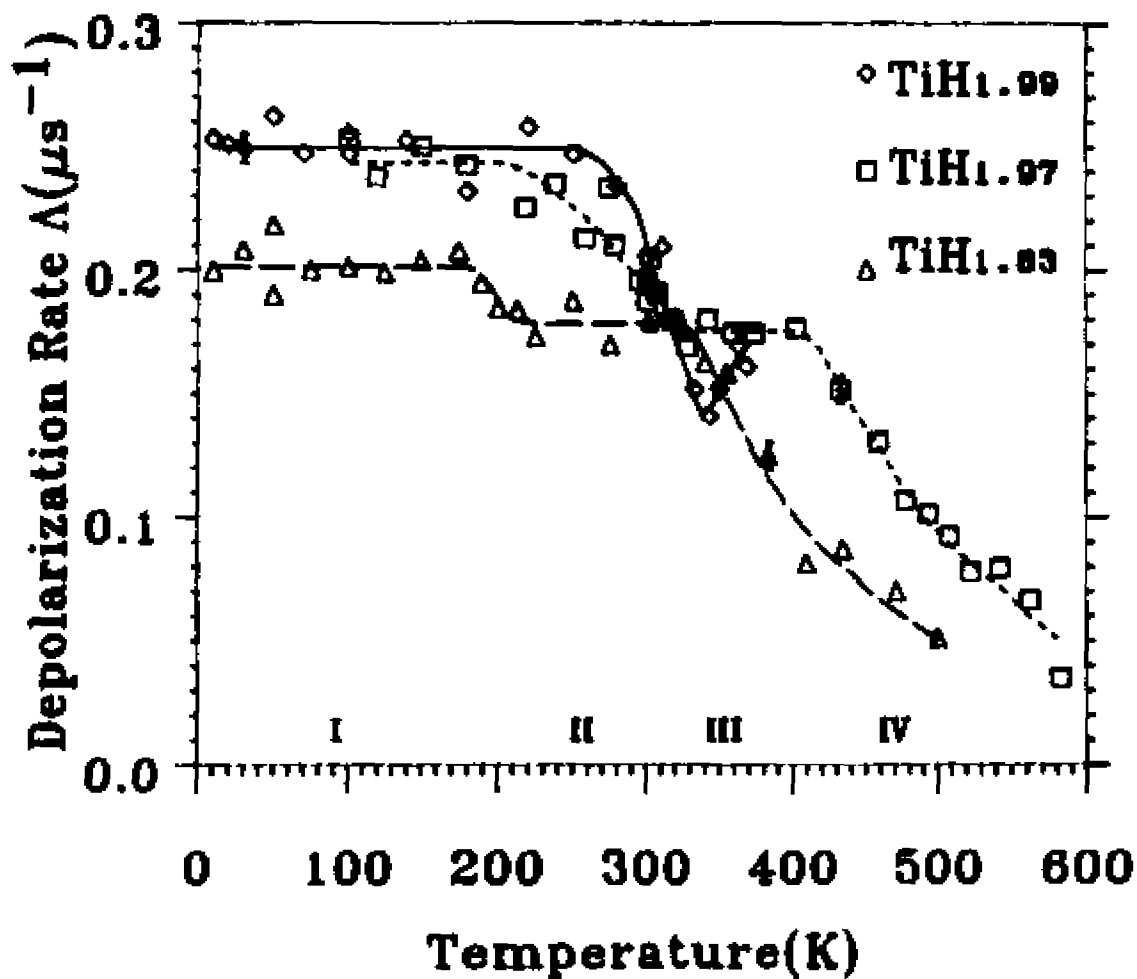


Figure 7.6 (Kossler et al.<sup>34</sup>)  
 Muon depolarization rate,  $\Lambda$ , as a function of temperature for the three samples of  $\text{TiH}_x$  studied. The lines serve as a guide for the eye.

If the line shape is Gaussian, then the measured second moment is

$$M_2 = 2\Lambda^2 \quad (7.2)$$

Since the gyromagnetic ratio (which is proportional to the magnetic moment) for titanium is very small, only the contribution from the hydrogen nuclei will be considered ( $\gamma_H = 2.675 \times 10^4 \text{ s}^{-1}\text{G}^{-1}$ ,  $\gamma_\mu = 8.51 \times 10^4 \text{ s}^{-1}\text{G}^{-1}$ ).<sup>12</sup> In the calculation of  $\Lambda$  for both O and T sites, the effect of the mutual spin-flips of the protons must be included. This has the effect of reducing the fourth moment of the  $\mu\text{SR}$  signal by 22% which lowers the line width of a fitted Gaussian by approximately 5% (Appendix B). The variance of  $c/a$  and  $a$  for the two phases ( $\gamma$  and  $\delta$ ) was neglected in this calculation since i) the volume is roughly a constant and ii) the computer calculations for a few test cases produced differences in  $\Lambda$  of less than a percent. Assuming a  $\gamma$ -phase lattice with  $a=4.454 \text{ \AA}$ , no vacancies, and mutual spin-flips of the protons, the depolarization rates are  $0.298 \text{ } \mu\text{s}^{-1}$  for octahedral site occupancy ( $\Lambda_{\text{OCT}}$ ) and  $0.189 \text{ } \mu\text{s}^{-1}$  for tetrahedral site occupancy ( $\Lambda_{\text{TET}}$ ). These values will serve as a guide for determination of site occupation by the muon as a function of temperature.

### 1. Region I

The constant depolarization rate in Fig. 7.6 for each sample indicates that the muon is stationary at low temperatures. The hydrogen concentration dependence of the average  $\Lambda$  is reflected by the  $x=1.99$  sample having the highest value for the depolarization rate and the  $x=1.83$  sample the lowest. This observation can be interpreted to indicate that the sites occupied by the muon are a mixture of O and T sites. The change of  $\Lambda$  with concentration can then be explained by the probability for T site occupancy increasing as the hydrogen content decreases. The depolarization rate dependence on O and T site occupancy can be made explicit by

$$\Lambda_{\text{EXP}}^2 = \Lambda_{\text{TET}}^2 P + \Lambda_{\text{OCT}}^2 (1-P), \quad (7.3)$$

where  $P$  is the probability of tetrahedral occupation.  $\Lambda_{\text{EXP}}$  is the observed muon line width; while  $\Lambda_{\text{OCT}}$  and  $\Lambda_{\text{TET}}$  are the line widths for O and T site occupancy by the muon. If one assumes that muons stop in O sites initially and that those that have a vacant nearest-neighbor T site transfer in a short time into the vacancy, then the probability for a muon to occupy a T site is

$$P = 8(1-x/2). \quad (7.4)$$

$\Lambda_{\text{EXP}}^2$  is plotted as a function of  $(1-x/2)$  in Fig. 7.7. The line is a least squares fit to Eqn. 7.3 with  $\Lambda_{\text{OCT}}$  and  $\Lambda_{\text{TET}}$  as the free parameters. The values determined from this fit are  $\Lambda_{\text{OCT}} = 0.252(3) \mu\text{s}^{-1}$  and  $\Lambda_{\text{TET}} = 0.172(5) \mu\text{s}^{-1}$ . This  $\Lambda_{\text{TET}}$  will be discussed in section 7.1A.3. This value for  $\Lambda_{\text{OCT}}$  is much lower than that calculated from the Van Vleck formula leading one to postulate a local lattice expansion around the muon. This is not surprising since the muon often causes a local lattice dilation as was mentioned for copper in section 3.3C. The calculated local lattice expansion is approximately 6(1)%. Alternatively, one can say that each nearest-neighbor hydrogen is displaced 0.13 Å outward. This distortion presumably arises from the shortness of the distance between O and T sites in an undistorted lattice ( $\sqrt{3}/2$  times the tetrahedral-tetrahedral site spacing), and the fact that the muon's spatial wavefunction is much larger than that of a hydrogen atom.

## 2. Region II

Fig. 7.6 shows a region of transition for each sample in the vicinity of room temperature. This region occurs at different temperatures for each sample. For  $x=1.83$ , the muon stops in a tetrahedral site approximately 70% of the time in region I. This leaves 30% of the muons to find T sites in region II. This change in the depolarization rate occurs at low temperatures where vacancy and muon motion

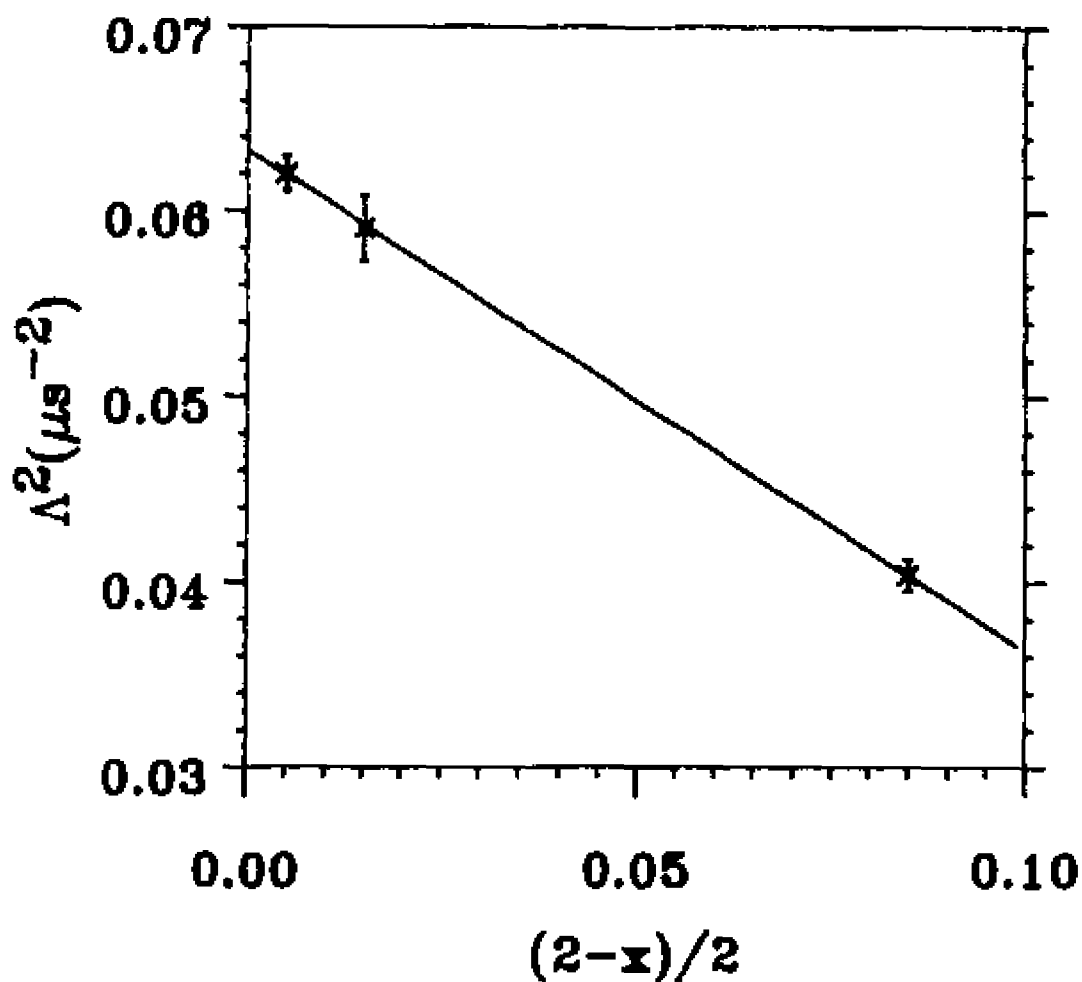


Figure 7.7 (Kossler et al.<sup>34</sup>)  
The depolarization parameter,  $\Delta_{\text{EXP}}^2$ , in region I for each titanium hydride sample plotted as a function of vacancy concentration. The line is a least squares fit to Eqn. 7.3.

is limited and can be explained by the presence of an attractive force between the muons and vacancies. For  $x=1.83$ , the number of vacancies among nearest-neighbor and second-nearest-neighbor sites is 2-3. Therefore, if there is no nearest-neighbor vacancy, then there may be 2-3 vacancies which only have to make one jump to be a nearest neighbor. Since there is a distortion of the local hydrogen sublattice lattice present for a muon in an octahedral site, this means that energy is being expended to "push" on the nearest-neighbor hydrogens. The system, therefore, finds it energetically favorable to allow the hydrogen to swap places with the vacancy. With a vacancy as a nearest neighbor, the muon will move into this T site.

For  $x=1.99$ , there are only 1 in 200 T sites available for occupancy. When the muon begins to move, the value of  $\Lambda$  drops below  $\Lambda_{TET}$  (Fig. 7.6) due to averaging over several octahedral sites (motional narrowing). In other words, the probability for a muon to find a vacant T site is small for temperatures less than 350 K. As the temperature increases above 350 K, the time to find a vacant T site decreases. This is evident in the recovery of the depolarization rate.

Quantitatively, one can calculate a mean time of stay,  $\tau_B$ , for a muon at an octahedral site. Since there is a small percentage of muons initially in T sites for temperatures below the motional narrowing region, the



field-correlation time,  $\tau$ , will not be equal to  $\tau_g$ . However, the field-correlation time, obtained from an Abragamian form for the relaxation function, can be used to obtain  $\tau_g$  via the parameter  $\alpha$  (defined in Appendix C). For an Abragamian form of the relaxation function (Appendix C),<sup>50</sup>

$$\alpha = \Delta^2 \tau_\mu^2 / (\tau + \tau_\mu) \quad (7.5)$$

where  $\tau_\mu$  is the mean lifetime of a muon, 2.197  $\mu\text{s}$  and  $\Delta^2$  is the muon second moment used in the Abragamian form for the relaxation function,  $1.24 \times 10^{-3} \mu\text{s}^{-2}$ . If one assumes that there are two possible trapping sites, octahedral and tetrahedral, and that the probability of being in a T site initially is given by Eqn. 7.4

$$P = 8(1-x/2) \quad (7.4)$$

If the trapping radius into a T site includes only nearest-neighbor T sites, then the effective vacancy concentration,  $c'$ , equals  $P$ . An expression for  $\tau_g$  can be derived in terms of  $\alpha$  (Appendix C).<sup>50</sup>

$$\begin{aligned} \tau_B = c' r_\mu & \left[ -0.5(1 + c' + (1 - c') \Delta_{\text{TET}}^2 r_\mu^2 / (\alpha - \Delta_{\text{TET}}^2 r_\mu^2)) \right. & (7.6) \\ & \left. \pm [0.25 \times \{ (1 - c') \alpha / (\alpha - \Delta_{\text{TET}}^2 r_\mu^2) \}^2 + \right. \\ & \left. (1 - c') c' \Delta_{\text{OCT}}^2 r_\mu^2 / (\alpha - \Delta_{\text{TET}}^2 r_\mu^2) \}^{1/2}]^{-1} \end{aligned}$$

$\Delta_{\text{TET}}^2$  and  $\Delta_{\text{OCT}}^2$  are the second moments for a muon in a tetrahedral and octahedral site, respectively, and can be calculated using the line widths obtained in the previous section.

$$\Delta_{\text{OCT}}^2 = 2\Lambda_{\text{OCT}}^2 \quad ; \quad \Delta_{\text{TET}}^2 = 2\Lambda_{\text{TET}}^2 \quad (7.7)$$

The values for  $c'$ ,  $\Delta_{\text{TET}}^2$ , and  $\Delta_{\text{OCT}}^2$  are 0.04(8), 0.059(3)  $\mu\text{s}^{-2}$ , and 0.127(3)  $\mu\text{s}^{-2}$ , respectively. Since the expression for  $\tau_B$  (Eqn. 7.6) is of the form of a quadratic formula, there will be two values for the time of stay except when the term raised to the one-half power is zero which occurs at the minimum value of  $\alpha$ . As a check of the effective vacancy concentration,  $c'$  can be calculated by using the values given previously for  $\Delta_{\text{TET}}$ ,  $\Delta_{\text{OCT}}$  and  $r_\mu$ . The value obtained for the effective vacancy concentration is 0.12(5) which agrees with the other value for  $c'$  (0.04(8)). Using this calculated value of  $c'$  and the values for  $\alpha$  obtained from Eqn. 7.5,  $\tau_B$  may be calculated as a function of temperature and is shown in Fig. 7.8. The line is a fit to Eqn. 7.8 with the parameters  $r_0$  and  $E_a$  equal to  $10^{-13}(1)\text{s}$  and 0.48(8) eV, respectively.

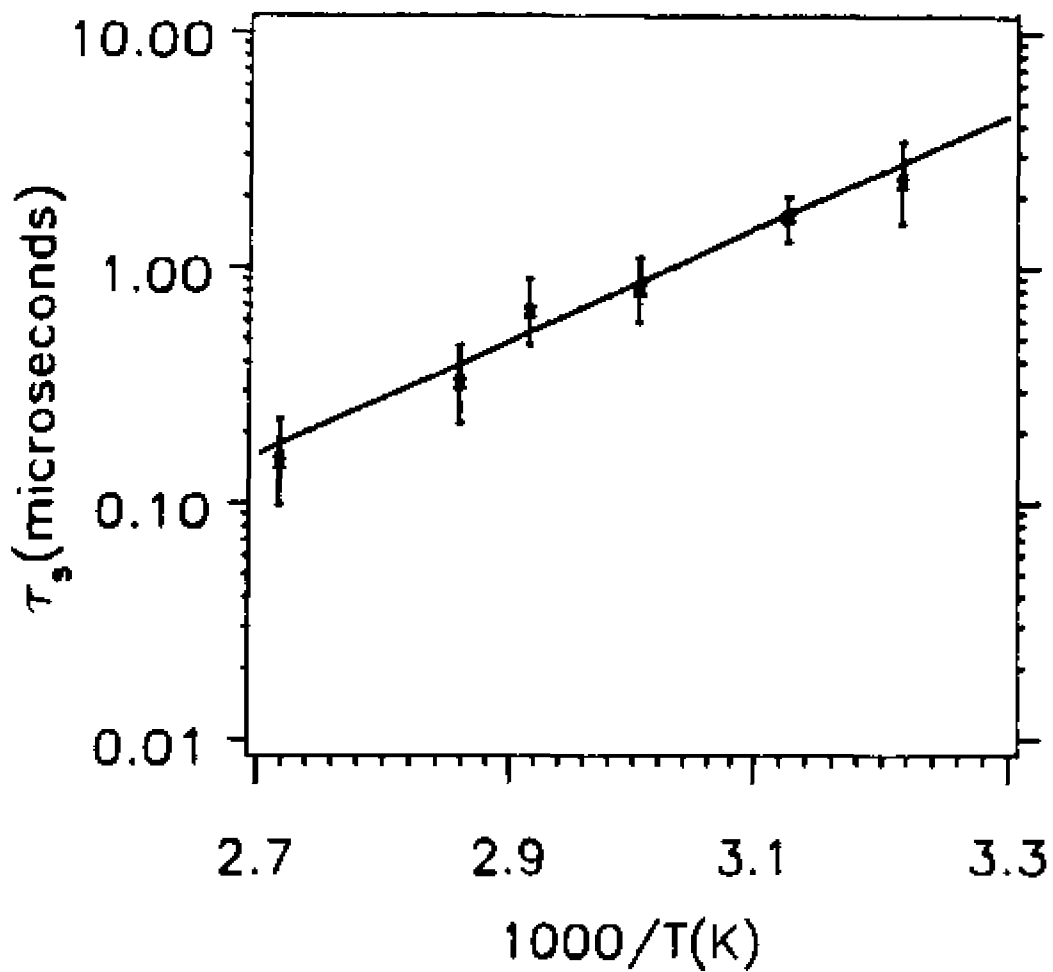


Figure 7.8 The mean time of stay for a muon at an octahedral site,  $\tau_s$ , plotted as a function of temperature. The line is a least squares fit to Eqn. 7.8.

$$r_s = r_0 \exp(E_a/kT) \quad (7.8)$$

The activation energy,  $E_a$ , is the energy necessary for the muon to activate out of an octahedral site. This is smaller than the activation energy for a proton in a T site, 0.507(10) eV.<sup>21</sup> For titanium hydride, the hydrogen vibration frequency is  $3.3 \times 10^{13} \text{s}^{-1}$ .<sup>21</sup> From the value for  $r_0$ , one can see that the muon attempt frequency ( $1/r_0$ ) is of the same order of magnitude implying that the vibration of the hydrogen lattice is the mechanism responsible for the activation of the muon out of an O site.

The model presented above will always yield a dip (or a minimum) in the depolarization rate,  $\Lambda$  (or in the alpha parameter). However, the depolarization rate,  $\Lambda$ , as a function of temperature for  $x=1.97$  does not have a minimum implying the effective vacancy concentration is too high for this model to be valid. One can however say that the majority of the muons are trapped in O sites until near room temperature and are able to find a vacant T sites at a higher rate than for  $\text{TiH}_{1.99}$  above this temperature.

### 3. Region III

Fig. 7.6 shows a concentration-independent plateau near room temperature for  $x=1.83$  and 1.97 and suggests that the same might be observed for  $x=1.99$  if the measurements were extended to a higher temperature. The value of

$\Lambda$  for this plateau is  $0.175(2) \mu\text{s}^{-1}$  which agrees with the value obtained from fitting the depolarization rate in region I to Eqn. 7.3 of  $0.172(5) \mu\text{s}^{-1}$ . The  $\Lambda$  value for a muon in a T site and no local distortion does not agree with this. One possible explanation is that there is a vacancy next to the muon in the T site. However, the probability of this occurring for the  $x=1.97$  sample is extremely small assuming that a nearest-neighbor vacancy is not bound to the muon. A reasonable alternative is to assume a  $2.6(4)\%$  lattice distortion or  $0.06(1) \text{ \AA}$  relaxation of the nearest-neighbor hydrogens. For  $\text{TiH}_{1.99}$  and  $\text{TiD}_{1.99}$ , the spacing between T sites is  $2.227(1)$  and  $2.220(1) \text{ \AA}$ , respectively,<sup>40</sup> and can be parameterized by an equation with a term proportional to the zero-point motion of the particle ( $1/\sqrt{m}$ ) plus a second term equal to a constant.

$$a = a_0 + k/\sqrt{m} \quad (7.9)$$

If  $m$  is set equal to the mass of the muon, then the distance between T sites is  $2.27(3) \text{ \AA}$ . This agrees with the value of  $2.285(9) \text{ \AA}$  for the muon-hydrogen distance obtained from the muon depolarization rate.

#### 4. Region IV

Fig. 7.6 shows a region of motional narrowing at high temperatures. This may be associated with the activation

of the hydrogen atoms out of T sites. Using the values of  $\tau$ , the field-correlation time, obtained from a fit to an Abragamian form for  $G_x(t)$ , the correlation times are plotted as a function of inverse temperature in Fig. 7.9. The muon field-correlation time disclosed in this figure is of the same order of magnitude as that of the proton, but the activation energies (the slope of the lines) for the muon and the proton ( $0.507(10)$  eV)<sup>21</sup> are quite different. The results of least squares fits to Eqn. 7.10 with  $\tau_0$  and  $E_a$  as the free parameters are shown in Table 7.2

$$\tau = [\tau_0/(1-x/2)] \exp(E_a/KT) \quad (7.10)$$

These results are in direct contradiction to classical blocking theory since the motion of the muon should be impeded by that of the hydrogen atoms.

Table 7.2

Prefactor and activation energy for fits using Eqn. 7.10 to  $TiH_x$  data.

$x$	$\tau_0(\mu s)$	$E_a(eV)$
1.83	$1.4(7) \times 10^{-6}$	0.38(2)
1.97	$1.9(9) \times 10^{-6}$	0.38(3)

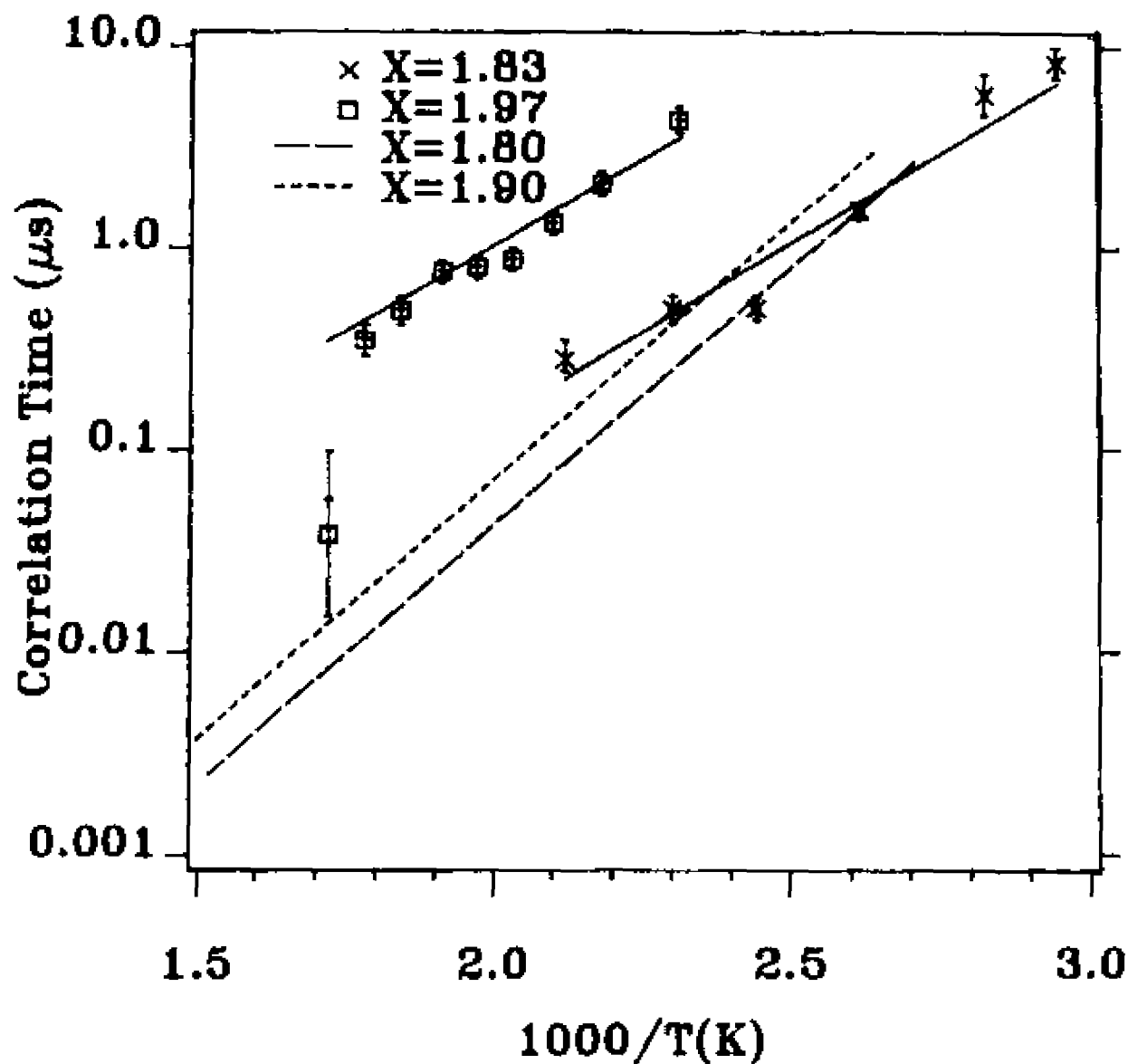


Figure 7.9 (Kossler et al.<sup>34</sup>)  
 Muon field-correlation time plotted as a function of temperature for  $\text{TiH}_{1.83}$  and  $\text{TiH}_{1.97}$ . The lines through these points are a least squares fit to Eqn. 7.10. The dashed lines correspond to proton correlation times measured by NMR.<sup>21</sup>

Secondly, since  $\tau_0$  is independent of concentration, the field-correlation time is inversely proportional to the vacancy concentration. This indicates that the change of the field at the site of the muon is dependent upon the motion of vacancies. This will involve the motion of the nearest-neighbor protons, the muon, or both. A second way to see this is to select data points where field-correlation times are equal for both samples and calculate the  $c\Gamma_V$  product where  $c$  is the vacancy concentration and  $\Gamma_V$  is the vacancy jump rate given by  $36 \times 10^{12} \text{s}^{-1} \exp(-E_a/kT)$  (where  $E_a = 0.507 \text{ eV}$  is the proton activation energy).<sup>21</sup> The temperatures for which the two samples have approximately equal correlation times are 435 K and 543 K which yield  $c\Gamma_V$  products of  $4(1) \times 10^6 \text{ s}^{-1}$  and  $11(6) \times 10^6 \text{ s}^{-1}$  for  $x=1.83$  and  $1.97$ , respectively. Since the values for  $c\Gamma_V$  are the same within the uncertainties, the muon field-correlation time is dependent on vacancy motion as was shown previously.

The discrepancy between activation energies measured by  $\mu$ SR and NMR has been observed in other metal hydride systems, such as  $\text{ZrH}_x$ ,<sup>33</sup>  $\text{NbH}_x$ <sup>27</sup> and  $\text{PdH}_x$ .<sup>51</sup> This discrepancy appears to be limited to hydrides with a hydrogen concentration greater than 60%, because the  $\mu$ SR data of Doyama et al.<sup>33</sup> in  $\text{VH}_{0.503}$  shows that the motion of the muon is limited by the motion of protons. Richter et al.<sup>27</sup>, using Monte Carlo calculations for tracer diffusion, have developed a model to explain the muon cor-



relation time in  $NbH_x$ . They find that the field-correlation time is a function of muon and proton attempt frequencies and hydrogen concentration.

$$\tau = \frac{1}{\Gamma_{\mu}(1-x/2)} + \frac{1-f}{\Gamma_H(1-x/2)f} \quad (7.11)$$

The quantities  $\Gamma_{\mu}$ ,  $\Gamma_H$  and  $f$  are the muon jump frequency, the proton jump frequency and the correlation coefficient, respectively. The problem of tracer diffusion for one-dimensional lattice has been solved analytically by Petzinger.<sup>50</sup> He finds, as Richter et al.<sup>27</sup> did in their Monte Carlo simulations, that the time,  $\tau$ , is a measure of the mean time for a vacancy to diffuse to the site of the muon. Richter et al.<sup>27</sup> assume that the time,  $\tau$ , is equal to the muon field-correlation time measured by  $\mu$ SR. However, since the proton has a sizeable magnetic moment, the field-correlation time is not equal to the auto-correlation time if the protons are also moving. Gygax et al.<sup>51</sup> have postulated for  $PdH_x$  that the hydrogen atoms surrounding the muon move slower than those not near the muon. However, they give no reason why the nearest-neighbor hydrogen atoms move slower. Hartmann et al.<sup>52</sup> (Richter included) have also adopted this picture for  $NbH_x$ , but also fail to give an explanation. Gygax et al.<sup>53</sup> have performed muon spin depolarization measurements on single-crystal  $PdH_{0.74}$  and find a decrease in the occupancy of

nearest-neighbor hydrogen sites as the temperature increases. This seems to contradict their earlier explanation concerning the slower motion of the nearest-neighbor hydrogens. However, they do not comment on this discrepancy. Doyama et al.<sup>33</sup> have also observed the disagreement between proton and muon activation energies in  $ZrH_x$ , but give no explanation. The Monte Carlo simulations described in Chapter 6 have been employed to try to understand this problem.

Since the muon is sensitive to changes in its magnetic environment, the field-correlation time is the significant quantity. In Table 6.1, results of the Monte Carlo simulations for  $p_r$  are given as a function of various movement probabilities for the vacancy. In order to compare the data to the results of the simulations, the  $p_r$  product for each temperature point must be calculated. Korn and Zamir<sup>21</sup> have determined the hydrogen jump rate,  $\Gamma$ , as a function of concentration,  $x$ , and temperature for  $\gamma$ -TiH<sub>x</sub>.

$$\Gamma = \Gamma_0(1-x/2)\exp(-E_a/kT) \quad (7.12a)$$

$$\text{where } \Gamma_0 = 36(7) \times 10^{12} \text{ s}^{-1} \quad (7.12b)$$

$$\text{and } E_a = 0.507(10) \text{ eV} \quad (7.12c)$$

The vacancy motion rate,  $\Gamma_v$ , is the same as that for the protons without the blocking factor.

$$\Gamma_v = \Gamma_0 \exp(-E_a/kT) \quad (7.13)$$

For a simple cubic lattice, the probability,  $p$ , for motion of a vacancy equals  $\Gamma_v/4$ .<sup>38</sup> Using this, the  $p\tau$  product for  $\text{TiH}_{1.97}$  can be calculated. The results of this are shown in Table 7.3. The uncertainties in the  $p\tau$  product result from the uncertainties in  $\tau$ ,  $\Gamma_0$  and  $E_a$ .

With the exception of the point at 583 K,  $p\tau$  is on the order of 50 or greater. For a stationary muon, the  $p\tau$  product is equal to 52 (Table 6.1). This is less than several of those listed below. From the results in

Table 7.3  
 $p\tau$  products for  $\text{TiH}_{1.97}$  data.

<u>T(K)</u>	<u><math>\tau</math> (<math>\mu\text{S}</math>)</u>	<u><math>p\tau</math></u>
432	4.3(7)	$5(2) \times 10^1$
458	2.1(3)	$5(2) \times 10^1$
477	1.3(2)	$5(2) \times 10^1$
493	0.9(1)	$5(2) \times 10^1$
508	0.8(1)	$7(2) \times 10^1$
523	0.8(1)	$9(3) \times 10^1$
543	0.49(9)	$9(3) \times 10^1$
563	0.35(7)	$9(3) \times 10^1$
583	0.04(6)	$1(2) \times 10^1$

Table 6.1, it is seen that for  $\mu_r$  to equal 90, the probability for a vacancy to become a nearest neighbor to the muon must be decreased. This will be used in the development of models in the following paragraphs.

One possible explanation of the data in light of the results of the simulations is that the motion of the muon is limited to nearest-neighbor hopping and that there exists an attractive force between the muon and the nearest-neighbor hydrogens. However, this picture has difficulty explaining the measured muon activation energy for the following reason. If the nearest-neighbor protons are bound, the activation energy for these hydrogen atoms to move would be greater than that for hydrogen atoms not near the muon. In other words, the activation energy measured by the muon should be  $E_a + \Delta U$  where  $E_a$  is the activation energy for protons not near the muon and  $\Delta U$  is the additional binding energy of the nearest-neighbor protons. However, the activation energy associated with the muon field-correlation time is less than  $E_a$  rather than greater.

A second possibility is that it is not energetically favorable for a vacancy to occupy a nearest-neighbor site and that the muon tunnels to a second-nearest-neighbor site. This idea is encouraging for two reasons. The first is that the nearest-neighbor hydrogens do not move which allows the field correlation time to be larger than is measured by NMR. Secondly, the polaronic motion of the

muon allows for a small prefactor and small activation energy for the correlation time. If this is the case, a qualitative model can be developed.

Neutron scattering has confirmed that the potential which describes transitions between vibration states for protons in  $\gamma$ -TiH<sub>x</sub> is approximately harmonic.<sup>35</sup> For hydrogen diffusion to occur, the protons must be in an excited state to tunnel through a barrier to a vacant site. The presence of the muon distorts the nearest-neighbor titanium atoms and causes the potential to be anharmonic. This change in energy levels and spacing reduces the probability for a nearest-neighbor proton to tunnel to a second-nearest-neighbor tetrahedral site and causes the proton to be bound to this site.

Since the postulated model does not allow or limits motion of the muon to nearest-neighbor tetrahedral sites, the muon presumably diffuses to second- or third-nearest-neighbor sites. The small prefactors reported in Table 7.2 indicate that the motion of the muon is polaronic in nature. As was mentioned in Chapter 6, Bisson and Wilson<sup>37</sup> have calculated the activation energies for protons in T sites of  $\gamma$ -TiH<sub>x</sub> for second- and third-nearest-neighbor diffusion paths to be 0.69 and 0.65 eV, respectively. Since the energy difference between these two paths is small, and the distance to the second-nearest-neighbor site is shorter by a factor of  $\sqrt{2/3}$ , the likely path for muon diffusion is across the cube face of the hydrogen

sublattice using a thermally-activated tunneling mechanism. This model suggests that the hopping rate ( $1/\tau$ ) can be fitted to a form similar to Eqn. 4.3. However, since the number of vacant T sites is limited, a factor must be incorporated to account for the effective vacancy concentration,  $c_v$ , and the coordination number,  $Z$ .

$$\frac{1}{\tau} = Z c_v \frac{J^2}{\hbar} \left( \frac{\pi}{4E_a kT} \right)^{1/2} \exp(-E_a/kT) \quad (7.14)$$

The coordination number is the number of second-nearest-neighbor sites to which the muon can tunnel. For this geometry,  $Z$  equals twelve. The results of fitting the data to Eqn. 7.14 are given in Table 7.4 and are shown in Fig. 7.9. A value for  $J$  will be given following a discussion of  $c_v$ .

Table 7.4

Tunneling matrix elements and activation energies for fits using Eqn. 7.14 to  $TiH_x$  data.

$x$	$\sqrt{c_v}J$ (meV)	$E_a$ (eV)
1.83	0.56(2)	0.36(5)
1.97	0.18(1)	0.36(1)

The effective vacancy concentration,  $c_v$ , is the probability that the second-nearest-neighbor site is vacant. The expected minimum value for this quantity is the nominal vacancy concentration which assumes that the probability for a vacancy to occupy any T site is equal. Energies for vacancy occupation of different sites can be assigned. A simple model would assign an energy of  $E_1$  ( $E_1 > 0$ ) to the nearest-neighbor sites,  $E_2$  ( $E_2 < 0$ ) to the second-nearest-neighbor sites and  $E_3$  for the remaining sites in the lattice. This models the decrease in vacancy occupancy of the nearest-neighbor sites. Since a site can be in one of two states (vacant or occupied), the distribution of vacancies is characterized by a Fermi distribution function ( $E_3 = 0$ ):

$$c_1 = \frac{c}{c + (1-c)\exp(\beta E_1)} \quad (7.15)$$

where  $c$  is the nominal vacancy concentration. In order to decrease the number of independent parameters in this model, let us assume that  $E_1$  equals  $-E_2$ . The ratio  $c_2/c_1$  is greater than 10 for  $c$ ,  $E_2$  and  $T$  equal to 0.015 ( $x=1.97$ ),  $-50$  meV and 500 K, respectively. This temperature was chosen, because the  $\mu$ SR measurements were made in this vicinity for  $x=1.97$  ( $c=0.015$ ). The value of 50 meV is not unreasonable since energies associated with the lattice are of this order. The value of  $c_2$  from above is

0.05(2) which can be used along with the result in Table 7.4 to find a value for  $J$ . For  $x=1.83$ ,  $c_2$  is equal to 0.23(2) under the same conditions as the preceding calculation. Using these values for  $c_V$  ( $c_2$ ), the values for  $J$  were calculated and are presented in Table 7.5. The agreement between the two values for the tunneling matrix element is reasonable.

Although the value for  $J$  in aluminum is 2.3 meV for a tunneling distance of 2.02 Å,<sup>20</sup> the calculated values for the tunneling matrix element in  $TiH_x$  seem large considering the distance of 3.15Å between the two sites.

Table 7.5

Probability for the existence of a vacancy at a second-nearest-neighbor site ( $c_V$ ), tunneling matrix element ( $J$ ), and activation energy for the two  $\mu$ SR titanium hydride samples at 500 K ( $E_A$ ).

$x$	$c_V$	$J$ (meV)	$E_A$ (eV)
1.83	0.23(2)	1.2(1)	0.36(5)
1.97	0.05(2)	0.8(2)	0.36(1)

The value of  $J$  may be estimated with the Mathieu formula (Eqn. 4.7). If one assumes that  $V_0$ , the barrier height, is equal to the proton activation energy calculated by Bisson and Wilson, 0.69 eV, and substitutes the mass of the muon and the distance between second-nearest-



neighbor sites for m and d, respectively, the value calculated for J is 7  $\mu\text{eV}$ . The energy for zero-point motion of a muon can be calculated from the energy for zero-point motion of a proton in  $\gamma\text{-TiH}_x$ , 0.21 eV,<sup>21</sup> and is 0.65 eV. Since the energy for zero-point motion of a muon is almost equal to the barrier height, the value of J from the Mathieu formula is a severe underestimation of the actual value by a couple orders of magnitude. However, the experimentally derived value of the tunneling matrix element is probably too large compared to that found for muons in aluminum where J is twice as big for approximately half the tunneling distance.

A second aspect of this model to be investigated is the activation energy. This is a measure of the coupling between the lattice and the muon. The results from inelastic neutron scattering in  $\text{TiH}_2$  show discrete levels for the hydrogen atoms implying that the T-site protons are not coupled.<sup>35</sup> Therefore, the T-site muon only couples to the four nearest titanium atoms. This does not contradict the postulate concerning the distortion of the local hydrogen lattice from the previous section, since the displacement of the titanium atoms can cause this. The acoustic mode for  $\text{TiH}_2$  has an energy ( $\hbar\omega_D$ ) of 39(3) meV as measured by inelastic neutron scattering.<sup>54</sup> Using Eqn. 7.16, the force constant, k, can be calculated.<sup>55</sup>

$$\hbar(2k/M)^{1/2} = \hbar\omega_D/2 \quad (7.16)$$

The variables  $M$  and  $\omega_D$  are the mass of the titanium atom and the acoustic mode frequency, respectively. This yields a value of  $2.2(6)$  eV/Å<sup>2</sup> for the force constant. The polaron binding energy,  $E_0$ , is equal to twice the activation energy. The true activation energy,  $E_a$ , is approximately  $0.41(2)$  eV. The difference between the measured, which was obtained from the muon field-correlation times and the actual activation energies is due to the inclusion of the exponential in  $c_v$  (Eqn. 7.15) to Eqn. 7.14. The four nearest titanium atoms must, therefore, relax  $0.4(1)$  Å to accommodate a polaron binding energy,  $E_0$ , of  $0.82(4)$ . This large value for the polaron binding energy implies that the coupling between the muon and the lattice is very large. Eqn. 7.17 yields a value of  $1.9(3)$  eV/Å for the coupling constant,  $g$ .<sup>55</sup>

$$E_a = g^2/4k \quad (7.17)$$

This value for the coupling constant is approximately three times greater than that for muons in copper.<sup>55</sup>

In summary, this model has the attractive feature that the measured field-correlation time for the muon is equal to its diffusion-correlation time. It allows for a binding of the hydrogen to nearest-neighbor sites. However, the experimentally determined parameters  $J$  and  $E_a$

are much too large compared to values obtained from simple calculations.

The models presented are two different attempts to explain the high temperature data for  $TiH_x$ . Each one has its advantages and disadvantages. The first model is an attempt to decrease the proton diffusion in the vicinity of the muon, yet allow the muon to jump to nearest-neighbor sites. However, an increased activation energy to explain the binding of the nearest-neighbor protons was not measured. The second model postulates that it is energetically favorable to have a vacancy at a second-nearest-neighbor site as opposed to a first-nearest-neighbor site and that the muon moves by a thermally-activated tunneling mechanism. The flaws with this theory are that the values obtained from the data for the tunneling matrix element and the activation energy are very large. However, the large value for  $J$  should not discount this theory since substantial values have been observed in other FCC metals contrary to theoretical expectations.

#### B. Yttrium Hydride

The temperature dependence of the depolarization rate,  $\Lambda$ , for the yttrium hydride samples is shown in Fig. 7.10. As was the case for titanium hydride, the data shown here can be divided into four different regions.

The line width for muon occupancy of the O and T sites may be calculated using the Van Vleck formula

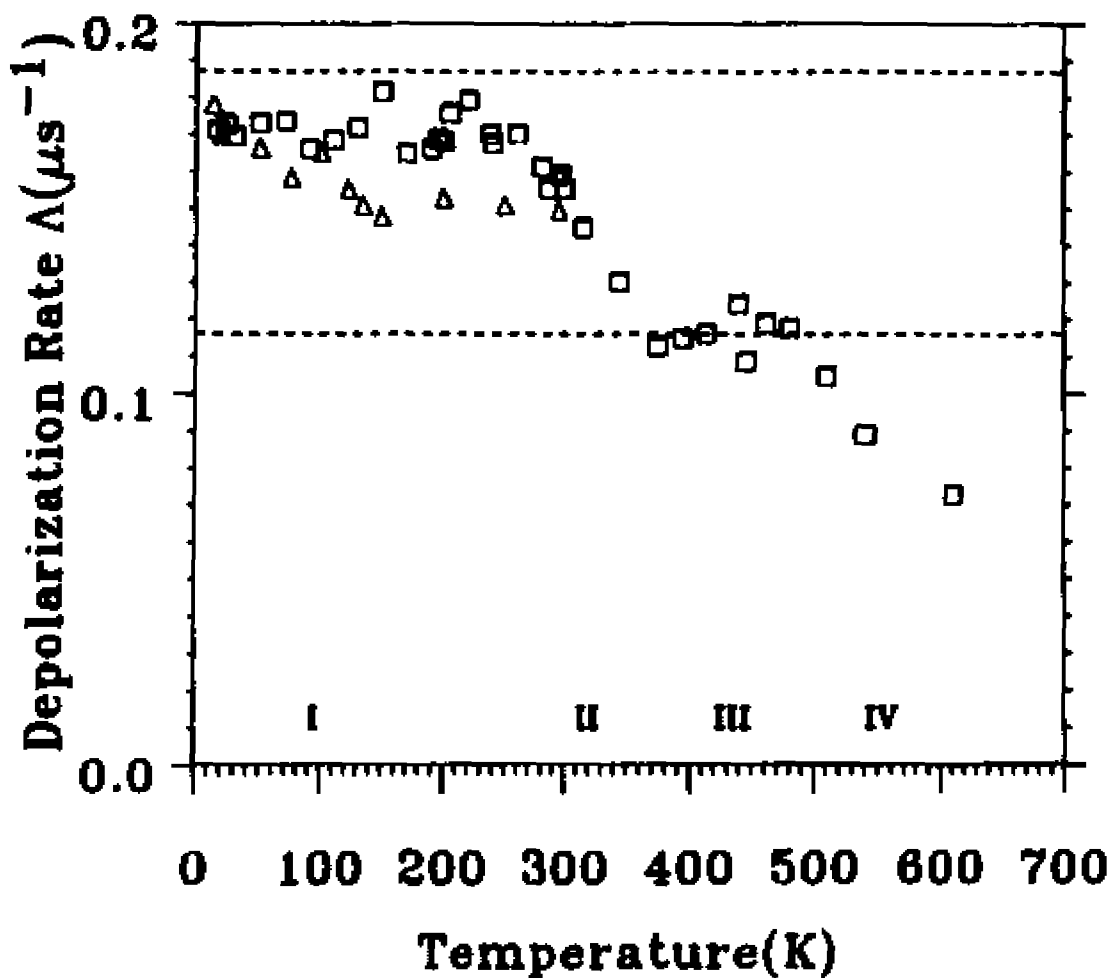


Figure 7.10  
 The depolarization rate,  $\Lambda$ , in yttrium hydride as function of temperature for  $\text{YH}_{1.77}$  (open squares) and  $\text{YH}_2$  (open triangles). The dashed lines correspond to the depolarization rate for a muon in an octahedral site (upper line) and a tetrahedral site (lower line) of an undistorted lattice.

(Eqn. 7.1) coupled with an allowance for the reduction of the fourth moment as mentioned previously (section 7.1A.1). Using a value for the lattice parameter of 5.204 Å,<sup>43</sup> the line widths for O and T site occupancy with no local distortion are  $0.186 \mu\text{s}^{-1}$  and  $0.120 \mu\text{s}^{-1}$ , respectively.

#### 1. Region I

Fig. 7.10 shows an increase in the value of the depolarization rate as the concentration is decreased for  $T < 300$  K. This is considerably different from that for  $\text{TiH}_x$ . This can be explained by allowing a greater percentage of O sites to be occupied by protons as the hydrogen concentration is increased. The occupation of O sites by protons has been observed by neutron diffraction<sup>56</sup> and proton second moment measurements with NMR<sup>57</sup> and is shown in Table 7.6.

Table 7.6

Percentage of occupied octahedral sites in yttrium hydride as a function of hydrogen concentration and temperature as measured by neutron scattering<sup>56</sup> and NMR.<sup>57</sup>

<u>H/Y</u>	<u>Percentage of Occupied O Sites</u>	<u>Temperature(K)</u>
1.98 <sup>56</sup>	12(6)	11
1.98 <sup>56</sup>	14(3)	300
1.98 <sup>57</sup>	16(3)	160 and 200
1.92 <sup>57</sup>	11(2)	160 and 200

The experimental results for  $\Lambda$  can be fit to a model in which a probability for occupancy of a T site by the muon is calculated. The probability that a muon, shortly after stopping in an O site, transfers to a T site is equal to the probability that a nearest-neighbor tetrahedral site to the octahedral site is vacant. Thus, if  $P_T^V$  is the probability that a T site is vacant and  $P_T^\mu$  is the probability that the muon is in a T site (and is equivalent to P for  $TiH_x$ ), one has

$$P_T^\mu = 8P_T^V \quad (7.18a)$$

$$\Lambda_{EXP}^2 = 8P_T^V \Lambda_{TET}^2 + (1-8P_T^V) \Lambda_{OCT}^2 \quad (7.18b)$$

For H/Y-2,  $P_T^V = P_O^H/2$  where  $P_O^H$  is the probability for an O site to be occupied by a proton. Since the ratio of unit cell volumes between yttrium hydride and titanium hydride is 1.6, then the distortion of the lattice for a muon in an O site should be very small. Using the unexpanded lattice calculated values for the line width for both sites, the probability for occupancy of T sites is shown in Table 7.7.

Table 7.7

Percentage of tetrahedral sites occupied by muons ( $P_T^{\mu} \times 100$ ) in yttrium hydride as a function of temperature and hydrogen concentration. The percentage of O sites occupied by hydrogen is  $P_O^H \times 100$ .

H/Y	$\Lambda_{\text{EXP}} (\mu\text{s}^{-1})$	$P_T^{\mu} \times 100$	$P_O^H \times 100$
1.77	0.171(2)	3.3(4)	-
2.00 (T>50K)	0.153(2)	6.9(4)	13.8(8)
2.00 (T<50K)	0.171(3)	3.3(4)	6.6(8)

The percentage of O sites occupied by hydrogen for  $\text{YH}_2$  above 50 K, as determined by  $\mu\text{SR}$  agrees, with the results from neutron scattering. A new equilibrium in the ratio of occupied O to T sites is observed by the change (near 50 K) in the percentage of protons occupying O site and appears to be stable until room temperature is reached.

The mixed phase sample,  $\text{YH}_{1.77}$ , is comprised of many small regions where the lattice structure is either HCP ( $\alpha$ ) or FCC ( $\beta$ ). The  $\alpha$  phase, which has a lattice constant of 3.65 Å, can contain up to a H/Y ratio of 0.15 at room temperature.<sup>58</sup> The volume available for muon occupancy in a T site in the  $\alpha$  phase is less than 30% of that for a muon in an O site in the  $\beta$  phase. Therefore, one can postulate that the muon chooses to occupy sites in the  $\beta$  phase of the material (which is 90% of this material and

has an average  $H/Y \sim 1.93$ ). Since the vacancy concentration in the  $\beta$  phase of this material is approximately 3.5% and 3.3(4)% of the T sites are vacant (as determined from  $\mu$ SR linewidths), it appears that there are no protons in the octahedral sites of this phase.

## 2. Region II

A region of transition to a lower height plateau for the depolarization rate in  $YH_{1.77}$  is observed in Fig. 7.10 and commences at approximately 270 K. This is associated with the muons activating out of O sites. The occurrence of this at a much higher temperature than for  $TiH_{1.83}$ , shown in Fig. 7.6 (200 K), reflects the difference in the structure of the materials.  $TiH_{1.83}$  is a single phase material with the H atoms not occupying O sites and the vacancies randomly distributed among the T sites; whereas,  $YH_{1.77}$  is a mixture of  $\alpha$  (which does not have room for the muon) and  $\beta$  phases. The  $\beta$  phase of this material has a nominal H/Y ratio at 175 K of approximately 1.93 with the hydrogen atoms occupying T sites. Further, muon occupancy of the O site causes little or no local lattice dilation which means that the attractive force between the muon in an O site and a second-nearest-neighbor vacancy is smaller than in the titanium hydride system. These two distinctions cause the transition region for  $YH_{1.77}$  to occur at higher temperatures than for titanium hydride of a similar concentration. Presumably the  $YH_2$  would have shown signs



of transition to T site occupancy slightly above room temperature if the measurements had been carried out.

### 3. Region III

The constant value for the depolarization rate,  $\Lambda$ , in Fig. 7.10 above 300 K indicates that the muon is trapped. The average value of  $\Lambda$  in this region is  $0.116(2) \mu\text{s}^{-1}$ . This agrees with the calculated unexpanded lattice value of  $0.120 \mu\text{s}^{-1}$  for T site occupation. The reason why there is no local lattice dilation is that this lattice is more spacious than  $\text{TiH}_x$ . Therefore, the muon's zero point motion does not cause a repulsion of the local hydrogen atoms.

### 4. Region IV

Motional narrowing of the muon line width is observed at high temperatures (Fig. 7.10). Similar behavior was also observed for  $\text{TiH}_x$  and was due to the motion of muons and possibly hydrogen atoms. Fig. 7.11 shows the values of  $\tau$  from a fit to an Abragamian form for  $G_x(t)$ . These correlation times can then be fit to an Arrhenius form to obtain an activation energy.

$$\tau = \tau_0 \exp(E_a/kT) \quad (7.19)$$

A fit to this form yields  $4(\pm 2) \times 10^{-4} \mu\text{s}$  and  $0.44(8) \text{ eV}$  for  $\tau_0$  and  $E_a$ , respectively.  $T_{1\rho}$  measurements have been

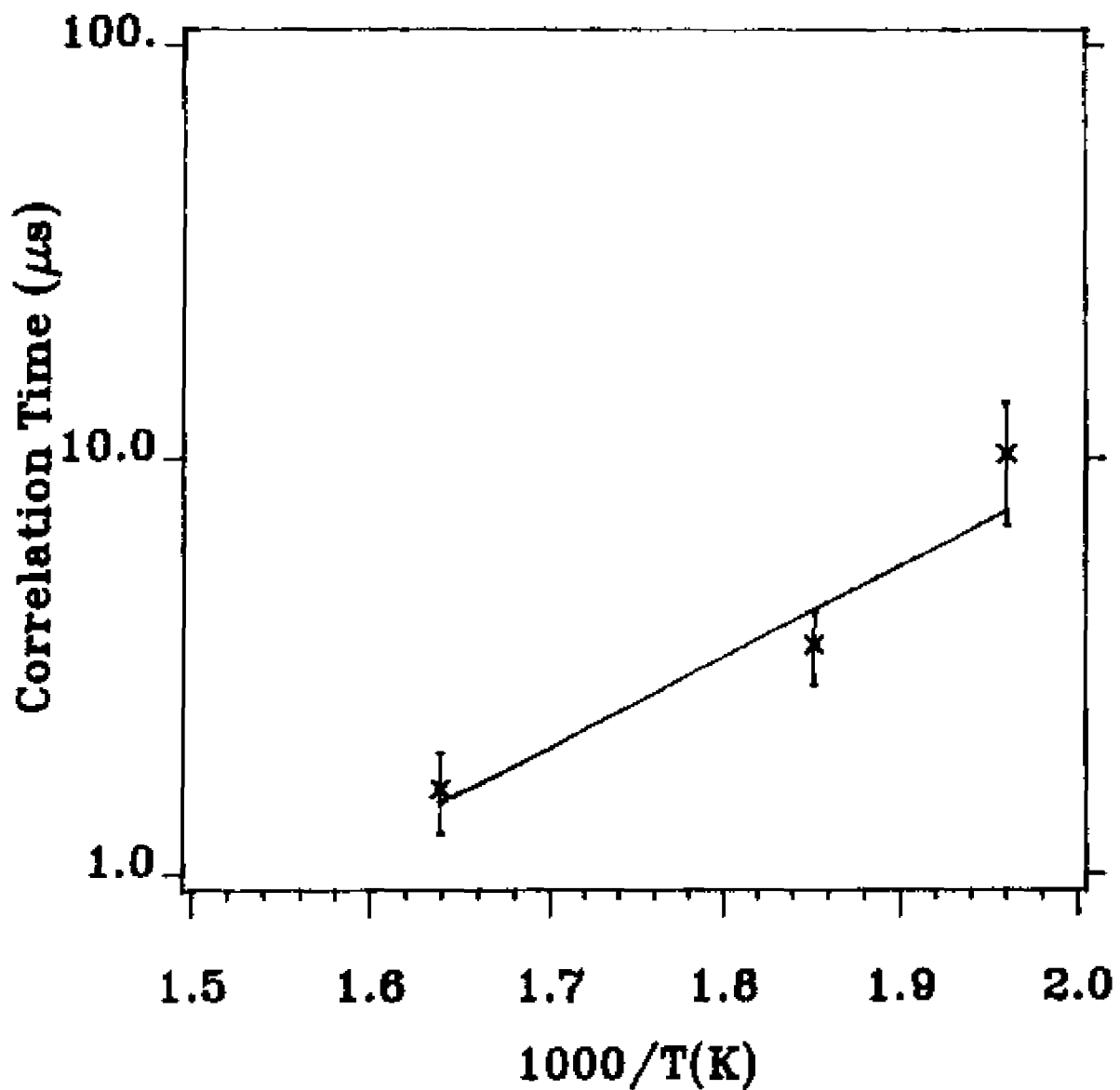


Figure 7.11  
Muon field-correlation time plotted as a function of  
temperature for  $\text{YH}_{1.77}$ . The line is a least squares fit to  
Eqn. 7.19.

performed on  $\text{YH}_{1.72}$  by Anderson et al.<sup>59</sup> Their results have been analyzed using a form similar to Eqn. 7.19 over three different temperature ranges yielding three different activation energies and are reported in Table 7.9.

Table 7.8

Prefactor and activation energies for proton correlation times obtained from  $T_{1\rho}$  measurements.<sup>59</sup>

Temperature region	$\tau_0(\mu\text{s})$	$E_a(\text{eV})$
$T < 465 \text{ K}$	$2.2 \times 10^{-3}$	0.457
$465 \text{ K} < T < 600 \text{ K}$	$6.9 \times 10^{-8}$	0.877
$T > 600 \text{ K}$	$9.4 \times 10^{-10}$	1.1

Their interpretation of the three regions of increasing activation energy with increasing temperature is motion between O sites for the lowest  $E_a$ , exchange between T- and O-site hydrogen atoms, and motion of all hydrogen atoms on both sublattices. However, this interpretation may be suspect since they were not able to determine the proton O and T site populations with proton second moment measurements. The activation energy observed for muons is close to that observed for O site hydrogens which might imply that the muon's field-correlation time is somehow determined by the motion of these protons. However, this is unlikely, because the values for  $\tau_0$  and  $E_a$  for  $\text{YH}_{1.77}$  are

on the same order as those for  $TiH_x$  for which hydrogen atoms do not occupy O sites. Secondly, the uncertainties in  $r_0$  and  $E_a$  are quite large. Further, our results for  $YH_{1.77}$  indicate that protons do not occupy O sites. Therefore, detailed conclusions are premature.

### C. Zirconium Hydride

Zirconium hydride has been studied previously with  $\mu$ SR. Doyama et al.<sup>33</sup> reported the depolarization rate for samples with H/Zr ratios of 1.54, 1.90, and 1.99 and  $T > 273$  K (Fig. 7.12). They also have reported an activation energy and a prefactor for the jump frequency for the muon which is lower than the proton activation energy and attempt frequency obtained from NMR. The studies reported here are for  $ZrH_{1.94}$  for  $T < 300$  K (Fig. 7.13).

For  $T \leq 100$  K, the average value for the depolarization rate is  $0.199(2) \mu s^{-1}$ . Doyama et al.<sup>33</sup> measured a value for the depolarization rate in  $ZrH_{1.90}$  and  $ZrH_{1.99}$  for  $T=300$  K which corresponds to a  $\Lambda$  of  $0.15 \mu s^{-1}$ . This agrees reasonably well with the calculated value for the line width of  $0.155 \mu s^{-1}$  for a muon in a T site with no lattice expansion. Since zirconium and titanium hydrides are very similar, one can assume a model similar to the one postulated for the depolarization rate in  $TiH_x$  at low temperatures.

$$\Lambda_{EXP}^2 = \Lambda_{TET}^2 P + \Lambda_{OCT}^2 (1-P), \quad (7.20a)$$

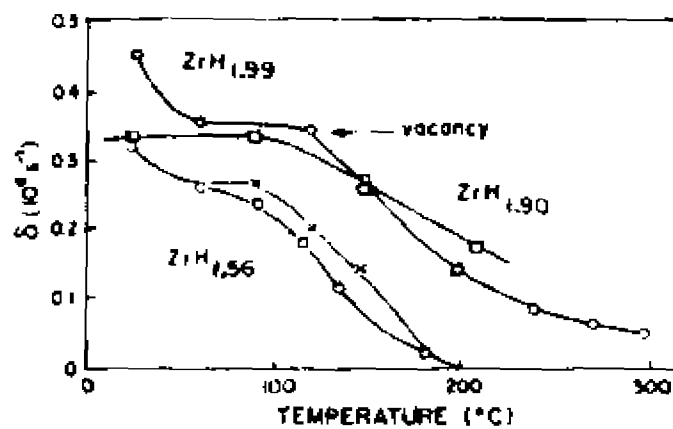


Figure 7.12 (Doyama et al.<sup>33</sup>)  
 The zero-field depolarization rate,  $\Delta_z$  ( $= \Lambda/\sqrt{5}$ ), as a function of temperature for  $ZrH_{1.99}$ ,  $ZrH_{1.90}$ , and  $ZrH_{1.56}$ . The data was fit to Eqn. 5.32 with  $\delta = \Delta$ .

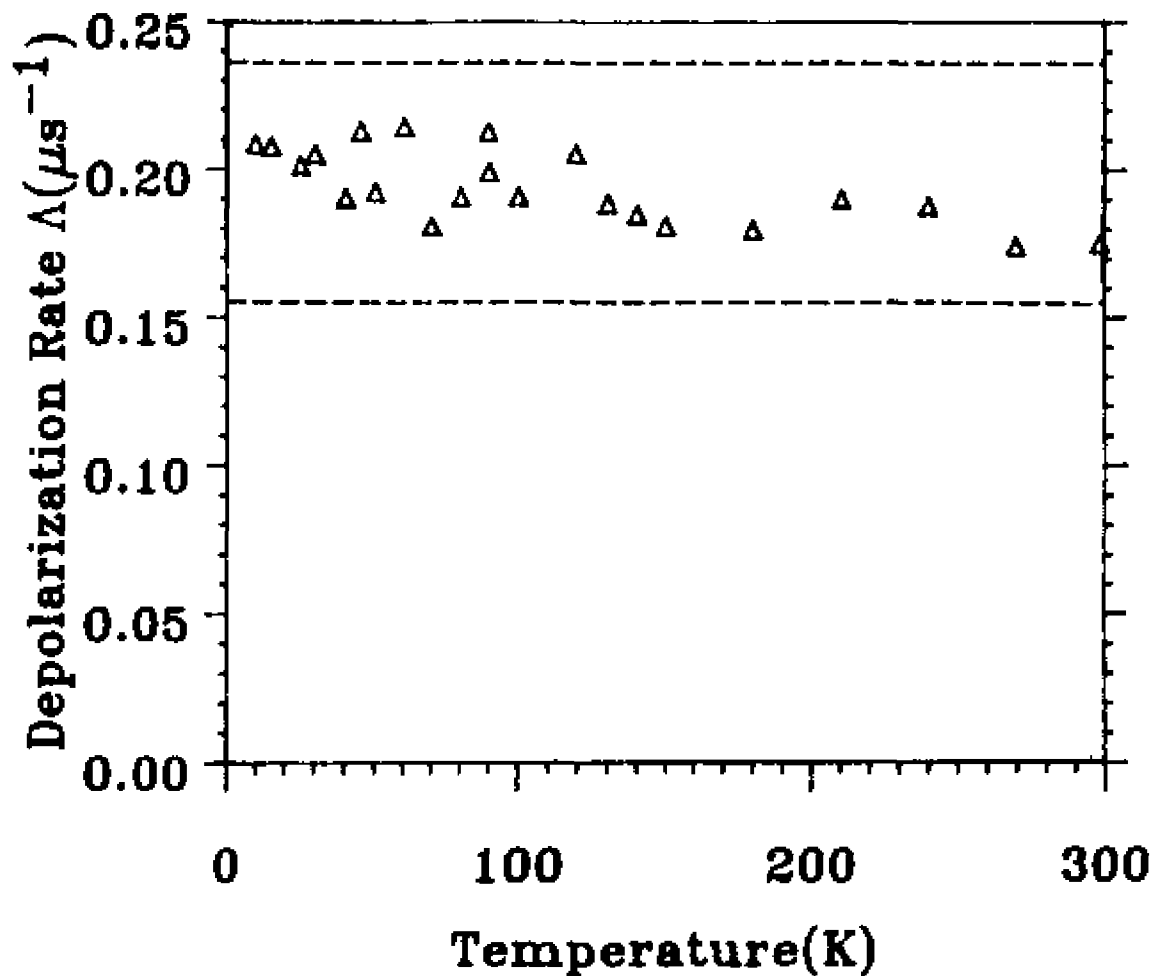


Figure 7.13  
The depolarization rate,  $\Lambda$ , as a function of temperature for  $\text{ZrH}_{1.94}$ . The dashed lines correspond to the depolarization rate for a muon in an octahedral site (upper line) and a tetrahedral site (lower line) with no local distortion.

$$\text{where } P = 8(1-x/2) \quad (7.20b)$$

If one assumes that the depolarization rate,  $\Lambda$ , determined from the data of Doyama et al.<sup>29</sup> (for  $ZrH_{1.90}$  and  $ZrH_{1.99}$  at 300 K) is equal to  $\Lambda_{TET}$  ( $0.15 \mu s^{-1}$ ) and that the depolarization rate for  $ZrH_{1.94}$  ( $T \leq 100$  K) is substituted for  $\Lambda_{EXP}$ , then the value of  $\Lambda_{OCT}$  is  $0.21(2) \mu s^{-1}$ . The value of  $\Lambda$  for a muon in an O site and no local distortion is  $0.237 \mu s^{-1}$ . A lattice expansion of  $4(4)\%$  is necessary to explain the disagreement between these two values for  $\Lambda_{OCT}$  and is compatible with the  $6(1)\%$  expansion for titanium hydride.

The depolarization rate for  $T > 150$  K is slightly lower than that for  $T \leq 100$  K (Fig. 7.13). For  $TiH_x$ , an attractive force for a vacancy to move to a nearest-neighbor T site to the muon was postulated to explain the decrease in the depolarization rate near 200 K for  $x=1.83$ . The motion of the vacancy to a nearest-neighbor T site is possible, because two or three of the second-nearest-neighbor sites can be vacant. Whereas for  $x=1.97$  and  $1.99$ , the probability for a vacant second-nearest-neighbor site is very small which means that the muon is trapped in the O site.  $ZrH_{1.94}$  is a good example of what occurs when the hydrogen concentration is in between these two extremes. For this concentration, there may be one nearest-neighbor or second-nearest-neighbor vacancy. This is reflected by the decrease in the depolarization rate around 200 K. If

the experiments were to be continued to a higher temperature one should see a decrease to a slightly (not much) lower value of the depolarization rate. This decrease in depolarization rate has been seen by Doyama et al.<sup>33</sup> They found muon T site occupancy at 280 K and 330 K for  $ZrH_{1.90}$  and  $ZrH_{1.99}$ , respectively (Fig. 7.12). Since not all the muons have activated out of an O site by room temperature for  $ZrH_{1.94}$  (but have for  $ZrH_{1.90}$ ), the postulated attractive force between a muon and a second-nearest-neighbor vacancy can be said to be observed only for vacancy concentrations in excess of 3%.

#### D. Lanthanum Hydride

Fig. 7.14 shows the muon spin depolarization rate as a function of temperature for  $LaH_{2.06}$ . The site determination of the muon is complicated by the presence of the dipole ( $2.78 \mu_N$ ) and quadrupole (0.220 barns) moments for the lanthanum nuclei which possess a spin of  $7\hbar/2$ .<sup>60</sup> The theoretical second moment is the sum of the contributions from the lanthanum and hydrogen nuclei. The Van Vleck formula (Eqn. 7.1) can be used to calculate the contributions to the muon second moment from both nuclei in the Zeeman limit. Upon performing this calculation, one finds that the line widths for muon occupancy of O and T sites is  $0.163 \mu s^{-1}$  and  $0.124 \mu s^{-1}$ , respectively. However, the quadrupole moment for lanthanum is large which means that 150 Gauss is probably not sufficient to achieve the Zeeman



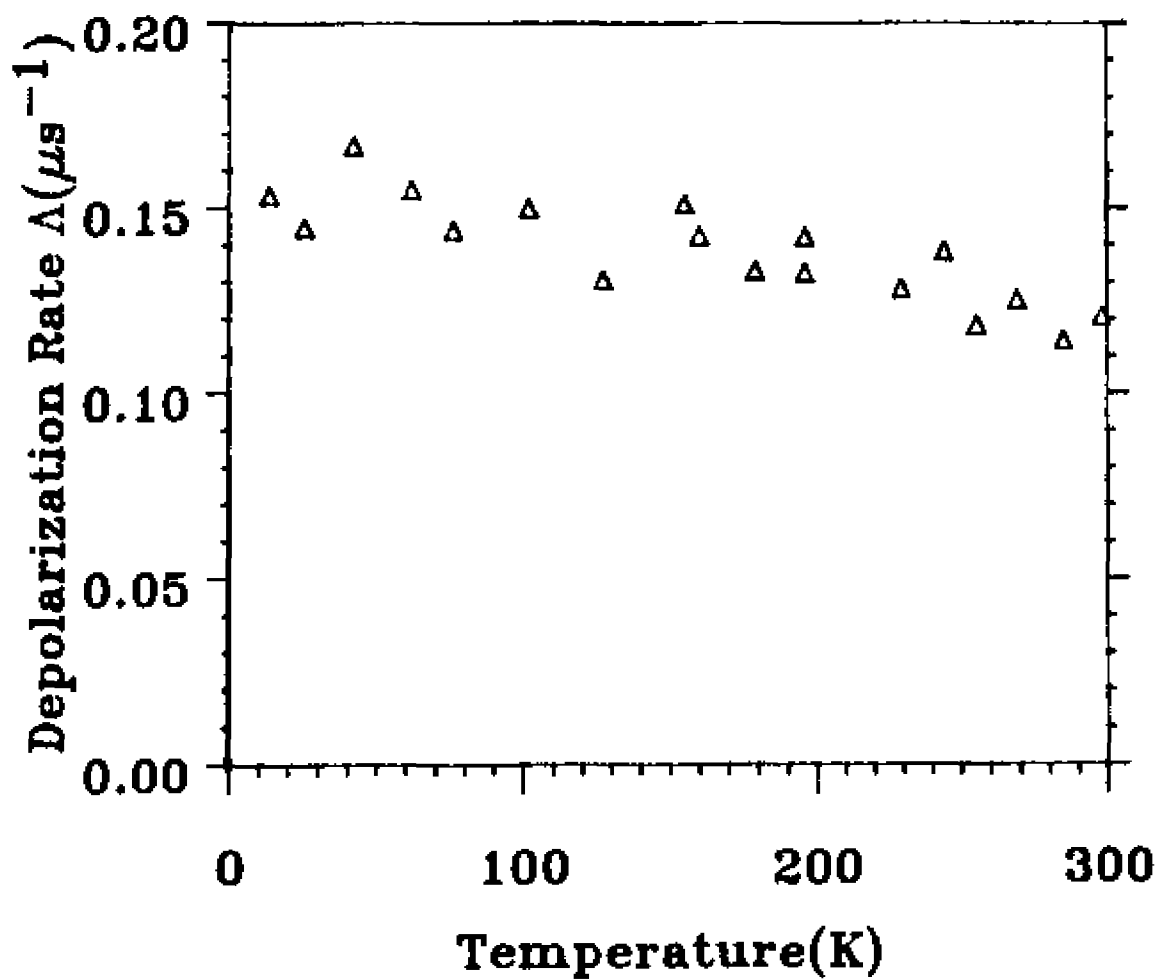


Figure 7.14  
The depolarization rate,  $\Delta$ , as a function of temperature  
for  $\text{LaH}_{2.06}$ .

limit. Instead of using Eqn. 7.1 to calculate the lanthanum contribution to the second moment, one must use Eqn. 5.16. Upon doing this, one finds that the line widths for muon occupancy of O and T sites is  $0.183 \mu\text{s}^{-1}$  and  $0.179 \mu\text{s}^{-1}$ , respectively. If 150 Gauss is not sufficient to quench the quadrupole interaction, then the site of the muon cannot be determined since the precision of our measurements is of the same order as the difference between line widths for both sites. However, one can postulate that the muon occupies O sites since the hydrogen atoms reside predominately in T sites. If one assumes this, then the experimentally observed line width yields a local lattice expansion of  $3.8(5)\%$  in the Zeeman limit and  $7.9(5)\%$  in the quadrupolar limit. Both of these are reasonable numbers for local lattice dilation for a muon occupying an O site.

As for  $\text{TiH}_{1.99}$ ,  $\text{LaH}_{2.06}$  has an extremely small number of vacant T sites. Therefore, one expects to observe motional narrowing of the line width if the muon is activating out of an O site and trying to find a T site. Since there is no motional narrowing of the muon line width, one can conclude that the muon is trapped.

## 7.2 ZERO-FIELD STUDIES

As was mentioned in Chapter 5, zero-field  $\mu\text{SR}$  has been a valuable technique for measuring internal fields and for measuring slow diffusion of the muon. In this

section, the zero-field  $\mu$ SR studies of  $TiH_x$  and  $YH_2$  are reported. Since the hydrogen atoms are the only nuclei with a sizeable magnetic moment, the results are a measure of the spin dynamics of the proton for temperatures where no muon or proton motion is expected.

#### A. Titanium Hydride

Fig. 7.15a-c shows the muon polarization as a function of time for  $TiH_{1.99}$ ,  $TiH_{1.97}$ , and  $TiH_{1.83}$  at 100 K. At this temperature, the muon is expected to be trapped and was observed to be by the transverse-field studies. One important feature of these three figures is the oscillation of the polarization at long times. This oscillation at long time disagrees with Kubo-Toyabe theory which predicts the polarization to approach 1/3 at long times for a static muon.<sup>29</sup> A calculation of the muon polarization in an O site which is coupled to the spins of the eight nearest-neighbor protons is shown in Fig. 7.15a-b.<sup>61</sup> The energy levels of the eigenstates were determined by diagonalizing the Hamiltonian with the proton-proton dipolar interaction included as a perturbation (see Appendix D). The results of this calculation give a better fit than Kubo-Toyabe theory for the muon polarization of a static muon for  $TiH_{1.99}$ . The fit to the polarization for  $x=1.97$  is not quite as good, but this is to be expected since the minimum is slightly shifted and filled in by the 12% of muons occupying T sites. No attempt was made to

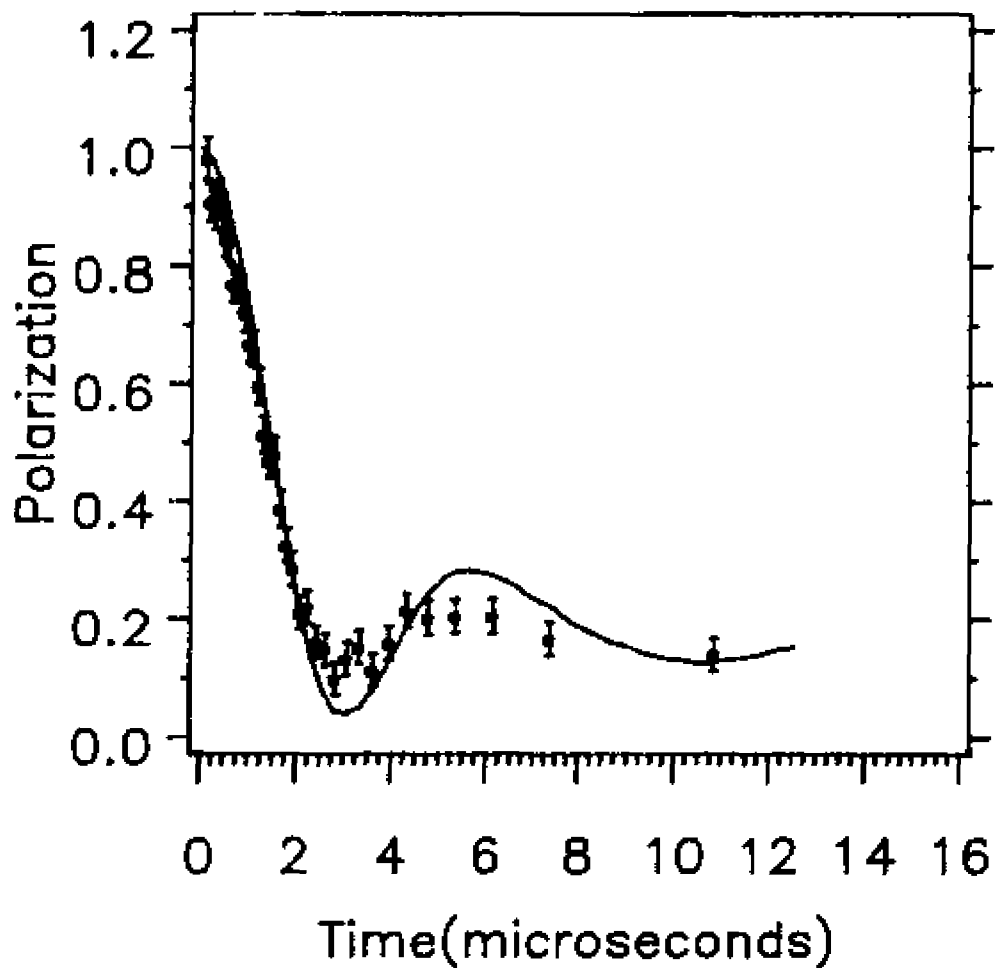


Figure 7.15a  
Experimentally-determined zero-field muon polarization as a function of time for  $\text{TiH}_{1.99}$  at 100 K. The curve is a theoretical calculation of the relaxation function for a muon in an octahedral site (see Appendix D).<sup>61</sup>

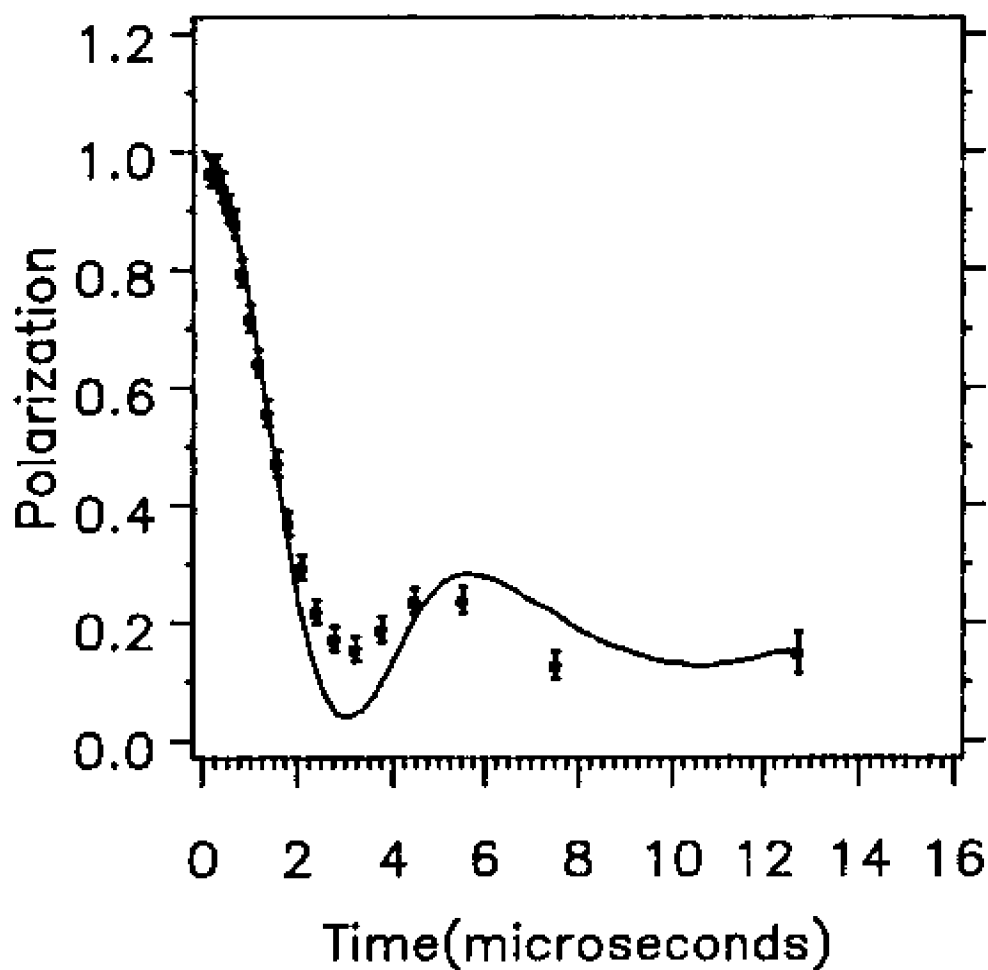


Figure 7.15b  
Experimentally-determined zero-field muon polarization as a function of time for  $\text{TiH}_{1.97}$  at 100 K. The curve is a theoretical calculation of the relaxation function for a muon in an octahedral site (see Appendix D).<sup>61</sup>

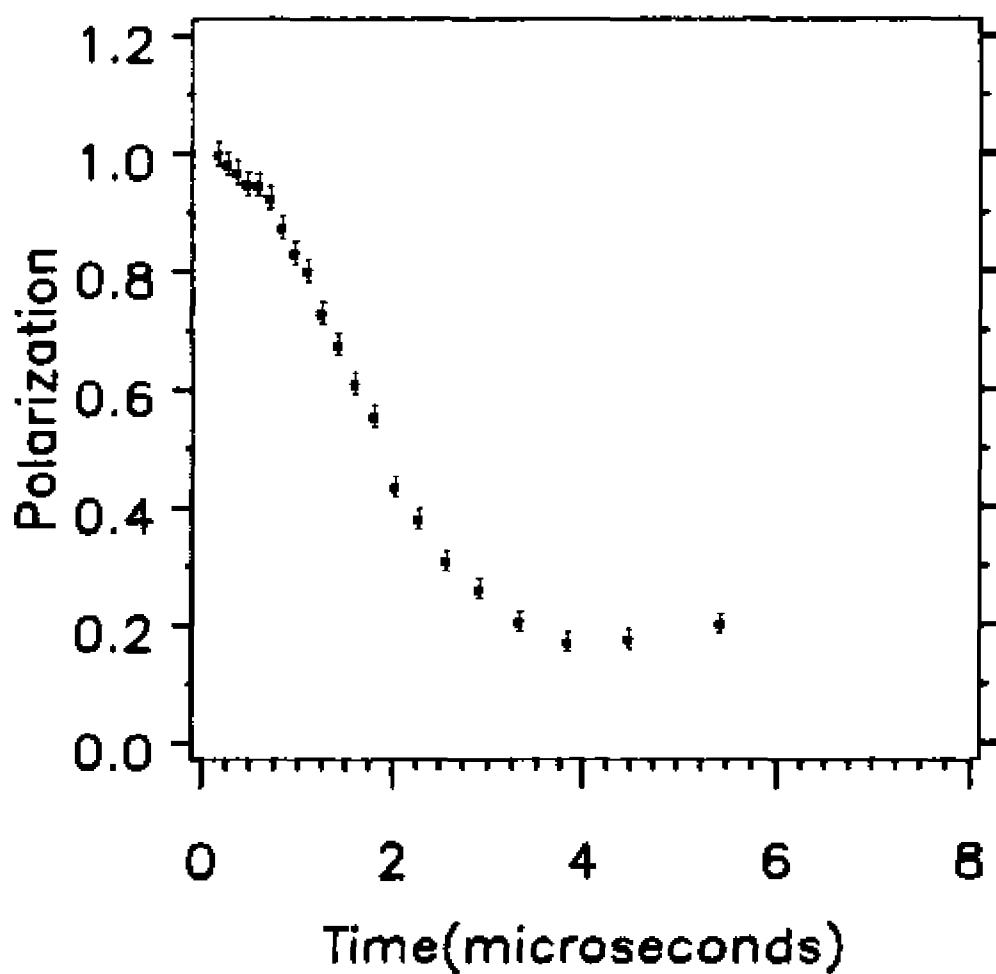


Figure 7.15c  
Experimentally-determined zero-field muon polarization as  
a function of time for  $\text{TiH}_{1.83}$  at 100 K.

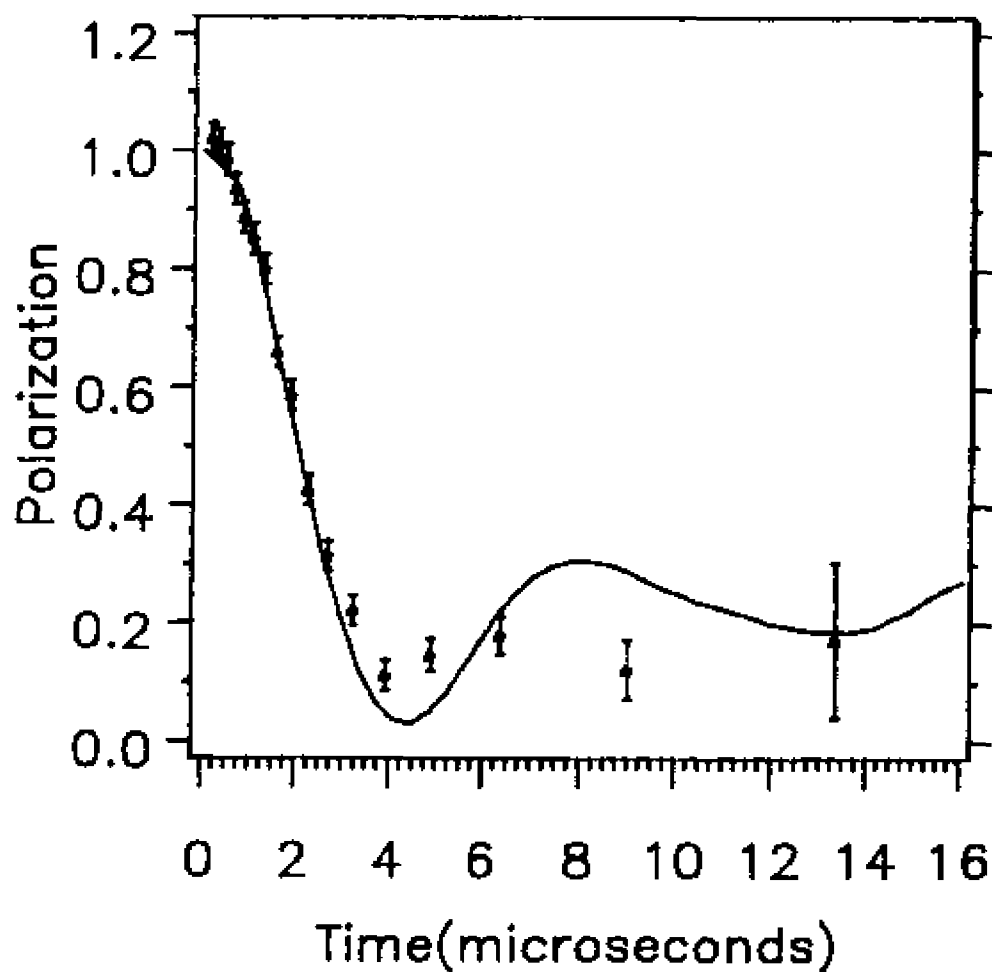


Figure 7.15d

Experimentally-determined zero-field muon polarization as a function of time for  $\text{TiH}_{1.83}$  at 305 K. The curve is a theoretical calculation of the relaxation function for a muon in an tetrahedral site (see Appendix D).<sup>61</sup>

compare this calculation with the  $x=1.83$  case since almost 70% of the muons are in tetrahedral sites. This is evidenced by the filling in and shift of the minimum and the damping of the recovery hump.

Since the position of the minimum in time of the relaxation function is independent of model (Fig. 5.5), the time derivative of Eqn. 5.32 can be used to calculate the zero-field depolarization rate,  $\Delta_2$ .

$$G_2(t) = 1/3 + 2/3(1 - \Delta_2^2 t^2) \exp(-\Delta_2^2 t^2 / 2). \quad (5.32)$$

The minimum of this function occurs at  $\Delta t = \sqrt{3}$ . The depolarization rate, thus, equals  $\sqrt{3}/t_{\min}$ .

The zero-field depolarization rate,  $\Delta_{Zcal}$ , can be calculated using a form similar to Eqn. 7.3.

$$\Delta_{Zcal}^2 = \Delta_{TET}^2 P + \Delta_{OCT}^2 (1-P), \quad (7.21a)$$

$$P = 8(1-x/2) \quad (7.21b)$$

The zero-field depolarization rate for a muon occupying a tetrahedral site (octahedral) site is equal to  $\Delta_{TET}$  ( $\Delta_{OCT}$ ), which was obtained in section 7.1A.1, multiplied by  $\sqrt{5}$  yielding a value of  $0.385(11) \mu s^{-1}$  ( $0.563(7) \mu s^{-1}$ ). Table 7.9 shows the results of both calculations of the zero-field depolarization rate for all three hydrogen concentrations.



Table 7.9

$t_{\min}$ , the zero-field depolarization rate, and the calculated zero-field depolarization rate as a function of hydrogen concentration in titanium hydride at 100 K.

x	$t_{\min}(\mu\text{s})$	$\Delta_z(\mu\text{s}^{-1})$	$\Delta_{z\text{cal}}(\mu\text{s}^{-1})$
1.99	3.2(1)	0.54(2)	0.557(7)
1.97	3.3(1)	0.52(2)	0.545(7)
1.83	4.1(1)	0.42(1)	0.450(9)

The agreement between the calculated and the measured zero-field depolarization rates is good.

The spin-spin relaxation time for a nearest-neighbor proton can be estimated from the zero-field  $\mu\text{SR}$  data.<sup>50</sup> Using the curves of Fig. 5.4b, the value of  $\Delta\tau$  for  $x=1.99$  is estimated to be approximately 4. If  $\Delta=0.54 \mu\text{s}^{-1}$ , then  $\tau \sim 7.5 \mu\text{s}$  and is the field-correlation time due the dynamics of the proton spins.

The calculation of the proton second moment in zero-field involves calculating the second derivative of the relaxation function using a dipolar Hamiltonian (Appendix E). The second moment for a nearest-neighbor proton contains contributions from the lattice of hydrogen atoms and the nearest-neighbor muon. The muon in this case is an interstitial in a SC lattice. The second moment is calculated to be  $0.103 \mu\text{s}^{-2}$ . If the line width is Gaussian,

then the spin-spin relaxation time is  $4.4 \mu\text{s}$ . This result is within a factor of two of the estimated result from the zero-field experiment. The agreement is surprisingly good despite the lack of coupling between the muon and the lattice of protons.

Fig. 7.15d shows the results for  $\text{TiH}_{1.83}$  at 305 K. This temperature was chosen because the transverse-field results indicate that the muon is trapped in a T site (Fig. 7.6). Once again, the polarization shows oscillations at long times which is not characteristic of Kubo-Toyabe depolarization function for a static muon. A calculation of the polarization for a muon in a substitutional site of a SC lattice was performed.<sup>61</sup> This calculation was similar to the one for an interstitial muon in a SC lattice with the exception that there were six nearest-neighbor hydrogen atoms. The calculated muon polarization is shown in Fig. 7.15d (Appendix D). This calculation fits the experimentally measured polarization better than Kubo-Toyabe theory for a static muon. The discrepancy between the calculated and measured polarizations may be due to the lack of proton-proton coupling which could not be included in these calculations.

The minimum in the polarization occurs at  $4.3(1) \mu\text{s}$ . This corresponds to a zero-field depolarization rate of  $0.403(9) \mu\text{s}^{-1}$ . The calculated zero-field depolarization rate for a muon in a T site is  $0.385(11) \mu\text{s}^{-1}$ . The agree-

ment between these two is good and helps confirm that the muon is in a T site.

The calculation of the proton spin-spin relaxation time with a muon in a T site is similar to that for a muon in an O site. The major difference is that the contribution of the muon to the second moment will be smaller since it is farther away from the proton. The calculated second moment is  $0.0714 \mu\text{s}^{-2}$ . If the line width is Gaussian, then the spin-spin relaxation time is  $5.3 \mu\text{s}$ . Using the curves in Fig. 5.4b, the estimated value for  $\Delta\tau$  for the muon polarization in Fig. 7.15d is approximately 2. Since  $\Delta = 0.40 \mu\text{s}^{-1}$ , then  $\tau \approx 5 \mu\text{s}$ . This is in good agreement with the calculated spin-spin relaxation time of  $5.3 \mu\text{s}$ .

#### B. Yttrium Hydride

Fig. 7.16a-b shows the zero-field muon polarization for  $\text{YH}_2$  at 20 K and 295 K. Since the polarization was not measured at long times, the comparison to the calculated polarization and the calculation of the proton spin-spin relaxation time (as was done for  $\text{TiH}_x$ ) is not possible. The line widths obtained from zero-field ( $\Delta_x = \Delta_z/\sqrt{5}$ ) and transverse-field studies ( $\Delta_{xt}$ ) can be compared (Table 7.10). The agreement between the two techniques is good, but experiments should be performed with an emphasis on long-time behavior of  $G_z(t)$ .

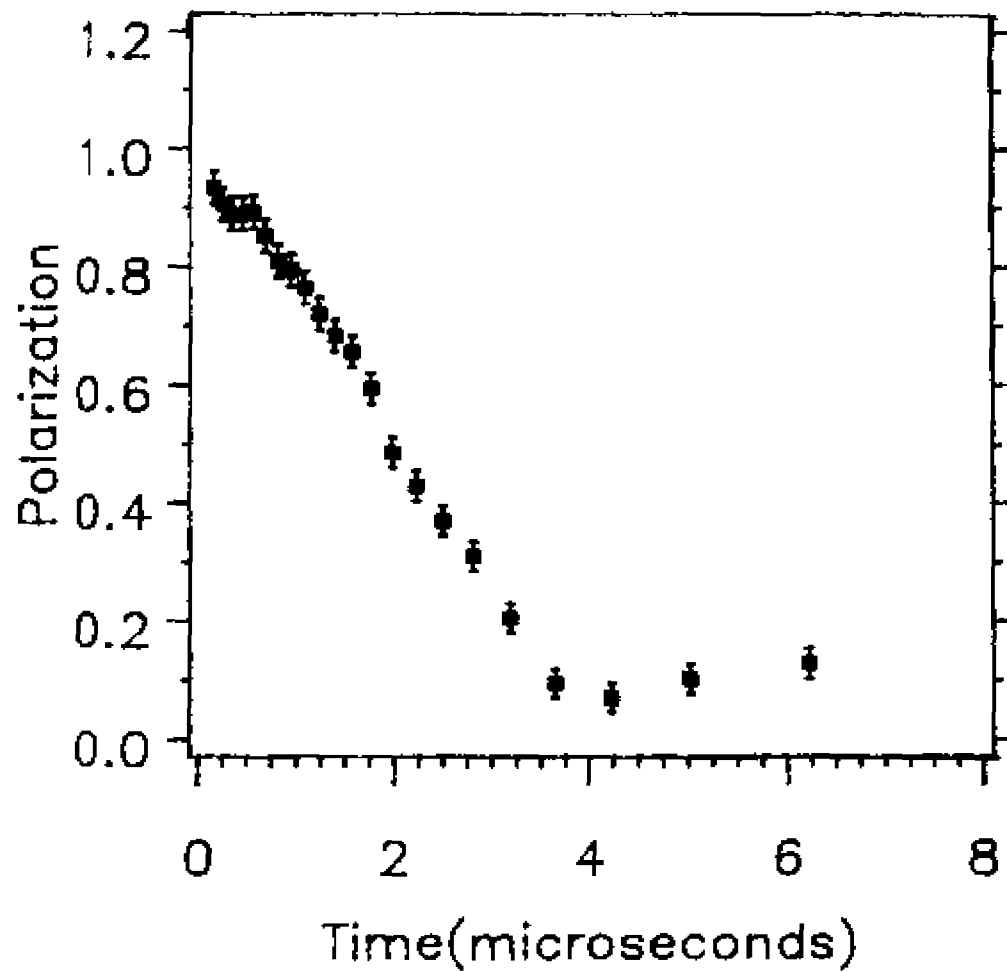


Figure 7.16a  
Experimentally-determined zero-field muon polarization as  
a function of time for  $\text{YH}_2$  at 20 K.

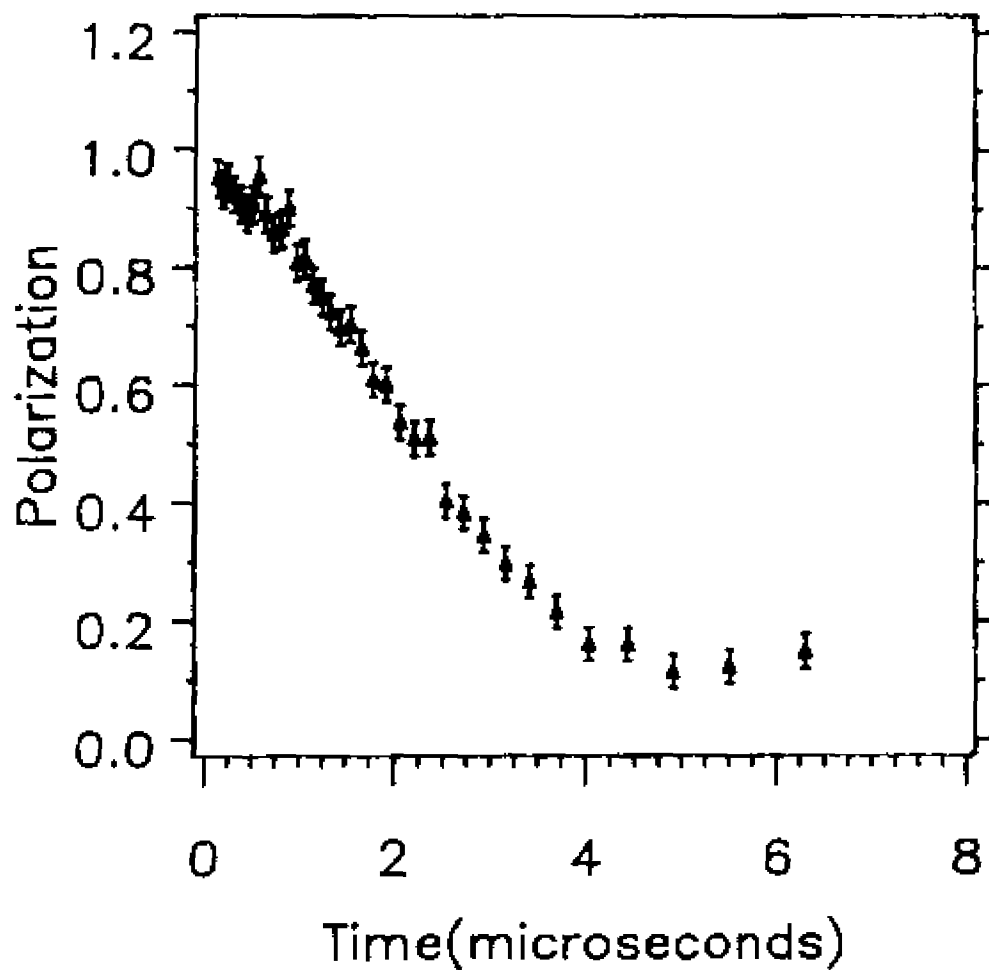


Figure 7.16b  
Experimentally-determined zero-field muon polarization as  
a function of time for  $\text{YH}_2$  at and 295 K.

Table 7.10

$t_{\min}$ , the zero-field depolarization rate, calculated transverse-field line width from zero-field depolarization rate, and experimentally measured transverse-field line width as a function of temperature in yttrium hydride.

T(K)	$t_{\min}(\mu\text{s})$	$\Delta_z(\mu\text{s}^{-1})$	$\Lambda_x(\mu\text{s}^{-1})$	$\Lambda_{xt}(\mu\text{s}^{-1})$
20	4.2(1)	0.41(1)	0.184(4)	0.170(5)
295	5.2(1)	0.33(1)	0.149(3)	0.149(6)

### 7.3 LONGITUDINAL-FIELD STUDIES

The longitudinal-field  $\mu\text{SR}$  technique was applied to the  $\text{TiH}_{1.97}$  sample at 100 K and approximately eight gauss. Fig. 7.17 shows the muon polarization for this field and indicates that the fluctuation rate for internal fields is less than 100 KHz (Fig. 5.7). The solid line is a fit of the data to Eqn. 5.40 out to approximately four microseconds since the decay of the muon polarization is an indication of a finite field-correlation time (due to the spin dynamics of the proton). The frequency obtained from the fit,  $\omega=0.673(2)$  MHz, corresponds to a field of 7.9 G which is in agreement with the known value of the applied field. The value for the depolarization rate obtained from the fit,  $\Delta_z=0.48(2) \mu\text{s}^{-1}$ , is in agreement with the value reported in Table 7.9 of  $0.52(2) \mu\text{s}^{-1}$ . As was the case in

zero-field, Kubo-Toyabe theory for a static muon fails to describe the data at long time. For long times, the decrease in the polarization can be described by  $\exp(-t/\tau)$ . This decay time has been estimated to be of the order of ten microseconds. This yields a value of  $\Delta\tau$  on the order of 5 which agrees with the estimate from the zero-field data for  $\text{TiH}_{1.99}$  of  $\Delta\tau \approx 4$ .

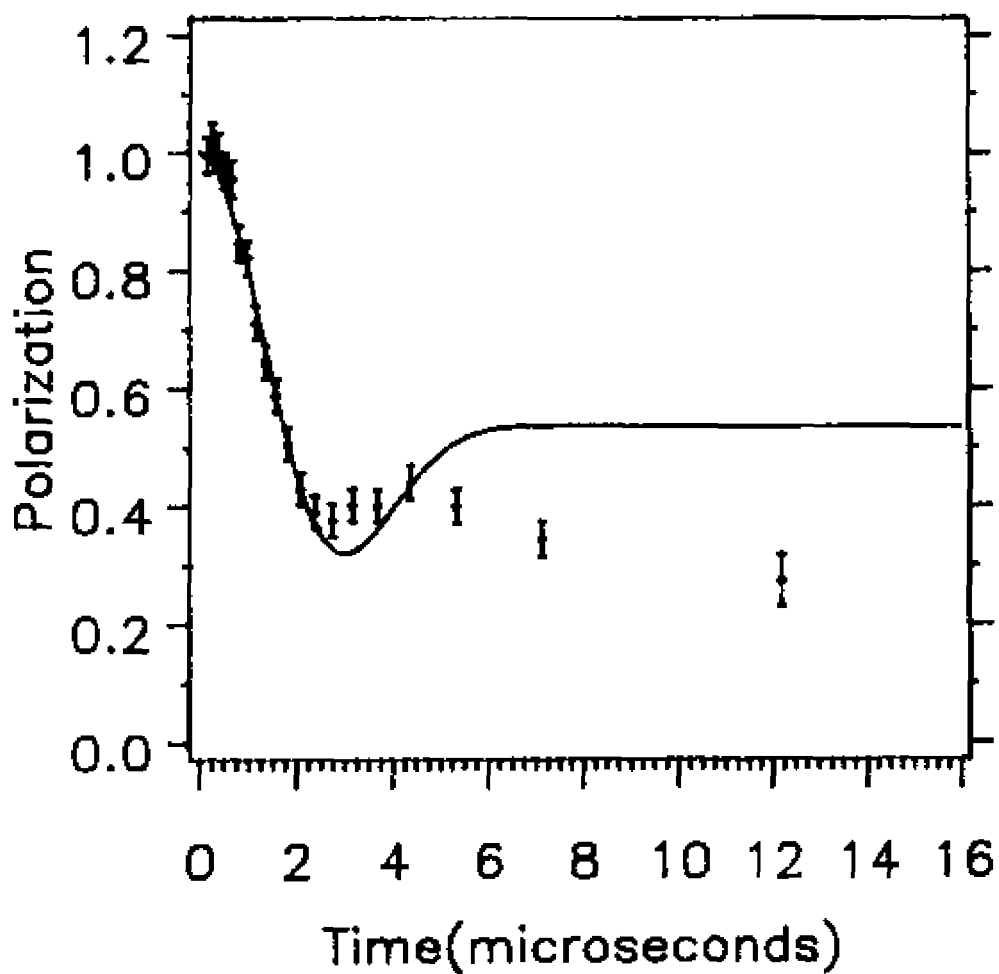


Figure 7.17  
Experimentally-determined longitudinal-field muon polarization as a function of time for  $\text{TiH}_{1.97}$  at 100 K and 7.9 G. The curve is a least squares fit out to four microseconds to Eqn. 5.40.



## CONCLUSION

The spin dynamics of protons have been seen to have a significant effect upon the fields felt by the muon. This was observed in the oscillation of the zero- and low longitudinal-field muon polarizations at long times with a damping due to the dynamics of the proton spins. Secondly, the narrowing of the transverse-field gaussian line widths by approximately 5% is evidence of the significance of the proton spin-spin interactions.

The diffusion and sites of muons in titanium hydride are dependent upon hydrogen concentration and temperature. For low temperatures and high hydrogen concentrations, the majority of the muons occupy octahedral sites with the probability for T-site occupancy equal to the probability that any of the nearest-neighbor tetrahedral sites to an O site are vacant. For low vacancy concentrations ( $x=1.97$  and  $1.99$ ), the O-site muons activate out of these sites (activation energy and prefactor equal to  $0.48(8)$  eV and  $10^{13}(1)\text{s}^{-1}$ , respectively) indicating that the vibration of the hydrogen lattice is responsible for this process. For higher vacancy concentrations ( $x=1.83$ ), an attractive force between the muon and vacancies at second-nearest-neighbor sites enables these vacancies to move to the

nearest-neighbor sites and allow the muon to jump to the T site. This force arises from the 6(1)% local hydrogen lattice dilation around the O-site muon. Near room temperature the muon occupies a tetrahedral site and distorts the hydrogen lattice by 3(1)%. At high temperatures (~500 K), the muon field-correlation time is greater than the proton diffusion time. Monte Carlo simulations indicate that the field-correlation time for a stationary muon equals the proton diffusion time. Therefore, the nearest-neighbor hydrogen atoms must be bound to their sites to increase the muon field-correlation time to explain the data. The usual binding mechanism is to increase their activation energy. However, the results from a fit to an Arrhenius expression to the field-correlation time show a decreased activation energy. In an attempt to explain this disagreement, the muon is postulated to tunnel to a second-nearest-neighbor site with the nearest-neighbor hydrogen atoms bound to their sites. However, the values for the tunneling matrix element and the distortion of the nearest-neighbor titanium atoms are too large. The discovery from the Monte Carlo simulations that the field-correlation time for a stationary muon is less than that measured in the experiments is significant. The study of a few more compounds, such as  $TiH_{1.7}$  and  $TiH_{1.9}$ , would be beneficial to the development of a model to explain the high temperature muon field-correlation times.

The results of  $\mu$ SR studies of yttrium hydride are qualitatively similar to those of titanium hydride. This is evidenced by the low prefactor and activation energy for the muon field-correlation time as compared to the proton diffusion time at high temperatures. Secondly, the muon occupies tetrahedral sites near room temperature and predominately O sites below room temperature. However, one striking difference between the results for titanium and yttrium hydrides is that the probability for muon T-site occupancy increases with hydrogen concentration for  $YH_x$ . This is thought to be due to an increase in the number of protons occupying O sites as H/Y approaches two. Secondly, no dilation of the local hydrogen lattice is observed. Future work on other yttrium hydride compounds should initially be confined to the high temperature regime to confirm the similarities in results to those of titanium hydride. Secondly, a study of the muon depolarization rate below room temperature should be conducted to observe in more detail the percentage of octahedral site protons as a function of hydrogen concentration.

The results of  $\mu$ SR studies of zirconium hydride agree qualitatively with the previous results of Doyama et al.<sup>33</sup> (and with those of  $TiH_x$ ). As for  $TiH_x$ , the muon predominately occupies octahedral sites with a trapping radius that includes the eight nearest-neighbor T sites. Further work on other zirconium hydride compounds is necessary to lower the uncertainty in the calculated local lattice

dilation due to a muon in an octahedral site. Secondly, studies to complement those of Doyama et al.<sup>33</sup>, combined with those for titanium hydride, would contribute to the development of a model to explain the high temperature muon field-correlation time.

The results of  $\mu$ SR studies of lanthanum hydride indicate that the muon is stationary. This is evidenced by the lack of a minima in the depolarization rate as a function of temperature as was seen for  $TiH_{1.99}$ . The muon site is probably an octahedral site since the tetrahedral sites are occupied by protons. However, a study of the depolarization rate as a function of applied magnetic field would substantiate this hypothesis.

## APPENDIX A

### COMPUTER PROGRAM FOR SIMULATION OF MOTION ON A CUBIC LATTICE

```
C
C PROGRAM TO WATCH THE MOVEMENT OF 7 VACANCIES IN A
C LATTICE OF 729 LOCATIONS AND THEIR EFFECT UPON
C THE MAGNETIC FIELD FELT BY THE MUON. THE MUON
C STARTS AT (0,0,0) WITH INDUCED PROBABILITIES
C FOR NN AND NEXT NN MOVEMENT
C
C USING THE IMSL SUBROUTINE GGUBS AND FUNCTION
C ROUTINE GGUBFS TO GENERATE RANDOM NUMBERS. BOTH
C OF THESE ARE PSEUDO-RANDOM NUMBER GENERATORS
C
C
C SPIN(X,Y,Z,N) IS THE COMPONENT OF THE SPIN AT
C LATTICE POSITION (X,Y,Z) IN THE X(N=1), Y(N=2),
C AND Z(N=3) DIRECTION
C
C IV(N,M) IS THE ARRAY WHICH STORES THE POSITION OF
C THE VACANCIES.
C N LABELS THE VACANCY AND M DEFINES THE LATTICE
C LOCATION; X(M=1) ,Y(M=2) , Z(M=3) .
C
C NTRY(N) IS THE ARRAY WHICH KEEPS TRACK OF THE
C DIRECTIONS A VACANCY HAS ATTEMPTED. IF A VACANCY
C CANNOT MOVE IN A PARTICULAR DIRECTION, THEN THE
C VALUE IN THE ARRAY ASSOCIATED WITH THAT DIRECTION
C IS SET=1. IF ALL VALUES IN THE ARRAY ARE 1 THEN
C THE VACANCY CANNOT MOVE.
C
C NN(N,M) DEFINES THE NEAREST NEIGHBORS(N=1 TO 6)
C AND THEIR POSITIONS (M=1 TO 3) .
C
C MARK(X,Y,Z) IS THE ARRAY WHICH KEEPS TRACK OF
C WHICH LATTICE LOCATIONS HAVE BEEN THE SIGHT OF
C MOVEMENTS
C
C MPOS(3) IS THE ARRAY WHICH KEEPS TRACK OF THE
C MUON'S POSITION.
C
C ARRAY(3) IS THE ARRAY WHICH IS USED FOR THE RANDOM
C NUMBER GENERATOR.
C
C B AND BN ARE THE MAGNETIC FIELD IN THREE
```

```

C DIRECTIONS DUE TO THE NUCLEAR SPINS.
C
C BX IS THE UNIT VECTOR IN THREE DIRECTIONS OF THE
C EXTERNAL MAGNETIC FIELD.
C
C NCHECK(0:3000,7) IS THE ARRAY WHICH KEEPS TRACK OF
C WHICH VACANCY IS A NEAREST NEIGHBOR OF THE MUON
C
C CLOCK IS A SUBROUTINE IN THE VFORTLIB WHICH READS
C THE TIME OF DAY IN UNITS OF 1/300 SECOND AND
C RETURNS IT AS A INTEGER*4 VARIABLE.
C
C VZERO(ARRAY,NO.OF ELEMENTS) IS A SUBROUTINE WHICH
C ZEROS THE NO. OF ELEMENTS IN AN ARRAY ASSUMING IT
C IS AN INTEGER*4 OR REAL*4 ARRAY.
C
COMMON /S/SPIN(-4:4,-4:4,-4:4,3)
COMMON /MUON/MPOS(3)
INTEGER IV(7,3),NTRY(6),NN(6,3),
1 MARK(-4:4,-4:4,-4:4),IVAC(7,2),NNVAC(7)
REAL ARRAY(3),BX(3),B(3),BN(3)
INTEGER*2 NCHECK(0:3000,7)
REAL*8 DSEED
DATA P,MNN,MMPOS,MNPOS1,MNPOS2,
1 MNPOS3/0.33,5*0/
DATA NN/1,-1,6*0,1,-1,6*0,1,-1/
DATA NCHECK/21007*0/
C SET THE VALUE FOR PPRIME
PPRIME=0.0
C SET THE VALUE FOR PIN
PIN=1./18.
C SET THE VALUE FOR POUT
POUT=1./1800.
C SET THE VALUE FOR P
P=1./18.
C READ TIME TO SEED THE RANDOM NUMBER GENERATOR
CALL CLOCK(ITIME)
WRITE(6,1000) ITIME
1000 FORMAT(1X,'TIME OF DAY FOR SEED=',I10)
DSEED=DFLOAT(ITIME)
CALL VZERO(MPOS,3)
C PICK THETA AND PHI TO DETERMINE THE FIELD
C DIRECTION THETA IS CHOSEN PROBABILITY OF THETA
C NEAR PI/2 LARGER
CALL GGUBS(DSEED,3,ARRAY)
PI=2.0*ACOS(0.0)
TH=1.0-ARRAY(1)
THETA=ACOS(TH)
C IF ARRAY(3) > 0.5 THEN THETA WILL RUN FROM PI/2 TO
C PI
IF(ARRAY(3).GT.0.5) THEN
THETA=PI-THETA
ENDIF
ENDIF

```

```

      PHI=ARRAY(2)*2.*PI
C CALCULATE THE FIELD DIRECTION
      X=SIN(THETA)*COS(PHI)
      Y=SIN(THETA)*SIN(PHI)
      Z=COS(THETA)
      BX(1)=X
      BX(2)=Y
      BX(3)=Z
      WRITE(6,1001) X,Y,Z
1001 FORMAT(1X,'FIELD DIRECTION=(',
      1 2(F7.4,' '),F7.4,')')
C PICK SPINS FOR EACH LATTICE POINT EXCEPT FOR THE
C MUON.
      DO 100 I=-4,4
      DO 101 J=-4,4
      DO 102 K=-4,4
      IF(I.EQ.0.AND.J.EQ.0.AND.K.EQ.0) THEN
          GOTO 102
      ENDIF
C QUANTIZE THE SPINS OF THE PROTONS PARALLEL OR
C ANTIPARALLEL TO THE APPLIED MAGNETIC FIELD
      CALL GGUBS(DSEED,1,ARR)
      IF(ARR.GT.0.5) THEN
          SPIN(I,J,K,1)=X
          SPIN(I,J,K,2)=Y
          SPIN(I,J,K,3)=Z
      ELSE
          SPIN(I,J,K,1)=-X
          SPIN(I,J,K,2)=-Y
          SPIN(I,J,K,3)=-Z
      ENDIF
102 CONTINUE
101 CONTINUE
100 CONTINUE
      WRITE(6,1002)
1002 FORMAT(18X,'INITIAL')
      WRITE(6,1003)
1003 FORMAT(1X,'VACANCY NO.',1X,'LOCATION(X,Y,Z)')
C PICK LOCATION OF THE 7 VACANCIES
      DO 103 I=1,7
10  CALL GGUBS(DSEED,3,ARRAY)
      DO 104 J=1,3
          JV1=9.0*ARRAY(J)
          IV(I,J)=JV1-4
      104 CONTINUE
C CHECK TO SEE WHETHER THE VACANCY IS AT THE MUON'S
C INITIAL LOCATION, IF SO GO BACK AND PICK A NEW
C LOCATION
      IF(IV(I,1).EQ.0.AND.IV(I,2).EQ.0
      1 .AND.IV(I,3).EQ.0) GOTO 10
C IF I=1 THEN THE DO LOOP WITH VARIABLE K WILL HAVE
C A PROBLEM WITH DO 105 K=1,0; THEREFORE SKIP OVER
C THIS DO LOOP

```

```

      IF(I.EQ.1) GOTO 11
C CHECK TO SEE WHETHER THERE ARE TWO VACANCIES AT
C ONE SPOT
      DO 105 K=1,I-1
      IF(IV(I,1).EQ.IV(K,1).AND.IV(I,2).EQ.IV(K,2)
1 .AND.IV(I,3).EQ.IV(K,3)) THEN
          GOTO 10
      ENDIF
105 CONTINUE
C SET SPIN OF VACANCY=0 IN ALL 3 DIRECTIONS
11 DO 106 K=1,3
      SPIN(IV(I,1),IV(I,2),IV(I,3),K)=0.0
106 CONTINUE
C WRITE INITIAL LOCATION OF VACANCIES
      WRITE(6,1004) I,(IV(I,J),J=1,3)
1004 FORMAT(2X,I4,9X,3(I4))
      DO 107 LP=1,6
C CHECK TO SEE WHETHER ANY OF THE VACANCIES ARE
C MUON'S NN
      IF(IV(I,1).EQ.NN(LP,1).AND.IV(I,2).EQ.NN(LP,2)
1 .AND.IV(I,3).EQ.NN(LP,3)) THEN
          MNN=MNN+1
          NCHECK(0,I)=1
          WRITE(6,1005)
1005 FORMAT('+',28X,' IS A NN OF THE MUON')
      ENDIF
107 CONTINUE
103 CONTINUE
C CALCULATE THE DIPOLAR MAGNETIC FIELD INDUCED BY
C THE NEIGHBORING PROTONS
      CALL BCAL(B)
      BOB=B(1)*BX(1)+B(2)*BX(2)+B(3)*BX(3)
C BOB= DOT PRODUCT OF THE MAGNETIC FIELD WITH THE
C UNIT VECTOR OF THE EXTERNAL MAGNETIC FIELD
C START TO LET VACANCIES MOVE
      FC=1.0
      I=0
      WRITE(2,1016) BOB,FC,I,MNN
      DO 108 I=1,3000
C SET ALL STORAGE SPACES IN THE ARRAY WHICH KEEPS
C TRACK OF WHAT LATTICE SITES HAVE MOVED DURING ITH
C TIME INTERVAL TO ZERO
      CALL VZERO(MARK,729)
C SET THE MARKER WHICH KEEPS TRACK OF WHETHER A
C VACANCY IS A NEXT NEAREST NEIGHBOR TO THE MUON TO
C ZERO FOR THE ITH TIME INTERVAL
      CALL VZERO(IVAC,14)
C SET THE MARKER WHICH KEEPS TRACK OF WHETHER A
C VACANCY IS A NEAREST NEIGHBOR TO THE MUON TO
C ZERO FOR THE ITH TIME INTERVAL.
      CALL VZERO(NNVAC,7)
C SET THE MARKER FOR THE VACANCIES SO THAT THERE ARE
C NO VACANCY-VACANCY SWITCHES

```



```

        DO 115 IK=1,7
        MARK(IV(IK,1),IV(IK,2),IV(IK,3))=1
115    CONTINUE
        DO 109 J=1,7
C     JX, JY, JZ ARE TEMPORARY SPOTS TO STORE THE
C     ORIGINAL SITE OF THE VACANCY; JX STORES X
C     COMPONENT; JY STORES Y; JZ STORES Z
        JX=IV(J,1)
        JY=IV(J,2)
        JZ=IV(J,3)
C     SET ALL STORAGE SPOTS OF THE ARRAY WHICH KEEPS
C     TRACK OF THE DIRECTIONS WHICH A VACANCY HAS
C     ATTEMPTED TO MOVE TO ZERO
        CALL VZERO(NTRY,6)
C     J1 IS THE INDEX USED IN ARRAY IVAC TO DEFINE
C     WHETHER THE VACANCY HAS ONE OR TWO MUON NEAR
C     NEIGHBOR SITES NEXT TO IT.
        J1=1
C     STEP THROUGH THE MUON NEAR NEIGHBORS TO FIND THE
C     DISTANCE TO THE VACANCY.
        DO 118 J2=1,6
C     STEP THROUGH THE THREE DIRECTIONS OR ARRAY
C     POSITIONS OF EACH NN
        R2=0.0
        DO 119 J3=1,3
C     CALCULATE THE DISTANCE BETWEEN THE J2TH NN AND THE
C     JTH VACANCY
        R2=R2+(NN(J2,J3)-IV(J,J3))**2
119    CONTINUE
C     IF THE VACANCY IS A MUON NEAREST NEIGHBOR THEN
C     NOTE WHICH ONE IT IS BECAUSE THIS WILL INFLUENCE
C     WHICH DIRECTION IT MOVES.
        IF(R2.EQ.0.) THEN
            NNVAC(J)=J2
C     IF THE VACANCY IS NEXT TO A MUON NN THEN NOTE
C     WHICH NN IT IS NEXT TO (BECAUSE THIS WILL BE USED
C     IN DETERMINING HOW IT MOVES) AND THEN INCREMENT
C     THE INDEX AND CHECK THE REMAINING MUON NN
        ELSE IF(R2.EQ.1.0) THEN
            IVAC(J,J1)=J2
            J1=J1+1
        ENDIF
118    CONTINUE
C     PICK A RANDOM NUMBER WHICH WILL BE USED TO DECIDE
C     WHICH DIRECTION THE VACANCY WILL BE ALLOWED TO
C     MOVE.
12     RND=GGUBFS(DSEED)
C     IF STATEMENT CHECKS TO SEE WHETHER THE VACANCY IS
C     A MUON NN
        IF(NNVAC(J).NE.0) THEN
C     IF RND IS GREATER THEN P'+5*POUT THEN GOTO THE
C     NEXT VACANCY
        IF(RND.GE.(PPRIME+5.*POUT)) GOTO 109

```

```

C IF THE RANDOM NUMBER IS LESS THAN PPRIME THEN THE
C MUON AND VACANCY WILL EXCHANGE POSITIONS.
      IF(RND.LT.PPRIME) THEN
          MLOC=NNVAC(J)
          GOTO (1,2,3,4,5,6),MLOC
      ELSE
C IF THE RANDOM NUMBER IS GREATER THAN PPRIME THEN
C PICK ANOTHER DIRECTION TO MOVE WITH SOME REDUCED
C PROBABILITY
          MLOC=(RND-PPRIME)/POUT+1
          IF(NNVAC(J).EQ.1) GOTO 71
          IF(NNVAC(J).EQ.2) GOTO 72
          IF(NNVAC(J).EQ.3) GOTO 73
          IF(NNVAC(J).EQ.4) GOTO 74
          IF(NNVAC(J).EQ.5) GOTO 75
          IF(NNVAC(J).EQ.6) GOTO 76
      ENDIF
C IF THE VACANCY IS NOT A NEXT NEAREST NEIGHBOR OR A
C NEAREST NEIGHBOR OF THE MUON THEN THE PROBABILITY
C OF MOVING IN ANY OF THE SIX DIRECTIONS IS EQUALLY
C LIKELY.
      ELSE IF(NNVAC(J).EQ.0.AND.IVAC(J,1).EQ.0) THEN
C IF RND IS GREATER THEN 6*P THEN GOTO THE NEXT
C VACANCY
          IF(RND.GE.(6.*P)) GOTO 109
          MLOC=RND/P+1
          GOTO(1,2,3,4,5,6),MLOC
C IF THE VACANCY HAS ONLY ONE MUON NN AS A NEIGHBOR
C THEN INCREASE THE PROBABILITY OF MOVING IN THAT
C DIRECTION TO PIN
          ELSE IF(IVAC(J,1).NE.0.AND.IVAC(J,2).EQ.0)
              1 THEN
C IF THE RANDOM NUMBER IS GREATER THEN PIN+5*P THEN
C GOTO NEXT VACANCY
          IF(RND.GE.(PIN+5.*P)) GOTO 109
          IF(RND.LT.PIN) THEN
              MLOC=IVAC(J,1)
              GOTO(1,2,3,4,5,6),MLOC
          ELSE
C IF THE RANDOM NUMBER IS GREATER THAN PIN THEN
C ALLOW MOVEMENT IN ONE OF THE OTHER FIVE
C DIRECTIONS WITH A REDUCED PROBABILITY
              MLOC=(RND-PIN)/P+1
              IF(IVAC(J,1).EQ.1) GOTO 71
              IF(IVAC(J,1).EQ.2) GOTO 72
              IF(IVAC(J,1).EQ.3) GOTO 73
              IF(IVAC(J,1).EQ.4) GOTO 74
              IF(IVAC(J,1).EQ.5) GOTO 75
              IF(IVAC(J,1).EQ.6) GOTO 76
          ENDIF
C IF THE VACANCY HAS TWO NEIGHBORS WHICH ARE MUON NN
C THEN INCREASE THE PROBABILITY OF MOVING TO ONE OF
C THESE TWO.

```

```

ELSE IF(IVAC(J,1).NE.0.AND.IVAC(J,2).NE.0)
  1 THEN
C IF THE RANDOM NUMBER IS GREATER THAN 2PIN+4P THEN
C GOTO NEXT VACANCY
  IF(RND.GE.(2.*PIN+4.*P)) GOTO 109
  IF(RND.LT.PIN) THEN
    MLOC=IVAC(J,1)
    GOTO(1,2,3,4,5,6),MLOC
  ELSE IF(RND.LT.(2.0*PIN)) THEN
    MLOC=IVAC(J,2)
    GOTO(1,2,3,4,5,6),MLOC
  ELSE
C IF THE RANDOM NUMBER>2*PIN THEN ALLOW MOTION TO
C ONE OF THE FOUR OTHER SITES WITH A REDUCED
C PROBABILITY
    MLOC=(RND-2.*PIN)/P+1
    IF(IVAC(J,1).EQ.1.AND.IVAC(J,2).EQ.3) THEN
      GOTO(2,4,5,6),MLOC
    ELSE IF(IVAC(J,1).EQ.1.AND.IVAC(J,2).EQ.4) THEN
      GOTO(2,3,5,6),MLOC
    ELSE IF(IVAC(J,1).EQ.1.AND.IVAC(J,2).EQ.5) THEN
      GOTO(2,3,4,6),MLOC
    ELSE IF(IVAC(J,1).EQ.1.AND.IVAC(J,2).EQ.6) THEN
      GOTO(2,3,4,5),MLOC
    ELSE IF(IVAC(J,1).EQ.2.AND.IVAC(J,2).EQ.3) THEN
      GOTO(1,4,5,6),MLOC
    ELSE IF(IVAC(J,1).EQ.2.AND.IVAC(J,2).EQ.4) THEN
      GOTO(1,3,5,6),MLOC
    ELSE IF(IVAC(J,1).EQ.2.AND.IVAC(J,2).EQ.5) THEN
      GOTO(1,3,4,6),MLOC
    ELSE IF(IVAC(J,1).EQ.2.AND.IVAC(J,2).EQ.6) THEN
      GOTO(1,3,4,5),MLOC
    ELSE IF(IVAC(J,1).EQ.3.AND.IVAC(J,2).EQ.5) THEN
      GOTO(1,2,4,6),MLOC
    ELSE IF(IVAC(J,1).EQ.3.AND.IVAC(J,2).EQ.6) THEN
      GOTO(1,2,4,5),MLOC
    ELSE IF(IVAC(J,1).EQ.4.AND.IVAC(J,2).EQ.5) THEN
      GOTO(1,2,3,6),MLOC
    ELSE IF(IVAC(J,1).EQ.4.AND.IVAC(J,2).EQ.6) THEN
      GOTO(1,2,3,5),MLOC
    ELSE
      WRITE(6,6000) IVAC(J,1),IVAC(J,2)
6000 FORMAT(//,1X,'WRONG WAY',2(1X,I3),//)
      ENDIF
    ENDIF
  ENDIF
  ENDIF
71 GOTO(2,3,4,5,6),MLOC
72 GOTO(1,3,4,5,6),MLOC
73 GOTO(1,2,4,5,6),MLOC
74 GOTO(1,2,3,5,6),MLOC
75 GOTO(1,2,3,4,6),MLOC
76 GOTO(1,2,3,4,5),MLOC
C PICK DIRECTION WHICH THE VACANCY WILL ATTEMPT TO

```

```

C MOVE IF MLOC=1 MOVE IN -X DIRECTION; =2 MOVE IN
C +X; =3 MOVE IN -Y; =4 MOVE IN +Y; =5 MOVE IN -Z;
C =6 MOVE IN +Z; MLOC MUST < 7
C MOVE IN THE - X DIRECTION
  1  IV(J,1)=IV(J,1)-1
     NTRY(1)=1
C SET NTRY(MLOC)=1 TO SHOW THAT DIRECTION HAS BEEN
C TRIED IF THE VACANCY HAS MOVED OUT TOO FAR BRING
C IT AROUND TO THE OTHER SIDE
     IVA=ABS(IV(J,1))
     IF(IVA.EQ.5) THEN
       IV(J,1)=-JX
     ENDIF
     GOTO 16
C MOVE IN THE + X DIRECTION
  2  IV(J,1)=IV(J,1)+1
     NTRY(2)=1
C IF THE VACANCY HAS MOVED OUT TOO FAR BRING IT
C AROUND TO THE OTHER SIDE
     IVA=ABS(IV(J,1))
     IF(IVA.EQ.5) THEN
       IV(J,1)=-JX
     ENDIF
     GOTO 16
C MOVE IN THE - Y DIRECTION
  3  IV(J,2)=IV(J,2)-1
     NTRY(3)=1
     IVA=ABS(IV(J,2))
     IF(IVA.EQ.5) THEN
       IV(J,2)=-JY
     ENDIF
     GOTO 16
C MOVE IN THE + Y DIRECTION
  4  IV(J,2)=IV(J,2)+1
     NTRY(4)=1
     IVA=ABS(IV(J,2))
     IF(IVA.EQ.5) THEN
       IV(J,2)=-JY
     ENDIF
     GOTO 16
C MOVE IN THE - Z DIRECTION
  5  IV(J,3)=IV(J,3)-1
     NTRY(5)=1
     IVA=ABS(IV(J,3))
     IF(IVA.EQ.5) THEN
       IV(J,3)=-JZ
     ENDIF
     GOTO 16
C MOVE IN THE + Z DIRECTION
  6  IV(J,3)=IV(J,3)+1
     NTRY(6)=1
     IVA=ABS(IV(J,3))
     IF(IVA.EQ.5) THEN

```

```

      IV(J,3)=-JZ
    ENDIF
C IF THE SPOT WHICH THE VACANCY IS TRYING TO MOVE TO
C HAS ALREADY BEEN THE SITE WHICH A PROTON HAS
C MOVED INTO DURING THIS TIME INTERVAL,
C OR IS THE SITE OF ANOTHER VACANCY, THEN GO BACK
C AND PICK ANOTHER DIRECTION TO MOVE.
16   IF(MARK(IV(J,1),IV(J,2),IV(J,3)).EQ.1) THEN
      IV(J,1)=JX
      IV(J,2)=JY
      IV(J,3)=JZ
      MTRY=NTRY(1)+NTRY(2)+NTRY(3)+NTRY(4)+
1     NTRY(5)+NTRY(6)
C IF THE VACANCY HAS NOT BEEN ALLOWED TO MOVE TO ANY
C OF THE NN SIX SITES DURING THIS TIME INTERVAL,
C I.E. MTRY=6, THEN GO ON TO THE NEXT VACANCY
      IF(MTRY.EQ.6) GOTO 109
      GOTO 12
    ENDIF
C CHECK TO SEE WHETHER THE VACANCY MOVED INTO THE
C MUON'S POSITION; IF SO THEN,MOVE THE POSITION
C MARKER FOR THE MUON
      IF(IV(J,1).EQ.MPOS(1).AND.IV(J,2)
1     .EQ.MPOS(2).AND.IV(J,3).EQ.MPOS(3)) THEN
      MPOS(1)=JX
      MPOS(2)=JY
      MPOS(3)=JZ
      MMPOS=MMPOS+1
      MNPOSJ=1
      MNN=MNN+1
      WRITE(6,1007) MPOS,I,J
1007  FORMAT(1X,'THE MUON HAS MOVED TO ('
1     2(I3,' '),I3,') DURING LOOP',I5,' AND',
2     'HAS SWAPPED POSITION WITH VACANCY',
3     I3)
      DO 113 M1=1,6
      DO 114 M2=1,3
C MOVE THE MARKERS FOR THE NN
      IF(((M1+1)/M2).EQ.2) THEN
      NN(M1,M2)=MPOS(M2)-(-1)**M1
      ELSE IF(M1.EQ.2.AND.M2.EQ.1) THEN
      NN(M1,M2)=MPOS(M2)-(-1)**M1
      ELSE
      NN(M1,M2)=MPOS(M2)
      ENDIF
114   CONTINUE
113   CONTINUE
    ENDIF
C EXCHANGE THE SPINS BETWEEN THE OLD AND NEW PROTON
C SITES.
      DO 110 JS=1,3
      SPIN(JX,JY,JZ,JS)=
1     SPIN(IV(J,1),IV(J,2),IV(J,3),JS)

```

```

        SPIN(IV(J,1),IV(J,2),IV(J,3),JS)=0.0
110  CONTINUE
C MARK=1 MEANS THAT THE PARTICLE IN THAT SITE HAS
C MOVED TO THAT SITE DURING THIS TIME INTERVAL
      MARK(IV(J,1),IV(J,2),IV(J,3))=1
      MARK(JX,JY,JZ)=1
C GO ON TO THE NEXT VACANCY
109  CONTINUE
      DO 116 L2=1,7
      DO 111 L1=1,6
      IF(NN(L1,1).EQ.IV(L2,1).AND.NN(L1,2).
1 EQ.IV(L2,2).AND.NN(L1,3).EQ.IV(L2,3)) THEN
          NCHECK(I,L2)=1
      ENDIF
111  CONTINUE
      IF((NCHECK(I,L2)-NCHECK(I-1,L2)).EQ.1) THEN
          MNPOS1=1
          MNN=MNN+1
      ELSE IF((NCHECK(I,L2)-NCHECK(I-1,L2)).EQ.-1)
1 THEN
          MNPOS2=1
          MNN=MNN+1
      ENDIF
116  CONTINUE
      CALL BCAL(BN)
      BNB=BN(1)*BX(1)+BN(2)*BX(2)+BN(3)*BX(3)
C DOT PRODUCT OF THE MAGNETIC FIELD WITH THE UNIT
C VECTOR OF THE EXTERNAL APPLIED MAGNETIC FIELD
C FC IS THE MUON FIELD CORRELATION
      IF(BOB.NE.0.0) THEN
          FC=BNB/BOB
      ELSE
          FC=BNB
      ENDIF
      IF(MNPOS1.EQ.1.AND.MNPOS2.EQ.1.AND.
1 MNPOS3.EQ.1) THEN
          WRITE(2,1009) BNB,FC,I,MNN
1009  FORMAT(2(1X,1PE13.6),2(1X,I5),' NN MOVES ',
1 'AND VACANCY I/O AND MUON')
      ELSE IF(MNPOS1.EQ.1.AND.MNPOS2.EQ.1.AND.
1 MNPOS3.EQ.0) THEN
          WRITE(2,1010) BNB,FC,I,MNN
1010  FORMAT(2(1X,1PE13.6),2(1X,I5),' NN MOVES ',
1 'AND VACANCY I/O')
      ELSE IF(MNPOS1.EQ.1.AND.MNPOS2.EQ.0.AND.
1 MNPOS3.EQ.1) THEN
          WRITE(2,1011) BNB,FC,I,MNN
1011  FORMAT(2(1X,1PE13.6),2(1X,I5),' NN MOVES ',
1 'AND VACANCY IN AND MUON')
      ELSEIF(MNPOS1.EQ.0.AND.MNPOS2.EQ.1.AND.
1 MNPOS3.EQ.1) THEN
          WRITE(2,1012) BNB,FC,I,MNN
1012  FORMAT(2(1X,1PE13.6),2(1X,I5),' NN MOVES ',

```

```

1 'AND VACANCY OUT AND MUON')
  ELSE IF(MNPOS1.EQ.1.AND.MNPOS2.EQ.0.AND.
1 MNPOS3.EQ.0) THEN
  WRITE(2,1013) BNB,FC,I,MNN
1013 FORMAT(2(1X,1PE13.6),2(1X,I5),' NN MOVES ',
1 'AND VACANCY IN')
  ELSE IF(MNPOS1.EQ.0.AND.MNPOS2.EQ.1.AND.
1 MNPOS3.EQ.0) THEN
  WRITE(2,1014) BNB,FC,I,MNN
1014 FORMAT(2(1X,1PE13.6),2(1X,I5),' NN MOVES ',
1 'AND VACANCY OUT')
  ELSE IF(MNPOS1.EQ.0.AND.MNPOS2.EQ.0.AND.
1 MNPOS3.EQ.1) THEN
  WRITE(2,1015) BNB,FC,I,MNN
1015 FORMAT(2(1X,1PE13.6),2(1X,I5),' NN MOVES ',
1 'AND MUON MOVE')
  ELSE
  WRITE(2,1016) BNB,FC,I,MNN
1016 FORMAT(2(1X,1PE13.6),2(1X,I5),' NN MOVES')
  ENDIF
  MNPOS1=0
  MNPOS2=0
  MNPOS3=0
108 CONTINUE
  WRITE(6,1008) MMPOS,MNN
1008 FORMAT(1X,'OVER 3000 TIME INTERVALS, THE ',
1 'MUON MOVED',I4,' TIMES AND HAD',I5,
2 ' NN VACANCIES.')
  STOP
  END
CCCCCCCCCCCCCCCCCCCCCCCCCCCCCCCCCCCCCCCCCCCCCCCCCCCCCCCC
C                                                                 C
C SUBROUTINE TO CALCULATE THE MAGNETIC FIELD                     C
C FELT BY THE MUON FROM PROTONS WITH A                          C
C DISTANCE EQUAL TO SQRT(20.).                                    C
C                                                                 C
CCCCCCCCCCCCCCCCCCCCCCCCCCCCCCCCCCCCCCCCCCCCCCCCCCCCCCCC
  SUBROUTINE BCAL(B)
  COMMON /S/SPIN(-4:4,-4:4,-4:4,3)
  COMMON /MUON/MPOS(3)
  REAL B(3)
  INTEGER LOC(3)
C SET THE MAGNETIC FIELD IN THE THREE DIRECTIONS
C EQUAL TO ZERO
  B(1)=0.
  B(2)=0.
  B(3)=0.
  DO 100 IX=-4+MPOS(1),4+MPOS(1)
  LOC(1)=IX-MPOS(1)
  I=IX
C IF MOD(I) OR (J) OR (K) IS GREATER THAN 4, THEN
C WRAP AROUND AND LOOK AT THE SPIN ON THE OTHER
C SIDE OF THE LATTICE.

```

```

IF(I.LT.-4) I=I+9
IF(I.GT.4) I=I-9
DO 101 JY=-4+MPOS(2),4+MPOS(2)
LOC(2)=JY-MPOS(2)
J=JY
IF(J.LT.-4) J=J+9
IF(J.GT.4) J=J-9
DO 102 KZ=-4+MPOS(3),4+MPOS(3)
LOC(3)=KZ-MPOS(3)
K=KZ
IF(K.LT.-4) K=K+9
IF(K.GT.4) K=K-9
C IF THE LATTICE SITE IS THE MUON SITE THEN GO ON TO
C THE NEXT SITE
      IF(LOC(1).EQ.0.AND.LOC(2).EQ.0.AND.
      1 LOC(3).EQ.0) GOTO 102
C R2 IS THE SQUARE OF THE DISTANCE BETWEEN THE
C PROTON AND MUON LATTICE SITES
      R2=LOC(1)**2+LOC(2)**2+LOC(3)**2
      IF(R2.GT.20.) GOTO 102
      R3=R2**1.5
C DPIR IS THE DOT PRODUCT BETWEEN THE SPIN AND
C DIRECTIONAL VECTOR
      DPIR=(LOC(1)*SPIN(I,J,K,1)+LOC(2)*
      1 SPIN(I,J,K,2)+LOC(3)*SPIN(I,J,K,3))/R2
      DO 103 L=1,3
C B(L) IS THE MAGNETIC FIELD IN THE LTH DIRECTION
      B(L)=B(L)+(3.0*DPIR*LOC(L)-SPIN(I,J,K,L))/R3
103  CONTINUE
102  CONTINUE
101  CONTINUE
100  CONTINUE
      RETURN
      END

```



APPENDIX B  
DIPOLAR BROADENING BY UNLIKE SPINS<sup>62</sup>

For a system of two spins (I and S), the total Hamiltonian is

$$H = H_0^I + H_0^S + H_1^{II} + H_1^{SS} + H_1^{IS}. \quad (\text{B.1})$$

The terms  $H_0^I$  and  $H_0^S$  are the Zeeman Hamiltonians for spin I and S, respectively. The terms  $H_1^{II}$ ,  $H_1^{SS}$  and  $H_1^{IS}$  are the dipolar Hamiltonians which describe the interaction of the spins among themselves and with each other. The second moment for spin I is represented by the contributions due to interactions among itself and also with spin S.

$$M_2^I = (M_2^I)_{II} + (M_2^I)_{IS} \quad (\text{B.2})$$

Each term can be calculated separately using a Van Vleck formula for unlike and like spins.

$$(M_2^I)_{IS} = 1/3 \gamma_I^2 \gamma_S^2 I(I+1) \hbar^2 \{ \sum_j (1-3\cos^2\theta_j)^2 / r_j^6 \} \quad (\text{B.3})$$

$$(M_2^I)_{II} = 3/4 \gamma_I^4 I(I+1) \hbar^2 \{ \sum_j (1-3\cos^2\theta_j)^2 / r_j^6 \} \quad (\text{B.4})$$

Use of the time-differential technique prohibits interactions between two muons, since only events resulting from one muon being in the sample at a time are kept. Therefore if spin  $S$  is associated with the proton and spin  $I$  with the muon, the only term left in Eqn. B.2 is  $(M_2^I)_{IS}$ .

In NMR, the broadening due to like spins has been found to lead to a difference between the r.m.s width, given by the second moment, and the full-width half-maximum of the line. This difference may be observed by calculating the fourth moment of the line. The fourth moment is symbolically written as

$$M_4 \propto (H_1^{II})^4 + (H_1^{IS})^4 + (H_1^{II})^2 (H_1^{IS})^2 + (H_1^{SS})^2 (H_1^{IS})^2 \quad (\text{B.5})$$

Each of these terms is proportional to a gyromagnetic ratio.

$$H_1^{XY} \propto \gamma_X \gamma_Y \quad (\text{B.6})$$

Since there is only one muon in the sample at a time, the  $H_1^{II}$  terms in Eqn. B.5 may be dropped. If Eqn. B.5 is written in terms of  $H_1^{IS}$ , then

$$M_4 \propto (H_1^{IS})^4 + (3/2(\gamma_S/\gamma_I))^2 (H_1^{IS})^2 (H_1^{IS})^2. \quad (\text{B.7})$$

The factor of 3/2 is the multiplicative constant between calculations of the second moment for like and unlike

spins assuming only dipolar interactions. Substituting in the gyromagnetic ratio for the proton (spin S) and the muon (spin I), one finds that

$$\gamma_S/\gamma_I = 1/3.18. \quad (\text{B.8})$$

$$M_4 \propto 1.22(H_1^{IS})^4 \quad (\text{B.9})$$

If the hydrogen-hydrogen interactions would have been ignored, then

$$M_4 \propto 1.00(H_1^{IS})^4. \quad (\text{B.10})$$

The addition to  $M_4$  is, therefore, due to spin flip-flops of the protons. This has the effect of reducing the r.m.s value of the line width by  $(1.22)^{1/4}$  or 1.05. This is a very small effect and does not change the line noticeably from a Gaussian shape, but is enough to reduce the effective line width from the r.m.s. value.

## APPENDIX C

### DERIVATION OF THE PARAMETERS $\alpha$ AND $\tau_B$ <sup>50,63,64</sup>

The parameter,  $\alpha$ , is defined as<sup>64</sup>

$$\alpha = \int_0^{\infty} dt \exp(-t/\tau_{\mu}) d\Gamma(t)/dt \quad (C.1)$$

where  $\Gamma(t)$  is the argument of the muon spin relaxation function,  $P(t)$ , and  $\tau_{\mu}$ , the mean lifetime of a muon.

$$P(t) = \exp[-\Gamma(t)] \quad (C.2)$$

If  $P(t)$  is of the Abragamian form (Eqn. 5.25), then

$$\Gamma(t) = \Delta^2 \tau^2 (\exp(-t/\tau) - 1 + t/\tau). \quad (C.3)$$

If this is substituted into Eqn. C.1, then

$$\alpha = \Delta^2 \tau_{\mu}^2 / (\tau + \tau_{\mu}) \quad (C.4)$$

Another form for  $\Gamma(t)$  is that for the two-trap model:

$$\Gamma(t) = \sum_{i=1,2} \Delta_i^2 \int_0^t dt' \int_0^{t'} N_i(t_2) G_{ii}(t'-t_2) \quad (C.5)$$

where  $\Delta_1^2$ ,  $N_1(t)$ , and  $G_{11}(t)$  are the second moment, probability for occupation, and the autocorrelation function for the muon at site 1. Let us make the following assumptions which are pertinent to the model in Section 7.1A.1:

- i) Site 1 and 2 are defined to be sites of octahedral and tetrahedral symmetry, respectively.
- ii) The probability for occupying an octahedral (tetrahedral) site initially equals  $1-c'$  ( $c'$ ) where  $c'$  is the effective vacancy concentration.
- iii) The rate,  $r$ , is the transition rate from an O to a T site.
- iv) The autocorrelation function for an O site is

$$G_{11}(t) = \exp(-t/r_s) \quad (C.6)$$

where  $r_s$  is a mean time of stay at an O site. Since the muon does not activate out of a T site at room temperature, the autocorrelation function for this site is

$$G_{22}(t) = 1. \quad (C.7)$$

This allows the T site to be considered as a deeper trap than the O site.

These assumptions yield:

$$\Gamma(t) = \Delta_{TET}^2 \int_0^t dt_1 [1 - (1-c') \exp(-rt_2)] dt_2 + \quad (C.8)$$

$$\Delta_{OCT}^2 \int_0^t dt_1 (1-c') \exp(-rt_2) \text{EXP}[-(t_1-t_2)/r_s] dt_2.$$

If this is substituted into Eqn. C.1 with the additional assumption that

$$r = c'/r_s, \quad (C.9)$$

then after some manipulation one finds that

$$r_s = c' r_\mu [-0.5(1+c' + (1-c') \Delta_{TET}^2 r_\mu^2 / (\alpha - \Delta_{TET}^2 r_\mu^2)) + \quad (C.10)$$

$$\pm [0.25 \times \{ (1-c') \alpha / (\alpha - \Delta_{TET}^2 r_\mu^2) \}^2 +$$

$$(1-c') c' \Delta_{OCT}^2 r_\mu^2 / (\alpha - \Delta_{TET}^2 r_\mu^2) ]^{1/2}]^{-1} .$$

## APPENDIX D

### CALCULATION OF A ZERO-FIELD RELAXATION FUNCTION<sup>61</sup>

The calculation of the zero-field muon spin relaxation function requires the Hamiltonian contain terms which describe the dipolar interaction between the muon and the nearest-neighbor protons. The first-order effects of hydrogen-hydrogen dipolar interactions can also be included in the Hamiltonian. However, care must be taken to balance the need for precision by the inclusion of more protons and the amount of space and time available on a computer.

$$H = \sum_{ij} [\vec{\mu}_i \cdot \vec{\mu}_j - 3(\vec{\mu}_i \cdot \hat{r}_{ij})(\vec{\mu}_j \cdot \hat{r}_{ij})] / r_{ij}^3 \quad (D.1)$$

The  $i$  and  $j$  in the dipolar Hamiltonian (Eqn. D.1) indices correspond to the muon and the nearest-neighbor protons, respectively. To calculate the relaxation function,  $G_2(t)$ , one must solve for the eigenstates and calculate the relative energies of the states. This entails diagonalizing the Hamiltonian matrix. Having done this,  $G_2(t)$  can be calculated.

$$G_2(t) = 1/3 \langle \exp(iHt/\hbar) \vec{\sigma}(0) \exp(-iHt/\hbar) \cdot \vec{\sigma}(0) \rangle \quad (D.2)$$

For a muon in an octahedral site, there are eight nearest-neighbor protons which must be included. In the calculation of the polarization for a muon in an octahedral site, the proton-proton dipolar coupling between nearest-neighbor hydrogen nuclei was included as a perturbation. This had the effect of lowering the muon polarization at long times. However, since only half the number of protons which interact with a nearest-neighbor proton were included, the proton-proton coupling was increased by a factor of  $\sqrt{2}$  to attempt to compensate for this.

$$H_1 = \sqrt{2} \sum_{ij} [\vec{\mu}_i \cdot \vec{\mu}_j - 3(\vec{\mu}_i \cdot \hat{r}_{ij})(\vec{\mu}_j \cdot \hat{r}_{ij})] / r_{ij}^3 \quad (D.3)$$

The summation is over nearest-neighbor protons. The calculation of  $G_z(t)$  entailed diagonalizing a  $512 \times 512$  matrix.

For a muon in a tetrahedral site, the calculation with six nearest-neighbor protons entailed diagonalizing a  $128 \times 128$  matrix. Since none of the nearest-neighbor hydrogen atoms for the nearest-neighbor protons (to the muon) are included in the eigenstates of this calculation, no dipolar coupling for the proton-proton interaction could be included. If this had been done, then the size of the matrix would have increased from  $128 \times 128$  to at least  $524,288 \times 524,288$  assuming that only second-nearest-neighbor protons are included.



APPENDIX E

ZERO-FIELD SPIN-SPIN RELAXATION TIME<sup>50</sup>

Initially, one starts with the relaxation function  $G(t)$ .

$$G(t) = \frac{\langle \vec{\sigma}(t) \cdot \vec{\sigma}(0) \rangle}{\langle \vec{\sigma}(0) \cdot \vec{\sigma}(0) \rangle} \quad (E.1)$$

$$= 1/3 \langle \exp(iHt/\hbar) \vec{\sigma}(0) \exp(-iHt/\hbar) \cdot \vec{\sigma}(0) \rangle \quad (E.2)$$

where  $H$  is the dipolar Hamiltonian and  $\vec{\sigma}$  is the Pauli spin matrix for the proton. The brackets denote an average over the muon and proton lattice states.

$$H = \sum_{ij} [\vec{\mu}_i \cdot \vec{\mu}_j - 3(\vec{\mu}_i \cdot \hat{r}_{ij})(\vec{\mu}_j \cdot \hat{r}_{ij})] / r_{ij}^3 \quad (E.3)$$

$$= -\sum_{ij} \vec{\mu}_i \cdot \vec{B}_{ij} \quad (E.4)$$

where  $\vec{B}_{ij} = \{\vec{\mu}_j - 3(\vec{\mu}_j \cdot \hat{r}_{ij})\hat{r}_{ij}\} / r_{ij}^3 \quad (E.5)$

To calculate  $T_2$  from the relaxation function, one must find the second moment.

$$M_2 = - \left. \frac{d^2 G}{dt^2} \right|_{t=0} \quad (E.6)$$

Taking the second derivative of  $G(t)$  and invoking cyclical invariance of the trace, one arrives at the following.

$$M_2 = -\langle [H, \bar{\sigma}] \cdot [H, \bar{\sigma}] \rangle / (3\hbar^2) \quad (\text{E.7})$$

The commutator of the dipolar Hamiltonian and the Pauli spin matrix for the proton was found to be

$$[H, \bar{\sigma}] = -2\gamma_i \hbar [ \hat{i}(\mu_Y B_Z - \mu_Z B_Y) + \hat{j}(\mu_Z B_X - \mu_X B_Z) + \hat{k}(\mu_X B_Y - \mu_Y B_X) ] \quad (\text{E.8})$$

Upon performing the dot product and taking the trace over the states, one finds the formula for the second moment of the  $j$ th proton.

$$M_2 = \gamma_i^2 \gamma_j^2 \hbar^2 \sum_l (1/r_{lj}^6) \quad (\text{E.9})$$

If one is attempting to calculate the second moment of a proton due to a lattice of protons, then  $\gamma_i^2$  is equal to  $\gamma_j^2$ . To calculate the contribution by the muon to the second moment,  $\gamma_i^2$  equals  $\gamma_\mu^2$  and the summation is no longer needed since there is only one muon. The zero-field second moment of a proton nearest neighbor to the muon is the sum of contributions from the lattice of protons and from the muon.

$$M_2 = M_{2p-p} + M_{2p-\mu} \quad (\text{E.10})$$

## REFERENCES

1. R. L. Garwin, L. M. Ledermann, and M. Weinrich, *Phys. Rev.* 105, 1415 (1957).
2. R. H. Heffner and D. G. Flemming, *Phys. Today* 37(12), 38 (1984).
3. E. Karlsson, *Phys. Rep.* 82, 271 (1982).
4. A. Schenck, *Muon Spin Rotation Spectroscopy* (Adam Hilger Ltd, Bristol, 1985).
5. M. Aguilar-Benitez et al., *Phys. Lett.* 170B, 1 (1986).
6. A. C. Melissinos, *Experiments in Modern Physics* (Academic Press, New York, 1966).
7. J. Chappert, in *Muons and Pions in Materials Research*, edited by J. Chappert and R. I. Grynspan (North-Holland, Amsterdam, 1984).
8. G. W. Ford and C. J. Mullin, *Phys. Rev.* 108, 477 (1957).
9. D. K. Brice, *Phys. Lett.* 66A, 53 (1978).
10. F. Volino, in *Muons and Pions in Materials Research*, edited by J. Chappert and R. I. Grynspan (North-Holland, Amsterdam, 1984).
11. D. E. Gray (ed.), *American Institute of Physics Handbook* (McGraw-Hill, New York, 1972).
12. C. Kittel, *Introduction to Solid State Physics* (John Wiley & Sons, New York, 1976).
13. K. Schroeder, in *Point Defects in Metals II*, edited by G. Hohler (Springer-Verlag, Berlin, 1980).
14. Z. W. Lu (private communication).
15. P. Jena, K. S. Singwi, and R. M. Nieminen, *Phys. Rev. B* 17, 301 (1978).
16. H. Teichler, *Phys. Lett.* 67A, 313 (1978).

17. M. Camani et al., Phys. Rev. Lett. 29, 836 (1977).
18. M. A. Preston and R. K. Bhaduri, Structure of the Nucleus (Addison-Wesley, Reading, Massachusetts, 1975).
19. K. W. Kehr, in Hydrogen in Metals I, edited by G. Alefeld and J. Volkl (Springer-Verlag, Berlin, 1978).
20. D. Richter, in Neutron Scattering and Muon Spin Rotation, edited by G. Hohler (Springer-Verlag, Berlin, 1983).
21. C. Korn and D. Zamir, J. Phys. Chem. Solids 31, 489 (1970).
22. R. S. Hayano et al., Phys. Rev. Lett. 41, 421 (1978).
23. Y. Kitaoka et al, Hyp. Int. 12, 51 (1982).
24. R. F. Kiefl, Hyp. Int. 32, 707 (1986).
25. V. G. Grebinnik et al., Sov. Phys. JETP 48, 1002 (1978).
26. O. Hartmann, Phys. Rev. Lett. 39, 832 (1977).
27. D. Richter et al., J. Chem. Phys. 79, 4564 (1983).
28. R. S. Hayano et al., Phys. Rev. B 20, 850 (1979).
29. R. Kubo and T. Toyabe, in Magnetic Resonance and Relaxation, edited by R. Blinc (North-Holland, Amsterdam, 1967).
30. M. Celio and P. F. Meier, Hyp. Int. 17-19, 435 (1984).
31. K. G. Petzinger and S. H. Wei, Hyp. Int. 17-19, 441 (1984).
32. K. Binder, in Monte Carlo Methods in Statistical Physics, edited by K. Binder (Springer-Verlag, Berlin, 1979).
33. M. Doyama et al., Hyp. Int. 9, 711 (1981).
34. W. J. Kossler et al., Hyp. Int. 31, 235 (1986).
35. C. Korn and D. Zamir, J. Phys. Chem. Solids 34, 725 (1973).

36. L. D. Bustard, R. M. Cotts, and E. F. W. Seymour, *Phys. Rev. B* 22, 12 (1980).
37. C. L. Bisson and W. D. Wilson, in *Effects of Hydrogen on Behavior of Materials*, Proceedings of an International conference, Moran, Wyoming, 1975, edited by A. W. Thompson and I. M. Bernstein (Metallurgical Society of AIME, New York, 1976).
38. K. G. Petzinger, *Phys. Rev. B* 26, 6530 (1982).
39. W. J. Kossler et al., *J. Less-Common Met.* 129, 327 (1987).
40. H. L. Yakel, Jr., *Acta Cryst.* 11, 46 (1958)
41. C. Korn, *Phys. Rev. B* 28, 95 (1983).
42. A. San-Martin and F. D. Manchester (unpublished) and references therein.
43. J. P. Blackledge, in *Metal Hydrides*, edited by W. M. Mueller, J. P. Blackledge, and G. G. Libowitz (Academic, New York, 1968).
44. R. L. Beck and W. M. Mueller, in *Metal Hydrides*, edited by W. M. Mueller, J. P. Blackledge, and G. G. Libowitz (Academic, New York, 1968).
45. R. Bischof, M. Tellefsen, and E. Kaldis, *J. Less-Common Met.* 110, 99 (1985).
46. W. M. Mueller, in *Metal Hydrides*, edited by W. M. Mueller, J. P. Blackledge, and G. G. Libowitz (Academic, New York, 1968).
47. P. Klavins, R. N. Shelton, R. G. Barnes, and B. J. Beaudry, *Phys. Rev. B* 29, 5349 (1984).
48. J. E. Bonnet and J. N. Daou, *J. Appl. Phys.* 48, 964 (1977).
49. P. R. Bevington, *Data Reduction and Error Analysis for the Physical Sciences* (McGraw-Hill, New York, 1969).
50. K. G. Petzinger (private communication).
51. F. N. Gygax et al., *Hyp. Int.* 17-19, 267 (1984).
52. O. Hartmann et al., *Hyp. Int.* 31, 241 (1986).
53. F. N. Gygax et al., *Hyp. Int.* 17-19, 377 (1984).

54. S. S. Pan, M. L. Yeager, and W. E. Moore, in *Molecular Dynamics and Structures of Solids*, edited by R. S. Carter and J. J. Rush (U. S. Government Printing Office, Washington, D. C., 1969).
55. H. Teichler, *Phys. Lett.* 64A, 78 (1977).
56. D. Khatamian, W. A. Kamitakahara, R. G. Barnes, and D. T. Peterson, *Phys. Rev. B* 21, 2622 (1980).
57. D. L. Anderson, R. G. Barnes, D. T. Peterson, and D. R. Torgeson, *Phys. Rev. B* 21, 2625 (1980).
58. W. B. Pearson, *A Handbook of Lattice Spacings and Structures of Metals and Alloys* (Pergamon, Oxford, 1958).
59. D. L. Anderson et al., *J. Less-Common Met.* 73, 243 (1980).
60. H. A. Enge, *Introduction to Nuclear Physics* (Addison-Wesley, Reading, Massachusetts, 1966).
61. Y. Li and K. G. Petzinger (private communication).
62. A. Abragam, *Principles of Nuclear Magnetism* (Clarendon, Oxford, 1962).
63. K. G. Petzinger, R. L. Munjal, and E. Zaremba, *Hyp. Int.* 6, 223 (1979).
64. A. T. Flory, *Hyp. Int.* 6, 261 (1979).

## VITA

James Russell Kempton

Born, April 15, 1960, in Richmond, Indiana, he graduated from Centerville Senior High School in May 1978. In June 1982, he received a Bachelor of Arts from Wittenberg University with a concentration in physics. During the summer of 1982, he worked as an intern at Wright-Patterson Air Force Base and did research in the area of GaAs semiconductors. He received a Master of Science with a concentration in physics from The College of William and Mary in May 1984. He will be awarded a Doctor of Philosophy by The College of William and Mary in December 1987. He has accepted a post-doctoral position in gas-phase  $\mu$ SR at TRIUMF and will assume these duties in late 1987.